NOVEL SIGNAL PROCESSING TECHNIQUES FOR REMOTE SENSING APPLICATIONS

A DISSERTATION SUBMITTED TO

THE GRADUATE SCHOOL OF ENGINEERING AND SCIENCE

OF BILKENT UNIVERSITY

IN PARTIAL FULFILLMENT OF THE REQUIREMENTS FOR

THE DEGREE OF

DOCTOR OF PHILOSOPHY

IN

ELECTRICAL AND ELECTRONICS ENGINEERING

By

Gökhan GÖK

June 2021

Novel Signal Processing Techniques for Remote Sensing Applications
By Gökhan GÖK
June 2021

We certify that we have read this dissertation and that in our opinion it is fully adequate, in scope and in quality, as a dissertation for the degree of Doctor of Philosophy.

Orhan Arıkan(Advisor)

Sinan Gezici

Cenk Toker

Lütfiye Durak Ata

Çağatay Candan

Approved for the Graduate School of Engineering and Science:

Ezhan Karaşan
Director of the Graduate School

ABSTRACT

NOVEL SIGNAL PROCESSING TECHNIQUES FOR REMOTE SENSING APPLICATIONS

Gökhan GÖK
Ph.D. in Electrical and Electronics Engineering
Advisor: Orhan Arıkan
June 2021

Remote sensing is the acquisition of information about an object or phenomenon without a direct contact. In this thesis, novel signal processing techniques are proposed for two different remote sensing applications. First, for the reconstruction of electron density profile in the ionosphere using the ionosonde measurements, a new technique, ISED, is proposed. By using a hidden Markov model, ISED technique first identifies actual ionosonde echoes reflected from the ionosphere. Then, vertical electron density profile is estimated as the solution to a model based convex optimization problem. Conducted experiments on real ionosonde data show that ISED overperforms the state of the art ionogram inversion tools. Second part, for Specific Emitter Identification (SEI) of radar transmitters, a new SEI technique is proposed. SEI is an important Electronic Warfare (EW) activity that aims to identify unique transmitters, even the emitters of same kind, by using the subtle differences on the transmitted signals. Proposed SEI consist of two main stages. In the first stage, received radar pulses are time aligned and coherently integrated to reveal subtle differences which could be used to distinguish different radar transmitters. In the second step, Variational Mode Decomposition (VMD) is used to decompose both the envelope and the instantaneous frequency of the received radar signal into a set of modes. Then, these mod signals are characterized by using a group of features for identification. Highly successful identification performance with the proposed method on real radar datasets is demonstrated.

Keywords: Remote sensing, ionogram scaling, true height analysis, ARTIST, NhPC, hidden markov models, ionosonde, ISED, optimization, model based electron density reconstruction, ionosphere, specific emitter identification, unintentional modulation on pulse, variational mode decomposition, radar pulse time aligment, radar emitter classification, time-frequency domain features.

ÖZET

UZAKTAN ALGILAMA UYGULAMALARI İÇİN YENİLİKÇİ TEKNİKLER

Gökhan GÖK
Elektrik ve Elektronik Mühendisliği, Doktora
Tez Danışmanı: Orhan Arıkan
Haziran 2021

Uzaktan algılama, ilgilenilen bir obje veya olgu ile ilgili belirli bilgilerin uzaktan sezilmesini ifade etmektedir. Bu tez kapsaminda, bilinen iki ayrı uzaktan algılama problemine yenilikçi çözümler önerilmiştir. Birince kısımda, ISED ismini verdiğimiz, ionosonda ölçümlerinden otomatik olarak iyonosferindeki elektron yoğunluk dağılımını elde eden bir yöntem önerilmiştir. ISED yöntemi, ionosonda ölçümleri içerisinde, iyonosfer katmanlarından yansıyan işaretleri Saklı Markov Modelleri (SMM) kullanarak bulmaktadır. Ardından, elektron yoğunluk dağılımı hesaplaması için model tabanlı iç bükey maliyet yüzeyine sahip bir eniyileme problemi çatılarak elektron yoğunluk dağılımı hesaplanmaktadır. Yapılan benzetimlerde, ISED yönteminin halihazırda kullanılan yöntemlere göre daha iyi performans gösterdiği gözlenmiştir. İkinci kısımda, literatürde 'Specific Emitter Identification' (SEI) olarak bilinen bir radar elektronik harp problemi için yeni bir yöntem önerilmiştir. SEI sistemleri, farklı göndermeç sistemlerini, bunlar aynı tip gönderme sistemleri olsa bile, işaretlerin üzerindeki küçük farkları kullanarak kimliklendirmeyi amaçlamaktadır. Önerilen yöntem, iki aşamadan oluşmaktadır. İlk adımda, ölçülen radar darbeleri zamanda hizalanmakta ve evre uyumlu bir şekilde entegre edilemektedir. Böylece, işaretlerin üzerindeki küçük farklılıklar ortaya çıkarılmaktadır. Ardından Varyasyonel Kip Ayrıştırıcı (VKA) kullanılarak entegre edilen radar darbelerinin anlık faz ve frekansları kiplere ayrıştırılmaktadır. Elde edilen kip işaretleri kullanılarak, ilgili işaretleri tanımlayan öznitelikler hesaplanmaktadır. Radar veri setleri ile yapılan benzetimlerde, önerilen yöntemin yüksek bir başarıma sahip olduğu gözlenmiştir.

Anahtar sözcükler: Uzaktan algılma, iyonogram ölçeklendirme, gerçek yükseklik analizi, ARTIST, NhPC, saklı markov modelleri, iyonosonda, ISED, en iyileme, model tabanlı elektron yoğunluk dağılımı oluşturma, iyonosfer, özel yayın tanıma, işaret üzerindeki istemsiz kipleme, varyasyonel kip ayrıştırıcı, radar

işaretlerinin zamanda hizalanması, radar yayın kimliklendirme, zaman-frekans alanında öznitelikler.

Acknowledgement

First and foremost, I am grateful to my advisor Prof. Orhan Arikan for his exhaustless support and guidance during my Ph.D. studies. While his immense knowledge helped me during this research, his wisdom will guide me rest of my life. Thank you for being a great teacher, a mentor and a father.

I would like to thank my thesis monitoring committee members Prof. Sinan Gezici and Prof. Cenk Toker for numerous technical discussions and helpful suggestions. Also, I would like to thank Prof. Feza Arikan for both technical and non-technical discussions.

I thank my fellow friends Sukru Firat Ada, Mehmet Atak and Dr. Yasar Kemal Alp for their continuous support, valuable advises, and encouragement during my research.

I am very grateful to Aselsan Inc. for providing me the opportunity and motivation to pursue my research. Also, I would like to thank all my colleagues for their contributions to this dissertation.

I also would like to express my gratitude to my parents for their endless encouragement and support through my whole life. Finally, I would like thank to my wife, Rennan, for her support, patience and sincere love which motivated me during the preparation of this dissertation.

Contents

List of Figures

List of Tables

Chapter 1

Introduction

Remote sensing is the acquisition of information about an object or phenomenon without a direct contact. The remote sensing discipline started with the development of flight. In 1858, photographs of Paris are taken using air balloons. With the development of technology, remote sensing clinched to find new areas. Starting from 1900s, the focus of remote sensing shifted to military applications. Beginning with World War I, systematic aerial photography started to be used for military surveillance and reconnaissance purposes. Between World War I and World War II different countries independently developed technologies which led to the modern radar systems. The latter half of the 20th century witnessed the golden age of remote sensing. During the Cold War era, interest in remote sensing increased significantly and countries started developing specialized mission aircrafts for reconnaissance operations. The space race between the two Cold War adversaries, the United States and the former Soviet Union, brought pioneering launches of space probes to explore the outer space and gather information. Today, with the catalyzing effect of military applications, interest in remote sensing progressed to the global scale for wide variety of applications. Remote sensing sensors become important part of daily life and researchers all over the world actively working on the topic.

In a broad sense, remote sensing can be considered in two categories as shown

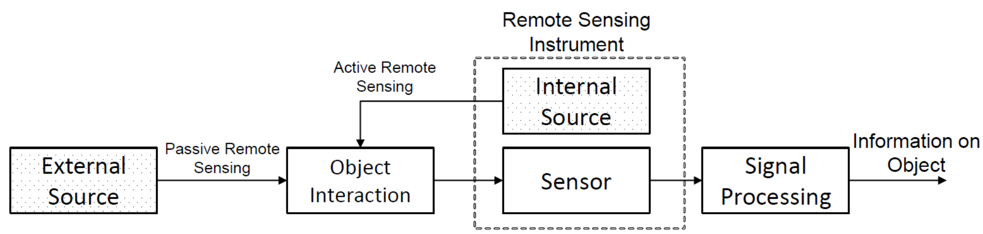

Figure 1.1: Conceptual representation of active and passive remote sensing.

in Fig.1.1. Active remote sensing refers to applications where instruments directs their signals toward the region of interest and acquire data. Majority of instruments employ radio frequency (RF) transmissions since their robust performance in all weather conditions. Radar is probably the best example for active remote sensing where the desired sensing information is extracted by acquiring the reflections of the emitted radio frequency signals. Light detection and ranging (LIDAR) and ultrasound are also important applications of active remote sensing.

The second category is the passive remote sensing. Unlike the active sensors, passive remote sensing depends on the stimuli of external sources which can be either the natural energy such as sun rays reflected by the object or the energy directly emitted by the object. For example, passive radars detect and track objects by capturing reflected signals of non-cooperative sources illuminating the environment. Electronic intelligence systems (ELINT) and electronic support systems (ESM) intercepts signals of radars and identify them which are crucial for Electronic Warfare (EW). Another example is the infrared (IR) remote sensing where the sensors detect the radiations of warm objects. An important civilian application of IR remote sensing is the detection of forest fires on Earth using the IR sensors on the satellites. In military applications, passive IR remote sensing is used by heat seeking missiles and missile approach warning (MAW) systems that are designed to protect different platforms from IR threads.

1.1 Scope of the Thesis

In the scope of this thesis, novel signal processing techniques for two different remote sensing problems are introduced. In the first part of the thesis, a method is proposed for reconstruction of electron density profile in the ionosphere which is a region of the Earth's atmosphere that consists of electrically charged particles namely, ions and electrons. Monitoring of the ionosphere has attracted great attention as electron density distribution directly affects the performance of different critical instruments such as communication or navigation. As a result, electron density distribution of the ionosphere is closely monitored to mitigate the effects of the ionosphere on different instruments.

Ionosondes are important active remote sensing instruments that provide valuable information about the ionospheric weather [2]. Similar to a radar, ionosondes transmit radio waves to the ionosphere. Due to dispersive nature of the ionosphere, radio waves travel slower within the ionosphere compared to the free space. Moreover, if there is a layer at which the electron density reaches to the critical level corresponding to the frequency of transmission, the radio waves reflects back. By scanning a range of transmission frequencies and recording the time of reflection, ionosonde can provide a vertical electron density profile. The velocity of propagation depends on the electron density profile. Therefore, the apparent height or, virtual height, of a layer that is obtained under the assumption of free space propagation velocity of light do not correspond to the actual heights of the layers. The plot of virtual height with respect to transmitted frequency is called the ionogram. The process of reconstructing the electron density with respect to the actual height and estimating the critical parameters of the ionosphere is known as the *ionogram scaling* or *true height analysis* [3, 4].

In the literature, there are various methods for ionogram scaling. Today, the most widely used automatic tool is the Automatic Real Time Ionogram Scaler with True Height (ARTIST). Different surveys in the literature show that ARTIST occasionally produces unacceptable scalings under certain conditions [5].

Here, we propose a new technique for automatic scaling of ionograms which employs Hidden Markov Models (HMM) and model based optimization. The proposed technique makes use of an HMM to extract the ionogram measurements that are directly reflected back from the ionosphere. Constructed HMM offers improved robustness to different practical problems such as the frequency gaps that are usually seen in the ionosonde measurements and it is one of the main contribution of the proposed technique to the automatic scaling literature [6]. Then, a model based optimization problem is cast to reconstruct the electron density profile with respect to the height. Although there exists different techniques which reconstructs the electron density profile using a model based approach [7], the problem that is proposed here has a convex cost surface and can be solved efficiently. Results of the proposed technique are compared with ARTIST using actual ionosonde measurements obtained in Pruhonice, Czech Republic.

In the second part of the thesis, a method for Specific Emitter Identification (SEI) is proposed for radar transmitters. SEI is an important ELINT activity that aims to recognize individual emitters by using Unintentional Modulations on Pulse (UMOP) that are mainly due to manufacturing differences in the transmitter hardware [8]. In conventional EW, radar signals are classified by using a set of parameters or features such as the Pulse Width (PW), Pulse Repetition Interval (PRI), Radio Frequency (RF), Antenna Scan Type/Period (AST/ASP) and the Intentional Modulation on Pulse (IMOP). However, classification of radars by using the conventional techniques becomes an increasingly more challenging task in modern EW due to increased number of emitters and their level of sophistication in a typical EW scenario. Moreover, advances in digital technology allow designers to implement different countermeasures in order to degrade detection and classification performance of the EW systems. Hence, detailed intra-pulse analysis of the received Intermediate Frequency (IF) signals becomes even more critical. Probably most important advantage of SEI techniques is their ability to distinguish emitters belonging to the same manufacturing line which enables the tracking of specific emitters. This property discriminates the SEI from the rest of the traditional parameter based classification techniques and it is thought to be the holy grail of the ELINT analysis.

Chapter 2

Ionosphere Remote Sensing

With the growing development of the technology, monitoring the state of the ionosphere become more and more important. Today, the state of the ionosphere directly affects the performance of many critical instruments including communication or navigation systems which are indispensable part of the daily life. For example, the signals designed for providing navigation information transmitted by the Global Navigation Satellite Systems (GNSS) or the Galileo system travels through the ionosphere. During this trip, the radio waves are refracted and diffracted by the highly variable ionospheric plasma. Since the performance parameters such as accuracy, availability, continuity and integrity of navigation signals are crucial in safety of life and precise positioning applications, detection, monitoring and prediction of the ionospheric effects are important for mitigating the impact. For example, Ground-Based Augmentation System (GBAS) [9] is a system that provide differential positioning corrections for civilian aviation around an airport for takeoff and landings in all weather operations even at zero visibility conditions. In [10], it is stated that changes in the ionosphere degrades the performance of GBAS and by monitoring the ionosphere, performance degradation could be mitigated. Ionospheric weather monitoring has also high importance for military applications as well. In fact, ionosonde network over the globe has expanded rapidly during the Second World War as a result of the need to make predictions of radio propagation over the Earth [3]. In radio communication, skywave or skip refers to the propagation of radio waves reflected or refracted back toward Earth from the ionosphere. This type of communication is not limited by the curvature of the Earth and can be used to communicate beyond the horizon [11, 12].

Ionosondes are important remote sensing instruments that provide valuable information about the ionospheric weather [2]. They transmit modulated HF pulses and record their returns from the ionosphere. Due to its dispersive nature, the radio waves travel slower than the free space in the ionosphere. Moreover, when the critical level of electron density of the corresponding transmission frequency is reached, the radio waves reflect back. Therefore, the apparent height of a reflection is called as the *virtual height*. The plot of virtual height with respect to sounding frequency is called the ionogram which is shown in Fig.2.1. The importance of ionogram is due to the fact a unique relationship exists between the sounding frequency and the vertical profile of the ionization density. As a result, using the ionograms, the underlying vertical profile of the electron distribution at the time of the transmission can be obtained. The process of reconstructing the electron density with respect to height and estimating critical parameters of the ionosphere is known as the *ionogram scaling* or *true height analysis* [3, 4].

The earliest ionospheric stations were all placed in temperate latitudes for scientific purposes, where the echo traces on the ionograms could be manually scaled by classifying a few patterns which are easily recognized. Ionosonde network has been expanded rapidly during the Second World War as a result of the need to make predictions of radio propagation over the earth [3]. Rapid growth of measured data forced researchers to use the same detailed conventions and methods. Consequently, different handbooks have been prepared to standardize the manual scaling of the ionograms [3, 4]. In the last few decades, due to the growing interest in monitoring of the ionosphere and growing amount of collected data, the need for near-real time and reliable automatic true height analysis become more important. As a result, automatic ionogram scaling tools are implemented as signal processing algorithms to extract important ionospheric parameters such as f_oF2, the critical frequency corresponding the F2 layer, and h_mF2, the maximum

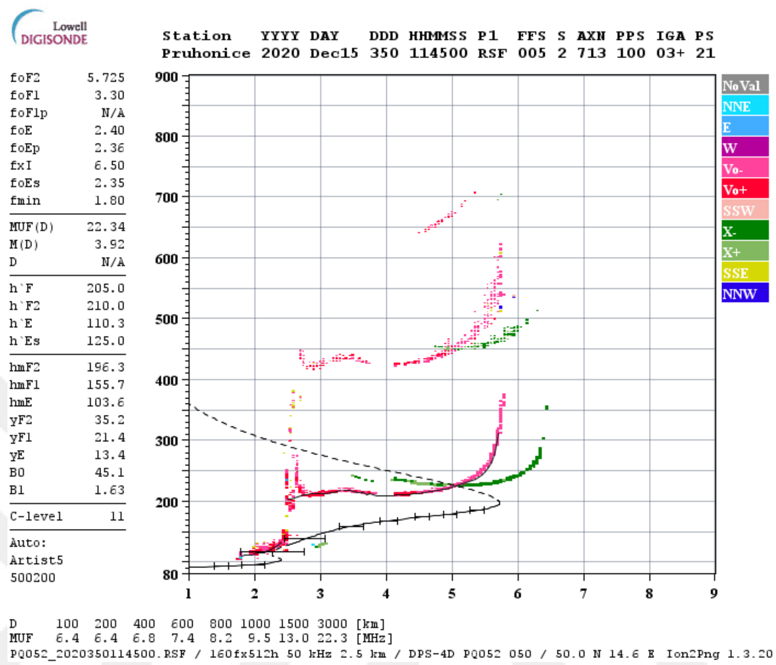

Figure 2.1: A sample ionogram obtained from Pruhonice Station (PQ052), Czech Republic (12 December 2020, 19:15 UTC)

ionization height. More detail of these parameters will be given in Sec.2.1.

Outline of this chapter is as follows. In Sec.2.1, the structure of ionosphere is given. In Sec.2.2, ionosonde, the remote sensing instrument of ionosphere, is introduced. In Sec.2.2.1, relation between the ionosonde measurements and the electron density distribution in the ionosphere is explained. In Sec.2.3, existing literature about the automatic ionogram scaling tools are discussed.

2.1 Structure of the Ionosphere

In this section, structure of the ionosphere and the dynamics affecting the ionospheric weather are briefly discussed. More detailed descriptions are available in [13–19].

Ionosphere is a region of the Earth's atmosphere which consist of high enough

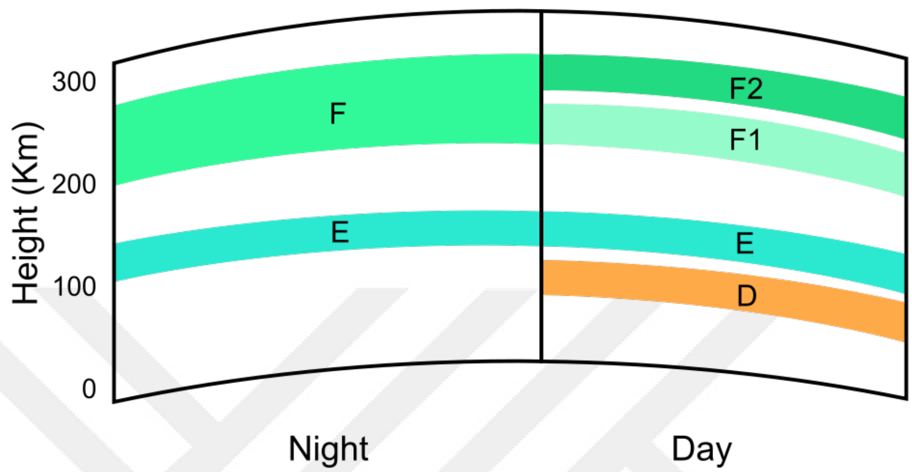

Figure 2.2: Typical layers observed during day/night cycle.

electrically charged particles namely, ions and electrons, which affect the propagation of radio waves. The charged particles are mainly due to the solar radiation. The ionosphere approximately starts at an altitude of 50 km and extends to an altitude of 1100 km. Ionization primarily depends on the Sun activity. As a result, there is a diurnal (time of day) effect and a seasonal effect. Also, the activity of the Sun varies during a solar cycle with a period of 11 years. Apart from periodical changes, there are also mechanism that disturb the ionosphere such as solar flares or activities in Earth's geomagnetic field.

As mentioned before, ionization in the ionosphere changes depending on the day of time and different layers of ionization are observed. Distinct layers are denoted by the D, E, F_1, F_2. Typically, at night F_2 layer is the only layer at which significant ionization present. During the day, D and E layers are also ionized and F_1 layer with weaker ionization is also observed. Typical height depending on day of time are depicted in Fig.2.2.

These layers could be easily observed on ionogram data and reconstructed electron density profile. Such an example is shown in Fig.2.3.

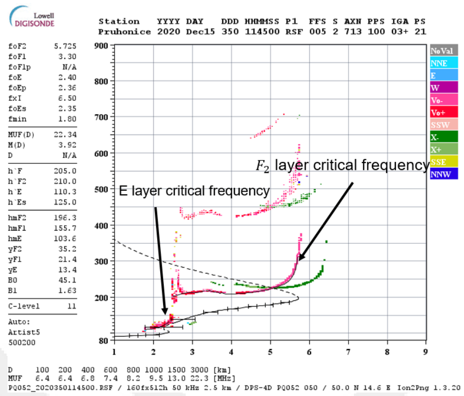

(a) Day time ionogram where E and F_2 layers are visible.

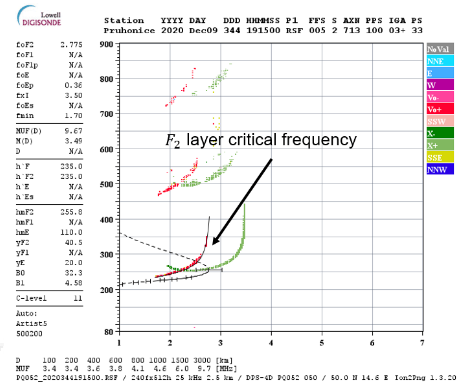

(b) Night ionogram where only F_2 layer echoes are visible

Figure 2.3: Ionosonde data for two different times of day and the observed layers of the ionosphere.

2.2 Remote Sensing Instrument:Ionosonde

An ionosonde or chirpsounder, is a special radar system designed for the monitoring of the ionosphere. Ionosonde transmits modulated pulses in HF band and record their *virtual height* to obtain the ionogram plot for the ultimate goal of reconstructing the electron density profile. To do that, ionosonde might operate in two different modes, namely, vertical mode depicted in Fig.2.4a and oblique mode depicted in Fig.2.4b. In the vertical mode, reflected echoes from the ionosphere are detected whereas in the oblique scenario, refracted signals from the ionosphere are detected.

The first study in the history that described the remote sensing of the ionosphere is given by Breit and Tuveit [20] in 1926. Since then, ionosondes become very important remote sensing instruments and each generational leaps brought significant improvements with the developing technology. The original analog ionosondes started to be replaced with digital counterparts in 1970s. Today, modern digital ionosondes that incorporates latest capabilities of RF circuitry and digital signal processing are used in ionospheric remote sensing. Two such examples are The Canadian Advanced Digital Ionosonde (CADI) which is shown in Fig.2.5a and the Digisonde Portable Sounder 4D (DPS-4D) which is shown in

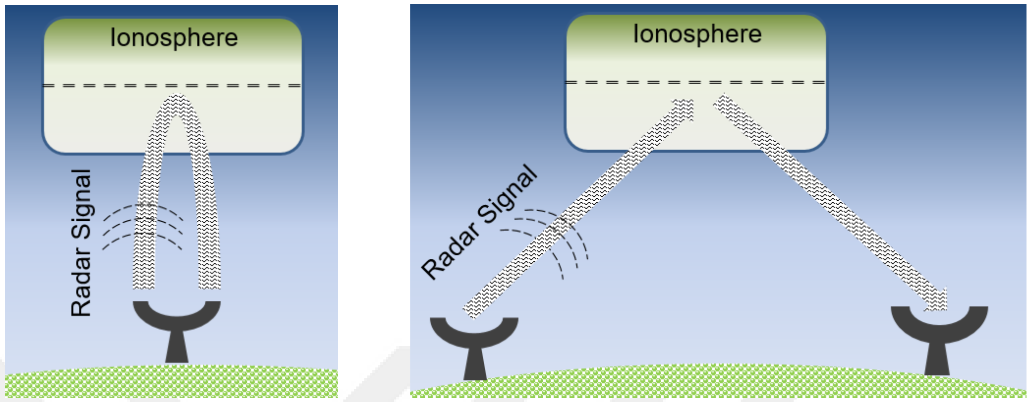

(a) Vertical Operation Mode (b) Oblique Operation Mode

Figure 2.4: Two modes of ionosonde operation.

Fig.2.5b.

DPS-4D developed by University of Massachusetts Lowell Center for Atmospheric Research (UMLCAR) currently have the largest ionosonde network over the globe at 90 stations in different locations [1]. Moreover, the data that is obtained from DPS-4D ionosonde located in Pruhonice, Czech Republic is used in this study. Hence, it is worth detailing the capabilities and specifications of DPS-4D here. Information about the DPS-4D given here are obtained from the user manual of the DPS-4D given in [1].

DPS-4D ionosonde can simultaneously measure the following parameters of the received echoes from the ionosphere.

- **Frequency**: Frequency parameter is actually not directly measured from the echoes. Instead, frequency interval set by the ionosonde operator is swept and returning echoes are detected.
- **Range**: Round trip delays of the received echoes are converted to the *virtual height* assuming that propagation at 3×10^8 m/sec.
- **Amplitude**: Amplitude of returning echoes are measured.
- **Phase**: Phase measurements are used when super-resolution direction technique is employed in Drift mode operation.

(a) The Canadian Advanced Digital Ionosonde (CADI)

(b) Digisonde Portable Sounder 4D (DPS-4D)

Figure 2.5: Modern ionosonde hardware.

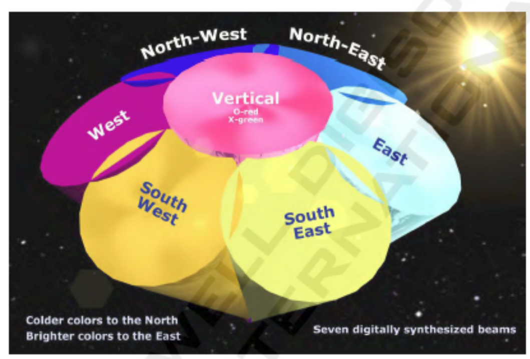

Figure 2.6: Digital beams formed by the DPS-4D.(Image taken from the user manual of DPS-4D given in [1].)

- **Doppler Shift and Spread**: Radial velocity of the off-vertical echoes received from the ionosphere is related the radial velocity of the plasma structure.

- **Angle of Arrival**: DPS-4D uses a receiving array of 4 crossed loop antennas. Depending on the operation mode, DPS-4D uses either super resolution direction finding or synthesize the beams shown in Fig.2.6 using digital beamforming techniques. Spatial filtering ability enables to suppress unwanted radio interference. Moreover, transmitter antennas illuminate very large portion of ionosphere and reflections can be received from different angles. Using the digital beamforming technique, echoes impinging on the receiving array with vertical angles can be filtered for more reliable scaling in vertical operation mode. Similary, in oblique operation, unwanted signals can be eliminated.

- **Wave Polarization**:Receiving antennas can be switched to left and right hand circularly polarized modes to observe ordinary and extraordinary waves.

Electron density distribution of the ionosphere affect the propagation and reflection dynamics of the radio waves and by measuring the aforementioned parameters it is possible to reconstruct the underlying electron density distribution. Measured parameters are plotted on the ionogram which is shown in Fig.2.7. Ionogram plot contains virtual heights, which are simply obtained by converting time delay to range assuming free space propagation speed of 3×10^8 m/s, versus frequency. Also, in Fig.2.7, it can be observed that the left column includes autoscaled parameters that are calculated by the ARTIST software [21] which is the standard software that is deployed with DPS-4D. ARTIST also reconstruct the underlying electron density distribution which is denoted by $N(h)$ profile in Fig.2.7.

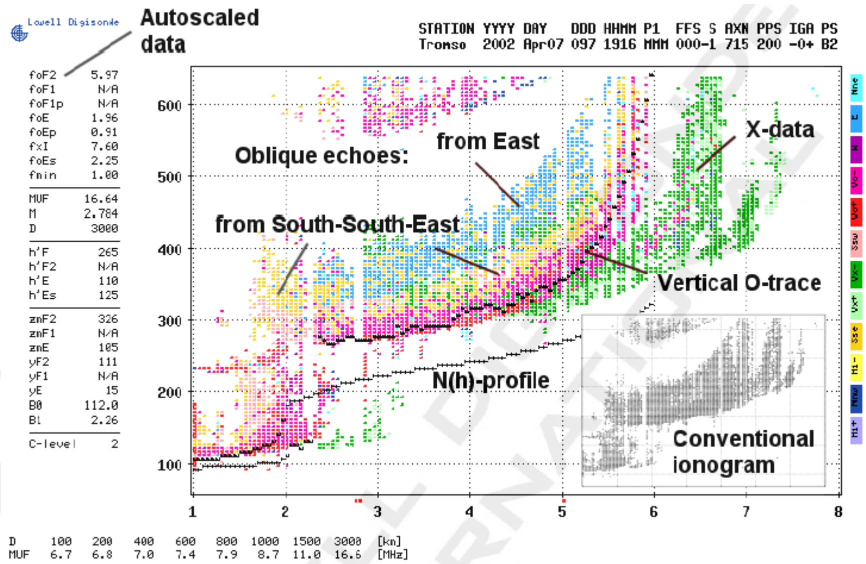

Figure 2.7: Ionograms are plots of frequency vs virtual reflection height. Green dots shows the extraordinary polarization, red dots shows the ordinary ray traces. The angle of arrival is shown with different colors. The left side of the figure contains autoscaled parameters that are obtained by the ARTIST software of the electron density distribution. (Image taken from user manual of the DPS-4D given in [1].)

2.2.1 Relation Between Electron Density Profile and the Ionosonde Data

In the vertical operation mode of the ionosonde, an electromagnetic wave pulse (wave pocket) with frequency f propagates vertically toward the ionosphere and if it encounters high enough electron density matching the frequency of transmission, the pulse reflects back. A pulse radio signal with finite duration at the position of transmission $z = 0$ can be represented by inverse Fourier relation as:

$$E(t) = \int_{-\infty}^{\infty} F(f) e^{j2\pi f t} df. \tag{2.1}$$

At height z, the can be written as [18]:

$$E(t, z) = \int_{-\infty}^{\infty} F(f) \exp\left(j2\pi f (t - \frac{1}{c} \int_0^z \mu dz) \right) df, \tag{2.2}$$

where μ is the phase refractive index given by the famous Appleton-Hartree dispersion relation [18]. Ignoring the electron collision effect, refractive index for the

$$\mu^2(f,h) = 1 - \frac{X(1-X)}{1 - X - \frac{1}{2}Y^2\sin^2(\theta) + \sqrt{(\frac{1}{2})Y^2\sin^2(\theta) + (1-X)^2Y^2\cos^2(\theta)}} \quad (2.3)$$

$X = \frac{w_p^2}{w^2}$ $\qquad$ $Y = \frac{w_H}{w}$

$w_p = 2\pi f_0 = \sqrt{\frac{N_e(h)e^2}{\epsilon_0 m_e}}$ $\qquad$ $w_H = 2\pi f_h = \frac{B_0|e|}{m_e}$

w_p : Plasma frequency.

ϵ_0 : The free space permittivity.

m_e : Mass of an electron

θ : Angle between the magnetic field vector and the wave vector.

w_H : The gyro frequency.

B_0 : Magnitude of the magnetic field vector.

e : Electron charge.

$N_e(h)$: Electron density distribution.

---

left hand circularly polarized (Ordinary Ray) can be calculated by using (2.3).

Using the (2.2), ionosonde signal can be evaluated for any f and z. However, depending on the time and position of the transmission, magnitude of the signal $E(t,z)$ is larger than 0 for those values of z which gives the position of the transmitted pulse at time t. Using this property, position of the pulse at time t can be determined by finding the z value that makes $|E(t,z)|$ large. Typically, transmitted signal with spectrum $F(f)$ is usually a signal with a constant frequency f_1. Using this assumption, $|E(t,z)|$ is large when frequencies close to the dominant frequency f_1 has all the same phase. This requires that,

$$\frac{\partial}{\partial f}\left\{ft - \frac{1}{c}\int_0^z \mu f dz\right\}\bigg|_{f=f_1} = 0. \quad (2.4)$$

Hence the position of the pulse is given by

$$t - \frac{1}{c}\int_0^z \left\{\frac{\partial}{\partial f}(\mu f)\right\}\bigg|_{f=f_1} dz = 0. \quad (2.5)$$

Let U_z denote the upward velocity of the pulse. Then, (2.5) shows that

$$\frac{c}{U_z} = \left\{\frac{\partial}{\partial f}(\mu f)\right\}\bigg|_{f=f_1} \quad (2.6)$$

The ratio of c/U_z is called as the *group refractive index* and denoted by $\mu^{'}$ which is given by:

$$\mu' = \frac{\partial}{\partial f}(\mu f) = \mu + f\frac{\partial \mu}{\partial f} \tag{2.7}$$

Substituting (2.3) into (2.7), group refractive index can be obtained as [18]:

$$\mu^{'}(f,h) = \frac{1}{\mu} + \frac{1 - X - \mu^2 + 0.5Y^2\cos^2(\theta)(1-X^2)(1-\mu^2)(Y^2\cos^2(\theta)(1-X)^2 + 0.25Y^4\sin^4(\theta))^{-\frac{1}{2}}}{\mu\left(1 - X - \frac{1}{2}Y^2\sin^2(\theta) + \sqrt{(\frac{1}{4})Y^4\sin^4(\theta) + (1-X)^2Y^2\cos^2(\theta)}\right)} \tag{2.8}$$

In terms of the group refractive index $\mu^{'}$, the upward velocity of the pulse U_z can be written as:

$$U_z = \frac{c}{\mu^{'}}. \tag{2.9}$$

Then, half of the round trip delay can be calculated by integrating the inverse of the upward velocity U_z of the pulse as:

$$\tau(f) = \int_0^{h_r(f)} \frac{1}{U_z}dh = \frac{1}{c}\int_0^{h_r(f)} \mu^{'}(f,h)dh\ , \tag{2.10}$$

where $h_r(f)$ is the real reflection height at which the electron density reaches to the critical value and the group velocity reaches to zero, i.e, $\mu(h_r(f), f)^{'} = 0$. For the ordinary ray, this condition can be simplified as:

$$X(h) = \frac{N_e(h)e^2}{\epsilon_0 m_e(2\pi f)^2} = 1\ . \tag{2.11}$$

Under the assumption of propagation at the free space propagation speed, the virtual height measured by the ionosonde becomes:

$$h^{'}(f) = c\int_0^{h_r(f)} \frac{1}{U_z}dh = \int_0^{h_r(f)} \mu^{'}(f,h)dh\ \ . \tag{2.12}$$

The integral given in (2.12) forms the foundation of the relationship between the ionogram and the vertical electron density profile. Moreover, it can be observed that the electron density reconstruction problem or the ionogram scaling can be thought as an inverse problem where $h^{'}(f)$ in (2.12) are measured by the ionosonde and and the underlying electron density $N_e(h)$ is reconstructed.

Relation between the electron density profile and the virtual height measurements have two important aspects. First, when the electron density profiles are inserted into (2.12), result of the integral typically can not be calculated analytically and numerical approaches must be used. Second, the integrand of (2.12) tends to infinity at the upper bound of the integral which requires special treatment to calculate the integral numerically which will be addressed in the next section.

2.3 Literature Review

Polynomial Analysis program, POLAN [22], is the first attempt that aims to give consistent results without an operator intervention. The POLAN uses polynomial with any desired degree to model the electron density profile and obtain a weighted least square solution for the polynomial parameters to reconstruct the electron density profile. Today, the most widely used automatic tool is the Automatic Real Time Ionogram Scaler with True Height (ARTIST) [23]. ARTIST program is deployed as a part of the Digisonde Data [21] processing system and it uses NhPC [24] algorithm to obtain the electron density profile. During the scaling process, NhPC expresses the electron density profile of each layer as shifted Chebyshev polynomials and the set of coefficients are calculated to reconstruct the electron density profile [24].

Although ARTIST is considered as the state of the art today, ionogram scaling is a highly challenging task. As discussed in [5], comparisons reveal that ARTIST is able to provide reliable scalings for about 93% of the time which indicates that there is a room for improvement. As a result, researchers are trying different techniques for ionogram scaling. Such an attempt is the *Autoscala* technique given in [25] which adjust the parameters of a model that generates a candidate electron profile and root mean square error between the recorded ionogram and calculated ionogram is minimized. In [7], an effort is made to improve the *Autoscala* by proposing a method for calculating the simulated ionogram for a given electron profile in a fast and robust manner.

Apart from the complete true height analysis, some methods focus on only estimating the critical parameters of the electron density profile or propose pre/post-processing techniques that could improve the results of existing scaling tools. For example, in [26, 27], a method for estimating critical frequency parameter *F2* layer and *E* layer are presented respectively. Recently, a new technique that is proposed in [28] which estimates the critical frequency of the F2 layer using the image processing technique proposed in [29]. In [30, 31], signal processing techniques for clearing artifacts and noise like components that are commonly observed in ionograms are proposed. In [32], an expert system called QualScan is proposed to survey and assign a quality factor to the outputs of the ARTIST in order to highlight unreliable scalings. In a similar study given in [33], a method for identifying incorrect scalings that are usually observed under disturbed conditions is proposed.

Chapter 3

Automatic Ionogram Scaling and Electron Density Reconstruction

Many inverse problems in signal processing can be cast as an optimization problem in terms of the parameters of a model as:

$$\hat{x} = \underset{\boldsymbol{x} \in \boldsymbol{X_f}}{\arg\min}\ J(\boldsymbol{y}, f(\boldsymbol{x}))\ , \tag{3.1}$$

where $\boldsymbol{y} \in \mathbb{R}^n$ is the vector of measurements, $\boldsymbol{x} \in \mathbb{R}^m$ is the vector of model parameters, $f : \mathbb{R}^m \to \mathbb{R}^n$ is the model function, $J : \mathbb{R}^{n \times n} \to \mathbb{R}$ is the function measuring the fitness between the model output and the measurements and $\boldsymbol{X_f}$ is the model parameter space which can be used to denote the feasible solutions or limit the search space to utilize some prior information about the measurements. In the optimization scope, there are two main types of constructed problems. In the first class, constructed problems are convex and its global optimizer can be efficiently found by using computationally efficient and fast convex solvers. The second class contains non-convex problems. For such cases, there are efficient algorithms to find the locally optimum solutions but finding the global optimizer usually results in high computational cost. Such an example is the Particle Swarm Optimization (PSO) which aims to find the global optimizer of non-convex problems [34].

In this chapter of the thesis, a novel technique, Ionogram Scaling and Electron Density reconstruction (ISED) is proposed. The ISED is a two stage algorithm that obtains the electron density profile by constructing an inverse problem such as the one given in (3.1). In the first stage of the ISED, actual echoes from the measurements are identified where the prior information about the characteristics of the ionospheric reflections and measured amplitudes of echoes are utilized by an (HMM) [35,36]. Then, the critical frequency of the ionogram, f_oF2, is estimated by using the extracted echoes. With the help of pre-processing in the first stage, the second stage of the ISED provides the electron density profile by constructing an optimization problem such as the one given in (3.1), in terms of the h_mF2 parameter. The proposed optimization problem is solved by using the Golden Section search method [37] and the h_mF2 parameter is estimated as the solution of the constructed model based on nonlinear optimization. The best electron density profile that fits to the recorded ionogram is obtained and the automatic scaling process is completed.

Performance of the ISED is demonstrated over a large data set of real ionosonde measurements that are obtained between the dates of 10-Jan-2015 and 02-June-2015 at a representative midlatitude ionosonde station located in Pruhonice, Czech Republic with geographic coordinates of [50^oN, 14.5^oE].

The outline of this chapter is as follows. In Sec.3.1, calculation of the ionograms for a given electron density profile is given. In Sec.3.2, an electron density profile model known as IRI-Plas is introduced. In Sec.3.3, the details of the proposed ISED technique is given. In Sec.3.4, results obtained using ionosonde measurements are given to demonstrate the performance of the proposed technique. Also, results are compared with the state of the art ARTIST technique. In Sec.3.5, some additional results that are obtained under disturbed ionospheric conditions are given to show the capabilities of ISED when ionograms are hard to resolve. In Sec.3.6, conclusions for this chapter are drawn.

3.1 Ionogram Computation for a Given Electron Density Profile

In Section 2.2.1, relation between the ionogram and the vertical electron density profile is given in detail. Relation between the ionogram, $h^{'}(f)$ and the refractive index $\mu^{'}(h,f)$, which is a complicated function of electron density profile given in (2.3), is given by:

$$h^{'}(f) = c \int_{0}^{h_r(f)} \mu^{'}(h,f)dh \quad . \tag{3.2}$$

where $h_r(f)$ is the real reflection height for frequency f, which can be simplified for ordinary ray as:

$$X(h) = \frac{N_e(h)e^2}{\epsilon_0 m_e (2\pi f)^2} = 1 \ . \tag{3.3}$$

Unfortunately, the integral given in (3.2) does not have a closed form expression. Also, some models that will be introduced later in this chapter provide numerical data for $N_e(h)$ which requires computation of the integral numerically.

Moreover, the integral given in (3.2) has a singularity at the upper bound, i.e., $\lim_{h\to h_r(f)} (1/n(h)) = \infty$ which can create numerical issues. Here, an adaptive Gauss-Kronrod quadrature (GKQ) [38,39] is used for the numerical computation of (3.2). The GKQ method expresses the integral of $f(x)$ as $f(x) = w(x)g(x)$ to improve the accuracy of the results. Furthermore, implementation detailed in [39] includes adaptive splitting of regions to improve the accuracy and enables the calculation of sub integrals in a parallel scheme which reduces the computation time of the integral. Details of the adaptive algorithm based on GKQ is given in Appendix A.

To demonstrate the accuracy of the adaptive GKQ, it can be compared with the Riemann Sum method. Chapman Layers model [40] which can be written as:

$$N_e(h) = \sum_{m=1}^{M} N_m \exp\left\{1 - \frac{h-h_m}{H_m} - \exp\left\{-\frac{h-h_m}{H_m}\right\}\right\} \quad , \tag{3.4}$$

can be used to generate synthetic electron density profile. In (3.4), M is the

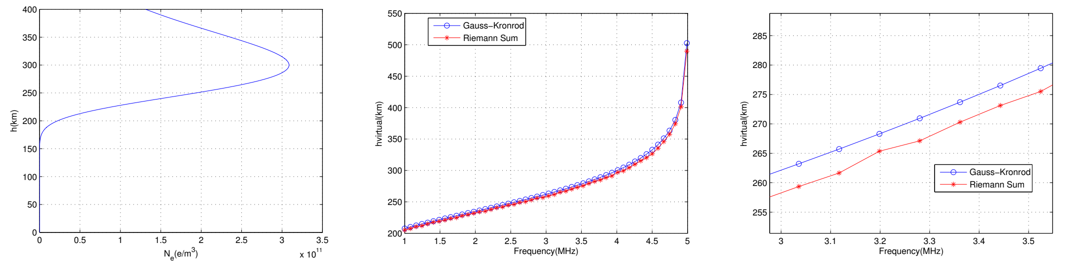

(a) Electron Density Profile (b) Ionogram Trace (c) Ionogram Trace-Close-up View

Figure 3.1: The chapman electron density profile and the corresponding ionogram traces computed by the Gauss-Kronrod quadrature and the Riemann Sum approximations.

number of layers, N_m is the maximum electron density of the m^{th} layer occurring at h_m and H_m is called as the scale height that adjusts the layer widths.

In Fig.3.1, the electron density profile for a single layer with the form given in (3.4) is shown along with the corresponding ionogram traces that are calculated using by both using Riemann Sum approximation and the GKQ. During the evaluation of the integral with Riemann Sum approximation, function is evaluated at integral interval is split into 10^4 points. For the adaptive GKQ, tolerance value is set to 10^{-6}. Results show that the Riemann Sum approximation underestimates the result of the integral as it discards the contribution of the values close to the singularity point. It can also be observed that the Riemann Sum results are not as smooth as those of the GKQ. In fact, accuracy of the Riemann Sum approximation can also be improved by splitting the integration interval into higher number of sub-intervals. But this is actually what the adaptive GKQ method does, adaptively splitting sub-intervals when needed.

3.2 IRI-Plas Electron Density Profile Model

The most commonly used electron density profile model is the International Reference Ionosphere (IRI) model [41, 42], which has been steadily updated as the new data and techniques have been available over time [43, 44]. IRI is a joint task group of the Committee on Space Research (COSPAR) and the International Union of Radio Science (URSI) which is dedicated to provide reliable and accurate climatic models for the ionospheric parameters [41–44].

IRI model can provide the electron density profile $N_e(h)$ for a given location, date and time from 80 to 2000 km in altitude. IRI is highly successful in representation of the general structure of the ionosphere, yet it requires modification in order to provide ionospheric parameters that are necessary for monitoring the space weather and tracking of the ionospheric disturbances in near-real time [45]. Recently, an extension of the IRI model, International Reference Ionosphere extended to Plasmasphere (IRI-Plas) [46, 47] has been introduced. IRI-Plas is extended to the 20,000 km altitude, which is the orbital height of the Global Positioning System (GPS) satellites. Moreover, IRI-Plas has the capability of ingesting parameters such as the Total Electron Content (TEC), h_mF2 and f_0F2 as an input for further scaling the electron density as described in [45, 48].

In Fig.3.2, the electron density profiles of IRI-Plas for 3 different parameter set of f_oF2, h_mF2 for 10-Jan-2015, 06:45 UTC are shown along with the computed ionogram traces using the method described in 3.1. Given electron density profiles are obtained at the location of Pruhonice Ionosonde Station, Czech Republic which has the geographic coordinates of [50.00^o N, 14.60^o E] and the geomagnetic coordinates of [49.34^o N, 98.57^o E].

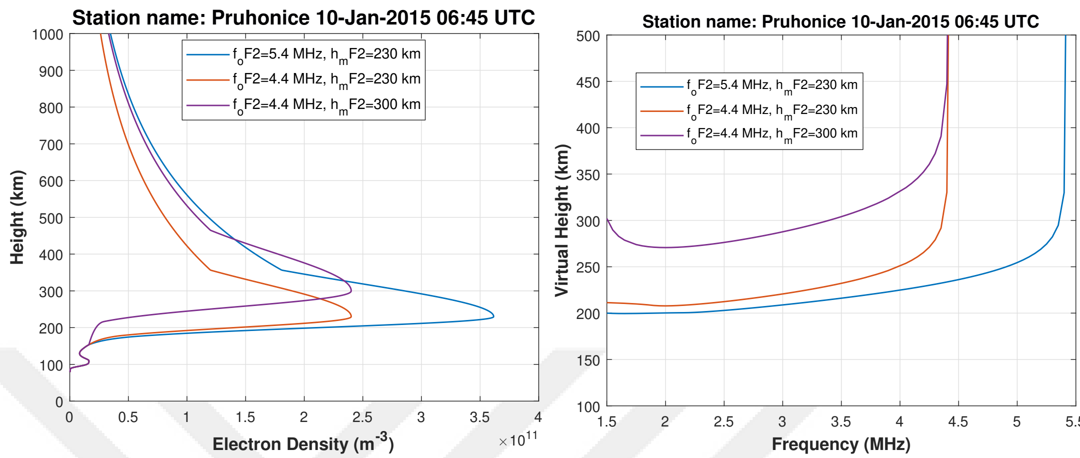

(a) Electron Density Profiles (b) Ionogram Traces

Figure 3.2: Electron density profiles of IRI-Plas and the corresponding ionograms that are obtained for Pruhonice Station, Czech Republic.

3.3 ISED: Ionogram Scaling and Electron Density Reconstruction

ISED is a two stage technique as shown in Fig.3.3. In the first stage of ISED, raw ionogram measurements are pre-proccessed by an HMM that is designed for the task of removing multi-hops and artifacts, hence extracting the actual echoes that are received as a result of the direct reflection from the ionosphere. Then, extracted echoes are used for estimating the critical frequency of *F2* layer which plays a crucial role in scaling. Then, a model based optimization problem is constructed that aims to find the best IRI-Plas electron density profile that fits the ionogram obtained by the HMM.

Outline of this section is as follow. In Sec.3.3.1, a signal model for the raw ionogram measurements are given.

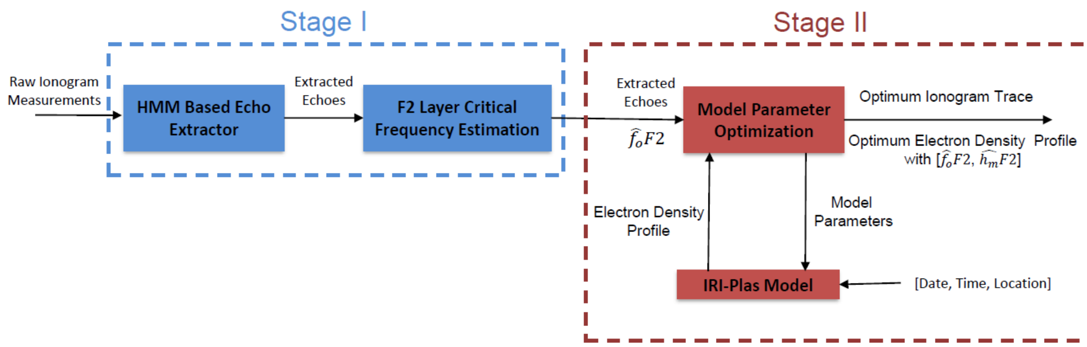

Figure 3.3: Flowchart of ISED

3.3.1 The Signal Model

The Digisonde DPS4-D [21] is one of the most widely used digital ionosonde that incorporates latest capabilities of the RF circuitry and digital signal processing. Operating frequencies of ionosondes are in between 1 MHz and 20 MHz where the frequency resolution is usually set manually by the ionosonde operator. It converts the round trip delays of the received echoes with a resolution of 2.5 km at each frequency [21]. Also, amplitudes of the received echoes are recorded if there is a detection in the corresponding range and frequency bin. Typically, the temporal resolution of ionosonde data is 15 minutes and frequency resolution of data is 0.025 MHz.

As stated in Sec.2.2, the DPS-4D has the ability of spatial filtering and measuring both the ordinary ray and the extra-ordinary ray by switching the polarization. Here, we only use the recorded detections of the ordinary ray which has the left hand circular polarization. Also, reflections detected at the output of the vertical beam, which is shown in Fig.2.6, are used alone to remove the possible interference and artifacts. Filtering operation for polarization and direction dimensions of the raw data that is utilized here is a common practice and also used in other scaling techniques [21].

After completing the aforementioned filtering operations, the raw ionogram measurements of the Digisonde DPS4-D consists of K distinct frequencies and N distinct virtual heights. These measurements are modelled using a matrix

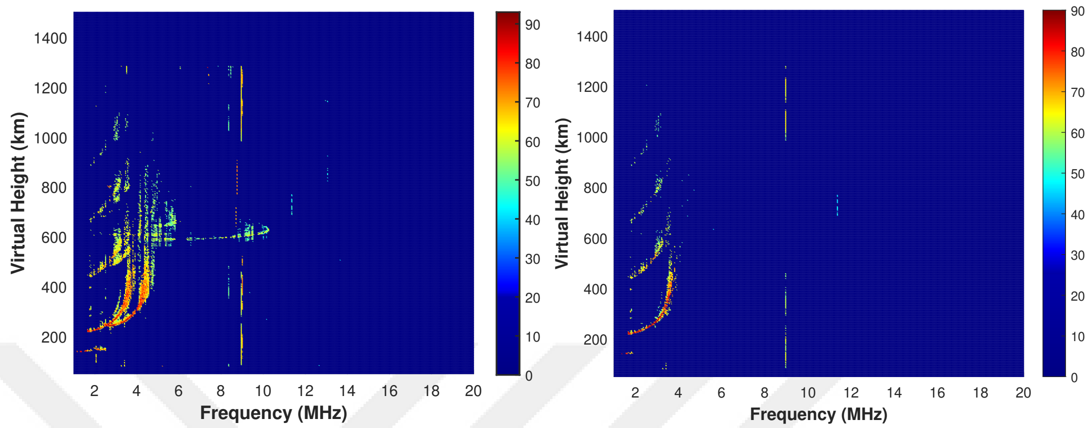

(a) Echo amplitudes prior to polarization and spatial filtering.

(b) Echo amplitudes after the polarization and spatial filtering.

Figure 3.4: Structure of $\boldsymbol{M}$ matrix before and after the filtering operation.

$\boldsymbol{M} \in \mathbb{R}^{K \times N}$ such that $M_{kn} = P_{kn}$ where P_{kn} is the measured power for the detection at frequency f_k, height h_n. For frequency and range bins where there is no detection, amplitudes are set to 0. An example of echo amplitudes are shown in Fig.3.4. It can be observed that, after filtering out the extra-ordinary ray and the directions except vertical reflections, the ionogram can be significantly cleared from artifacts, and echoes of the F trace can be observed clearly.

3.3.2 Brief Review of Hidden Markov Models

Signals that are investigated in remote sensing problems are generally results of some underlying real world processes. Depending on the application, acquired signals can be naturally discrete such that they are elements of a finite alphabet or naturally continuous such as samples of a room temperature. Also, depending on the application, signals can be pure or corrupted from other signal sources such as thermal noise or interference.

There are broadly two possible choices for signal modeling. First class consist of deterministic models where measured signals acquired from an instrument are modelled by using some well known properties. For example, signal could be a pure sinusoidal signal or sum of sinusoidal signals. In these cases, problem is usually estimating the model parameters of the signal. Second class consist of stochastic signal models where there is a low order statistical description on the signals are available. HMM is a stochastic model it is successfully applied to wide variety of signal processing applications including speech processing [35, 36, 49] and remote sensing [50–53].

HMM is useful in obtaining solutions to following problems:

- **Problem-1:** Given the observation sequence and the model, calculating the probability (or likelihood) of the observation sequence.
- **Problem-2:** Given the observation sequence and the model, finding the state sequence with the maximum likelihood.
- **Problem-3:** Adjusting the model parameters for a given state sequence and observation sequence.

In this thesis, we are mainly interested in Problem-2 where we relate the state sequence $Q = \{q_1, q_2, \dots q_F\}$ of an HMM with the actual echoes received from the ionosphere. Then, the most probable state sequence for the given ionogram observations O_i is obtained as the ionogram trace covering the actual echoes, i.e.,

$$\hat{Q} = \underset{Q=q_1,q_2,\dots q_t}{\arg\max}\, P[q_1, q_2, \dots q_t, O_1 O_2 \dots O_F | \lambda]. \tag{3.5}$$

In the next section, details of the proposed echo extraction technique based on the HMM is detailed.

3.3.3 HMM Based Echo Extraction

An HMM is defined by few model parameters called as states, state transition probabilities, observation probabilities and initial state probabilities. Significance of the aforementioned parameters and details related to ionogram echo extraction by using HMM are given in the following subsections.

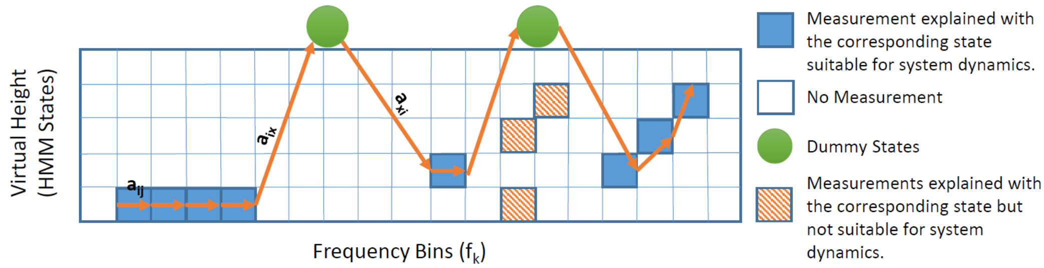

Figure 3.5: HMM visualization for echo extraction.

3.3.3.1 HMM States for Ionogram Echo Extraction

In order to adapt HMM to ionogram echo extraction process, we consider a system with N distinct states, $\boldsymbol{S_h} = \{S_1, S_2, \ldots, S_N\}$, where each state corresponds to the range bin h_n of the ionosonde. As discussed in Sec.3.3.1, DPS-4D ionosonde converts the round trip delays of the received echoes with a resolution of 2.5 km at each frequency. We assume that, in each measurement frequency, ionogram trace is in one of these states and by estimating the state sequence using the measurements will provide an accurate ionogram trace. Considering that most ionosonde measurements have frequency gaps as a result of weak reflections or local regulations which restrict transmissions at specific frequencies [32], we additionally define a set of dummy states $\boldsymbol{S_d}$. By using these dummy states, when there is a gap in the observations, model will proceed through the corresponding dummy states until it reaches to an appropriate measured echo as illustrated in Fig.3.5. Therefore, we choose the set of states as $\boldsymbol{S} = \boldsymbol{S_h} \cup \boldsymbol{S_d}$ for the HMM model.

3.3.3.2 HMM State Transition Probabilities

As illustrated in Fig.3.5, it is assumed that the modeled system undergoes a change of state at regular frequency intervals according to the system dynamics which are determined by the set of transition probabilities between states.

Let f_k denote the frequencies corresponding to state transitions and q_{f_k} denote the actual state at frequency f_k. For the ionogram echo extraction problem, we consider only the first order Markov Chains where the system dynamics are determined by just the current and the predecessor states, i.e.,

$$P[q_{f_k} = S_j | q_{f_{k-1}}, \ldots, q_{f_{k-2}}] = P[q_{f_k} = S_j | q_{f_{k-1}}] \tag{3.6}$$

Furthermore, we consider only frequency independent state transition probabilities:

$$a_{ij} = P[q_{f_k} = S_j | q_{f_{k-1}} = S_i], \quad 1 \leq i, j \leq N. \tag{3.7}$$

For simplicity, the matrix $\boldsymbol{A} = \{a_{ij}\}$ will be used to denote the state transition probabilities. Note that the state transition coefficients must obey the standard stochastic constraints:

$$\begin{aligned} a_{ij} &\geq 0, \\ \sum_{j=1}^{N} a_{ij} &= 1. \end{aligned} \tag{3.8}$$

To adapt an HMM to ionogram traces, larger transition probabilities are assigned for virtual heights that are close to each other so that the extracted ionogram traces are smoother. Also, HMM should not be able to jump to a state that is too far from the current state for improved robustness. Hence, state transition probabilities for the states where $(h_j - h_i) > 200$ are set to $a_{ij} = 0$. Assuming range resolution of adjacent states is 2.5 km, this condition corresponds to $a_{ij} = 0, \ \forall (i - j) > 80$. Moreover, ionogram traces are typically an increasing function of the frequency hence designed model should be encouraged to jump to a higher virtual height. Considering these properties along with the constraints given in (3.8), the transition probabilities between states in $S \in \boldsymbol{S_h}$ can be set as:

$$a_{ij} = \begin{cases} \gamma e^{-(|h_i - h_j|)/\beta} & , \text{ if } 0 \leq (j - i) \leq 80 \\ 0 & , \text{ otherwise.} \end{cases} \tag{3.9}$$

Here, γ is a normalization constant so that $\sum_{j=1}^{N} a_{ij} = 1$ and β is a constant to control how fast the transition probabilities attenuate as a function of altitude difference between the states.

We also need to define the transition probabilities for the dummy states that are defined to account for the frequency gaps in the measurements. Let i denote the index of the state in $\boldsymbol{S_h}$ and z denote the index of the dummy state in $\boldsymbol{S_d}$. Then, a_{iz} is chosen as:

$$a_{iz} = \begin{cases} 1/(2W+1) & , \text{ if } |i-z| \leq W \\ 0 & , \text{ otherwise.} \end{cases} \tag{3.10}$$

Here, W is a parameter controlling how far the model can jump between the dummy states and the actual states. Note that, we define $a_{iz} = a_{zi}$.

3.3.3.3 The Observation Probability Distribution

With the above definitions, if we can observe the set of states at each frequency instant, the corresponding stochastic model is called as an *observable Markov model*. However, this model is too restrictive to be applicable in many practical problems [35]. To overcome this issue, observations of the model can be defined as probabilistic function of the state.

In the proposed technique ISED, an HMM relates the state observation probabilities with ionogram amplitude measurement in a way that favors the virtual height states which has more powerful echo measurements. In other words, observation probability of a given ionogram measurement at frequency f_k in state j is chosen to be proportional to the echo amplitude for each virtual height as:

$$b_j(f_k) = P_{kj} \ . \tag{3.11}$$

Here, we assume that amplitude measurements of the ionosonde, P_{kj}, are normalized to satisfy $0 \leq P_{kj} \leq 1$. For simplicity, matrix $\boldsymbol{B} = \{P_{kj}\}$ will be used to denote the observation probabilities.

3.3.3.4 Probability Distribution of Initial the State

Initial states of the HMM correspond to the starting point of the ionogram trace at the minimum frequency which is typically around 1 MHz. As there are no previous echoes that the trace can be connected to, probability of the initial states, denoted by $\boldsymbol{\pi} = \{\pi_i\}$, determines the likelihood of each virtual height being the first state of the trace.

Our analysis on data shows that depending on the time of the day and the day of the year, virtual height of the first echo varies between $[90, 450]$ km range. As a result, initial state probabilities are assumed to be uniformly distributed in $h \in [90, 450]$ km.

3.3.3.5 Ionogram Trace Extraction using the Viterbi Algorithm

To identify the most probable sequence of states efficiently, the Viterbi algorithm can be used [54, 55]. First, define the highest probability along a single path at frequency f as:

$$\delta_f(i) = \max_{q_1, q_2, \cdots, q_{f-1}} P[q_1, q_2, \ldots q_f = i, O_1, O_2 \ldots O_f | \boldsymbol{\lambda}], \tag{3.12}$$

where $\boldsymbol{\lambda} = (\boldsymbol{A}, \boldsymbol{B}, \boldsymbol{\pi})$ denotes the set of HMM parameters given in the previous sections and O_k denotes the observations at frequency f_k. By induction, the highest probability at frequency f_{k+1} can be written as:

$$\delta_{f+1}(j) = \max_i \, [\delta_f(i) a_{ij}] b_j(f_{k+1}). \tag{3.13}$$

To obtain the optimum ML state sequence, argument which maximizes (3.13) can be tracked and the ML optimum state sequence with probability P^* in (3.18) can be determined using the Viterbi algorithm given in Algorithm 1. Viterbi algorithm obtains optimal state $q^*_{f_K}$ at the maximum frequency as given in (3.19) and back tracks the optimal state sequence using the variable Ψ_f given in (3.17) which is calculated at each frequency. In Fig. 3.6, the optimum state sequence tracked by the HMM is shown on as example.

3.3.4 The Electron Density Reconstruction

In the previous section, the HMM for ionogram echo extraction is defined. In order to complete the automatic scaling process, ionogram trace provided by the

Algorithm 1 The Viterbi Algorithm ($\boldsymbol{\lambda} = (\boldsymbol{A}, \boldsymbol{B}, \boldsymbol{\pi})$)

1: Initialization:

$$\delta_1(i) = \pi_i b_i(O_i), \quad 1 \leq i \leq N \tag{3.14}$$

$$\Psi_1(i) = 0. \tag{3.15}$$

2: Recursion:

$$\delta_f(j) = \max_{1\leq i\leq N}[\delta_{f-1}(i)a_{ij}]b_j(O_f), \qquad f_2 \leq f \leq f_K \quad 1 \leq j \leq N \tag{3.16}$$

$$\Psi_f(j) = \arg\max_{1\leq i\leq N}[\delta_{f-1}(i)a_{ij}], \qquad f_2 \leq f \leq f_K \quad 1 \leq j \leq N \tag{3.17}$$

3: Termination:

$$P^* = \max_{1\leq i\leq N}[\delta_{f_K}(i)] \tag{3.18}$$

$$q^*_{f_K} = \arg\max_{1\leq i\leq N}[\delta_{f_K}(i)]. \tag{3.19}$$

4: State Sequence backtracking:

$$q^*_f = \Psi_{f+1}(q^*_{f+1}), \quad f = f_{K-1}, f_{K-2}, \ldots, f_1. \tag{3.20}$$

HMM should be used to obtain the underlying electron density profile. To achieve this goal, first the critical frequency of the F2 layer, f_oF2 has to estimated which is detailed in Sec.3.3.4.1. Then, reconstruction of electron density is detailed in Sec.3.3.5.

3.3.4.1 Estimation of the Critical Frequency for F2 Layer

Critical frequency parameter of the F2 layer, denoted by f_oF2, is the maximum frequency at which an echo is received. Beyond this frequency, electromagnetic waves pass through the ionosphere without any measurable back scatter. Hence, accurate estimation of the f_oF2 plays a critical part in the reconstruction of the

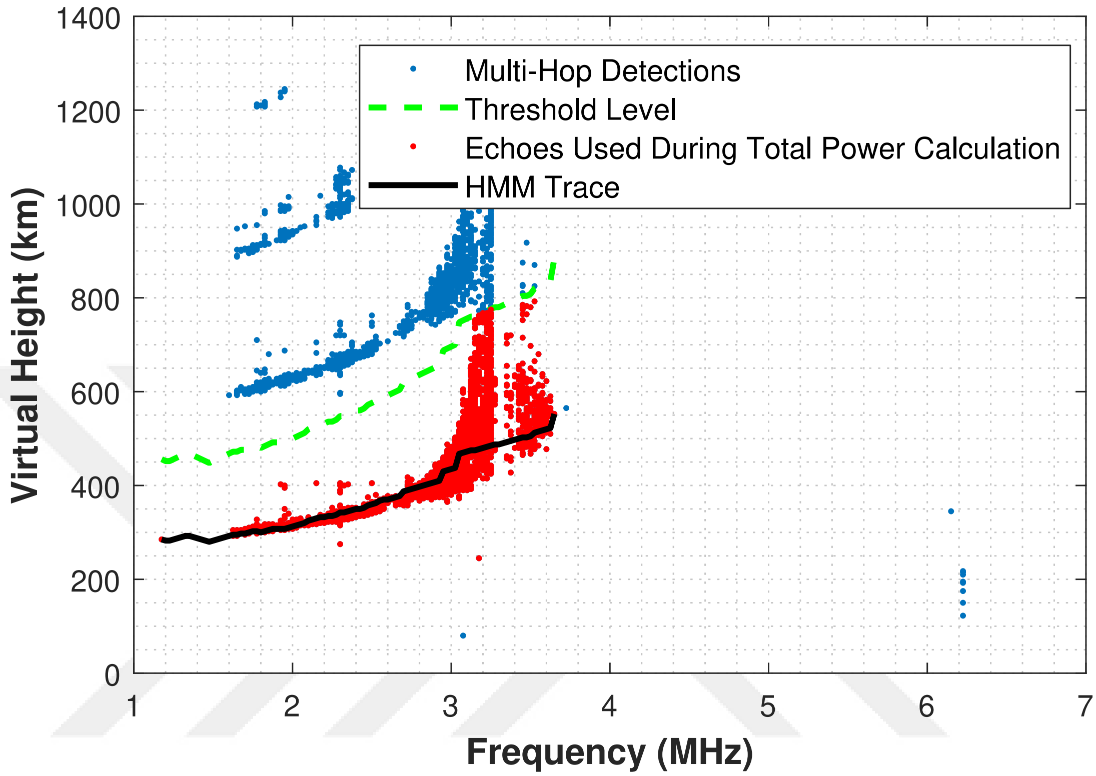

Figure 3.6: Calculation of threshold level for eliminating multihop reflections. (Pruhonice Station, 10-Jan-2015 00:45 UTC)

electron density. The tracking quality or the likelihood of the state sequence selected by the HMM also provides valuable information about the f_oF2 parameter. As shown in Fig.3.6, HMM tracks the correct echoes until the critical frequency. After the critical frequency, HMM tends to select echoes with higher measured amplitude and follow the echoes that spread both in frequency and height which decreases the likelihood of the state sequence. Unfortunately, there are other factors which also decreases the likelihood of a given state sequence such as frequency gaps in the measurements or weak echoes at different frequencies. As a result, tracking quality can not be directly employed by using the likelihood of a sequence given in (3.13). Instead, as a post-processing step, likelihood of the state sequence can be calculated by using (3.13) assuming that the observation probabilities for the chosen states are $\hat{b}_j(f) = 1$. Then, the coarse estimate of the critical frequency, $\widehat{f_o}F2_c$, can be found as:

$$\widehat{f_o}F2_c = \arg\min_f \ (\delta(f+1)/\delta(f)) \tag{3.21}$$

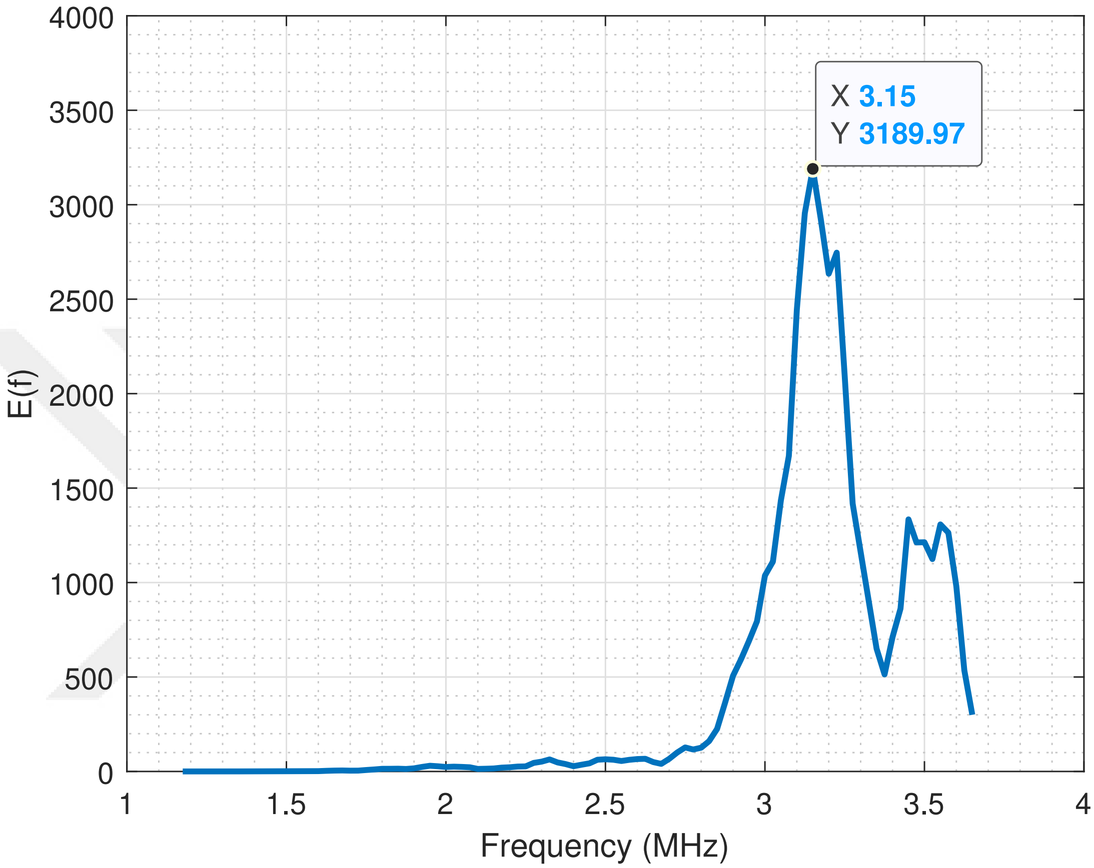

Figure 3.7: Total power for each frequency is obtained by integrating the received power for each frequency component. (Pruhonice Station, 10-Jan-2015 00:45 UTC)

In order to estimate f_oF2 accurately, the total received power at each frequency can be utilized. However, detections due to multihop reflections (multiple reflections from ionosphere and the surface of the earth) also affect the total received power at each frequency. For robust estimation of f_oF2, multihop detections that do not contribute to electron density reconstruction has to be removed. This can be achieved by using the ionogram trace generated by the HMM denoted by $h_H(f)$. For each frequency f, echo amplitudes in $\boldsymbol{M} = \{P_{fk}\}$ that satisfy the relation $k \geq T$ is set to 0 where $T = (\alpha \times h_H(f))$ denotes the threshold level. Here, $\alpha < 2$ should be satisfied to eliminate multihop reflections as they are observed at twice the height of the actual ionospheric reflection. This procedure is shown in Fig.3.6 for $\alpha = 1.6$.

Following the multihop removing process, total power at each frequency weighted with the coarse estimate is calculated as:

$$E(f_k) = \sum_{n=1}^{N} P_{kn}\, e^{-(f_k - \widehat{f}_o F2_c)^2} \;, \tag{3.22}$$

where N denotes the total number of observation heights. Then, f_oF2 parameter is estimated as:

$$\widehat{f}_o F2 = \underset{f_{max} - f_k \leq 2 \text{ MHz}}{\arg\max} \quad E(f_k) \tag{3.23}$$

where f_{max} is the maximum observed frequency in MHz. By imposing the constraint $(f_{max} - f_k) \geq 2$ MHz, we make sure that f_oF2 parameter estimation is robust against spurious measurements that are commonly observed at low frequencies.

After this step, $h_H(f)$ is modified so that the maximum frequency in the extracted trace is f_oF2.

3.3.5 Model Based Vertical Electron Density Reconstruction

In order to complete the automatic scaling process, underlying electron density distribution has to be reconstructed in a way that best fits to the extracted trace by the HMM. To do that, we take a model based approach. One of the most commonly used model is the IRI model [41, 42], which has been updated regularly as the new data and techniques available [43, 44]. Here, we employ the International Reference Ionosphere extended to Plasmasphere (IRI-Plas) [46, 47] due to the facts that the range of IRI-Plas is extended to the 20,000 km, which is the orbital height of GPS satellites, and also, IRI-Plas has the capability of ingesting TEC as an input for further scaling the electron density as described in [45, 48].

The optimization problem in terms of the IRI-Plas h_mF2 parameter is defined as:

$$(P1) \qquad \widehat{h}_m F2 = \underset{h_m F2}{\arg\min} \quad \sum_{k \in \boldsymbol{K}} \Big(h_H(f_k) - h_I(f_k, \widehat{f}_o F2; h_m F2) \Big)^2 . \tag{3.24}$$

Here, $h_H(f_k)$ denotes the trace extracted by the HMM and $h_I(f_k, \widehat{f}_o F2; h_m F2)$ denotes the IRI-Plas trace obtained for the given parameter set $\{f_k, \widehat{f}_o F2; h_m F2\}$ at the acquisition time of the data and the geographical location of the ionosonde.

Optimization problem given in (3.24) has a convex cost surface and it is a non linear function of the parameter $h_m F2$. By using the relation between the virtual height and the electron density distribution which is detailed in the Section 3.1, it can be shown that $h_I(f_k, \widehat{f}_o F2, h_m F2 + \delta h) \approx h_I(f_k, \widehat{f}_o F2, h_m F2) + \delta h'$. In other words, the IRI-Plas trace is shifted upward or downward as a function of the $h_m F2$ in a nonlinear fashion. This property is demonstrated on a specific example in Fig.3.8a. Using this property, the optimization problem in (3.24) can be solved by using a nonlinear convex optimization technique such as the Golden Section search [37]. The Golden Section search, given in Algorithm 3, can efficiently converge to the local minimum of the cost function given in (3.24). Cost surface for (3.24) and the function evaluation points of the Golden Section search are shown in Fig.3.8. Iterations of the Golden Section search algorithm are stopped when absolute difference between the left evaluation point l and the right r function evaluation points are smaller than $\epsilon = 0.1$. Our analysis on the ionograms show that, this condition is satisfied with less than 20 iterations. The value of cost function at each iteration and the difference $|l - r|$ is shown in Fig.3.9.

3.4 Results Obtained on Measured Ionosonde Data

The proposed ISED algorithm for the estimation of critical frequency and reconstruction of the electron density profile is applied to the raw ionogram outputs from a midlatitude station, namely, Pruhonice, Czech Republic, for the time

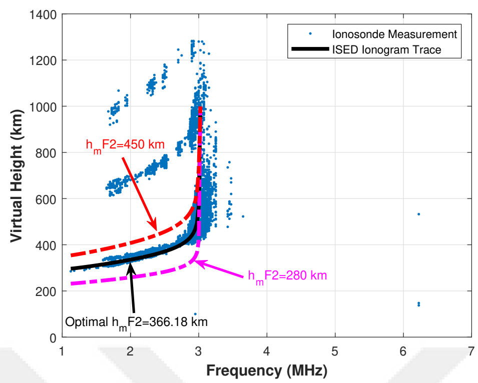

(a) Ionogram trace calculated for the optimal IRI-Plas solution that best fits the HMM trace. (Pruhonice Station, 10-Jan-2015 01:15 UTC)

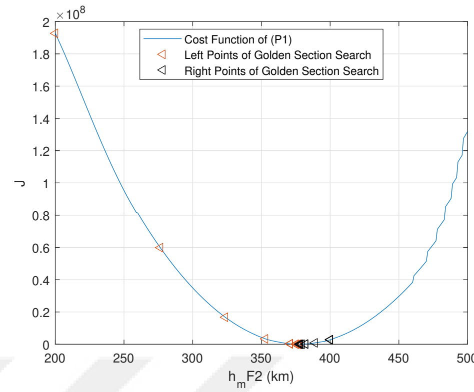

(b) Cost function of (P1) and cost function iterations of Golden Section search algorithm.

Figure 3.8: Optimal solution for h_mF2 parameter is obtained by using Golden Section search algorithm.

period between January 10, 2015 to June 2, 2015.

The ionosonde at Pruhonice (PQ052) is Digital Portable Sounder (DPS-4D) located at geographic coordinates 50.00^o N, 14.60^o E; geomagnetic coordinates 49.34^o N, 98.57^o E. The ionosonde produces raw ionograms and these ionograms are either manually scaled or automatically scaled by using ARTIST (version 5002). Typically, the temporal resolution of the ionosonde data is 15 minutes and the frequency resolution of the data is 0.025 MHz.

The ISED algorithm is applied to the raw ionograms and the F2 layer parameters, namely, f_oF2 and h_mF2, and also the vertical electron density profile are estimated as discussed in the previous section. For each application, electron density profile of the IRI-Plas algorithm is obtained for the given date and time of the measurement at the coordinates of Pruhonice ionosonde. The model outputs without any optimization and the corresponding simulated ionograms, which are calculated using by (2.12), are also included in the following figures to demonstrate the importance of the optimization step carried out by the ISED.

The ISED algorithm is applied to 13,812 ionograms and the algorithm outputs are compared with those of the ARTIST and non-optimized IRI-Plas (i.e.,

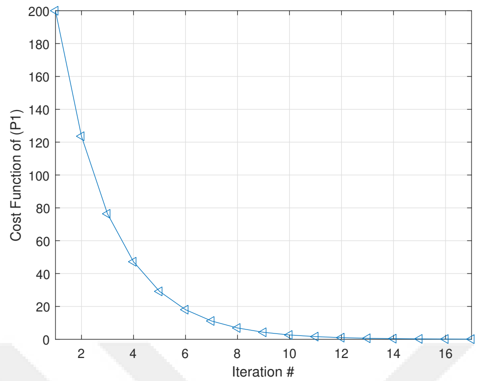

(a) Difference between left and right evaluation points for the ionogram given in Fig.3.8 in each iteration.

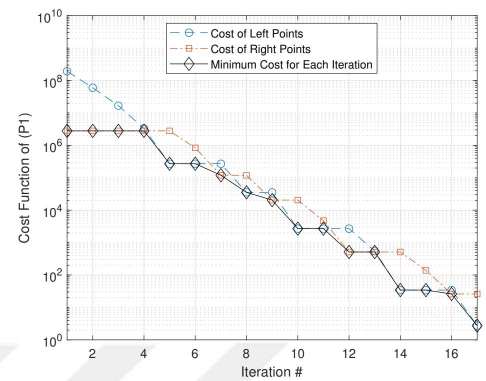

(b) Cost values of left, right evaluation points for the ionogram given in Fig.3.8 in each iteration.

Figure 3.9: Optimal solution for h_mF2 parameter is obtained by using Golden Section search algorithm.

with the default parameters). In 12,321 ionograms out of a total 13,812 ionograms (89.21 % of the total number of ionograms) the ISED and the ARTIST produced very similar outputs which are also consistent with the manually scaled ionograms. An example of such an ionogram is provided in Fig.3.14 where the F-layer returns (given in blue dots on raw ionogram) are spread in a wide range of frequencies on January 12, 2015 at 05:30 UTC. Here, both the ARTIST (red curve) and the ISED (black curve) traces follow similar tracks and resolve the spread-F ionogram. Similary, in Fig.3.12, both the ARTIST and the ISED successfully track E and F layer echoes and obtain similar electron density profiles as shown in Fig.3.13.

In 1,230 ionograms out of a total 13,812 ionograms (8.9 % of the total number of ionograms), the ISED is able to improve the results of the ARTIST. Such an example is shown in Fig.3.10. Similar examples can be easily identified in Fig.3.17 and Fig.3.16 where the estimated parameters of both the ARTIST and the ISED are shown for the first 1000 ionogram of the dataset. As it can be seen in these figures, the ARTIST algorithm estimates f_oF2 and h_mF2 parameters lower than expected whereas, the ISED successfully scales the ionograms.

2014 was the solar maximum year of 24th solar cycle so solar activity was

Algorithm 2 The Golden Section Search($[h_{min}, h_{max}]$, f, ϵ)

Set $k := 1$, $a_1 := h_{min}$, $b1 := h_{max}$, $\tau := \frac{\sqrt{5}-1}{2}$
$l := x_0 := a + (1-\tau)(b-a)$, $r := x_1 := a + \tau(b-a)$
Evaluate $f(l) := f(x_0)$
repeat
  Evaluate $f(x_k)$
  if $f(r) < f(l)$ **then**
    $a_{k+1} := l$, $b_{k+1} := b_k$, $l := r$
    $r := x_{k+1} := a_{k+1} + \tau(b_{k+1} - a_{k+1})$
  else
    $a_{k+1} := a_k$, $b_{k+1} := r$, $r := l$
    $l := x_{k+1} := a_{k+1} + (1-\tau)(b_{k+1} - a_{k+1})$
  end if
  $k := k + 1$
until $(b_k - a_k < \epsilon)$

slowing down in 2015. During the period from January 10 to June 2, there were about 10 geomagnetically disturbed periods including the severe St. Patrick's Day storm that extended from March 17 to March 22, 2015. In such cases, ionograms might become too complicated to scale for the automatic scaling techniques. Such an example is shown in Fig.3.18 where the F layer is completely disappeared and the results of the ISED and the ARTIST are not consistent.

Performance of automatic ionogram scaling techniques might get affected depending on the solar radiation that is caused by the Sun. Hence, their performance might change depending on the time of the year. Hence, it is important to know the performance of the techniques for different months and seasons. Monthly performance comparison between the ARTIST and the ISED is given for the time period January 2015 to May 2015 in Fig.3.19. Results indicate that, the ISED is able output improved scalings compared to the ARTIST in each month in our data set.

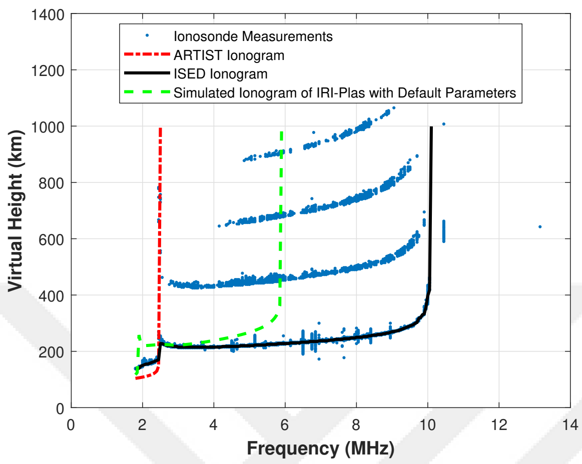

Figure 3.10: Ionosonde measurements and comparison of ionogram traces for Pruhonice Station, 12-Jan-2015 07:45 UTC.

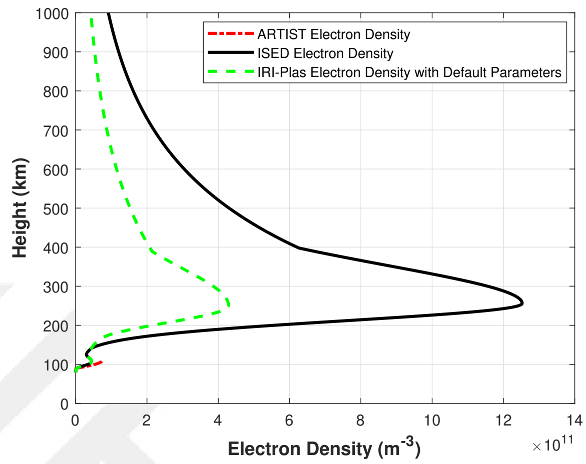

Figure 3.11: Comparison of reconstructed electron density profiles for Pruhonice Station, 12-Jan-2015 07:45 UTC.

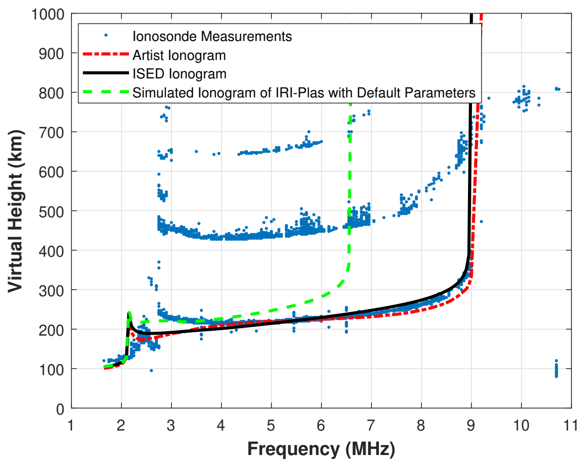

Figure 3.12: Ionosonde measurements and comparison of ionogram traces for Pruhonice Station, 11-Jan-2015 08:15 UTC.

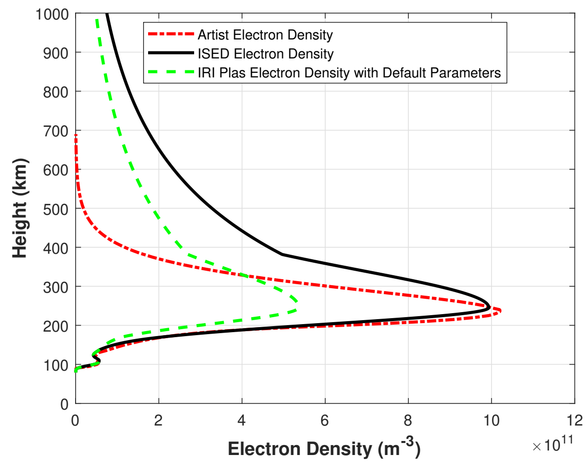

Figure 3.13: Comparison of reconstructed electron density profiles for Pruhonice Station, 11-Jan-2015 08:15 UTC.

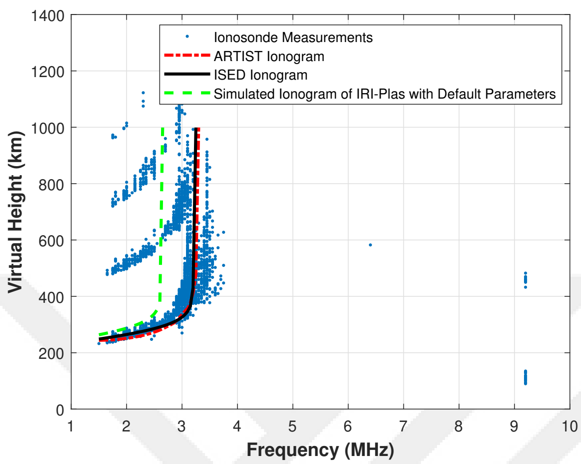

Figure 3.14: Ionosonde measurements and comparison of ionogram traces for Pruhonice Station, 12-Jan-2015 05:30 UTC.

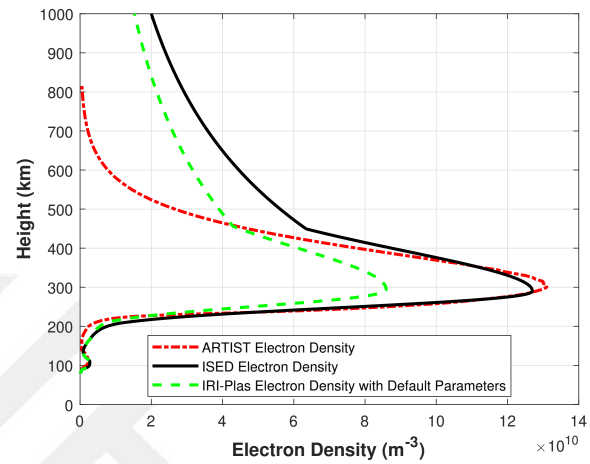

Figure 3.15: Comparison of reconstructed electron density profiles for Pruhonice Station, 12-Jan-2015 05:30 UTC.

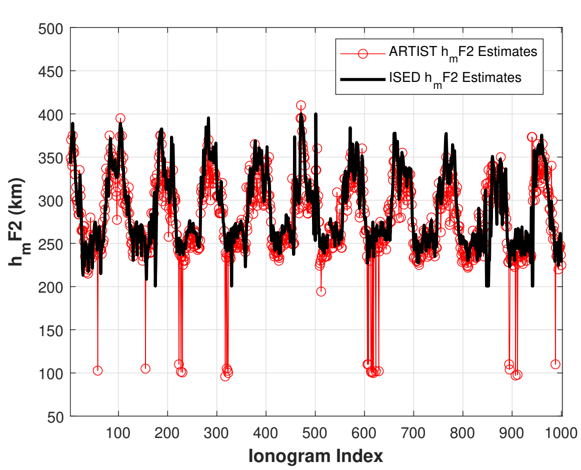

Figure 3.16: Estimated h_mF2 parameters for ARTIST and proposed method.

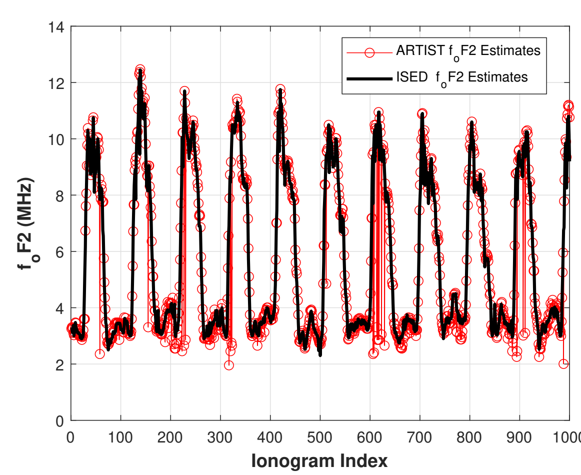

Figure 3.17: Estimated f_oF2 parameters for ARTIST and proposed method.

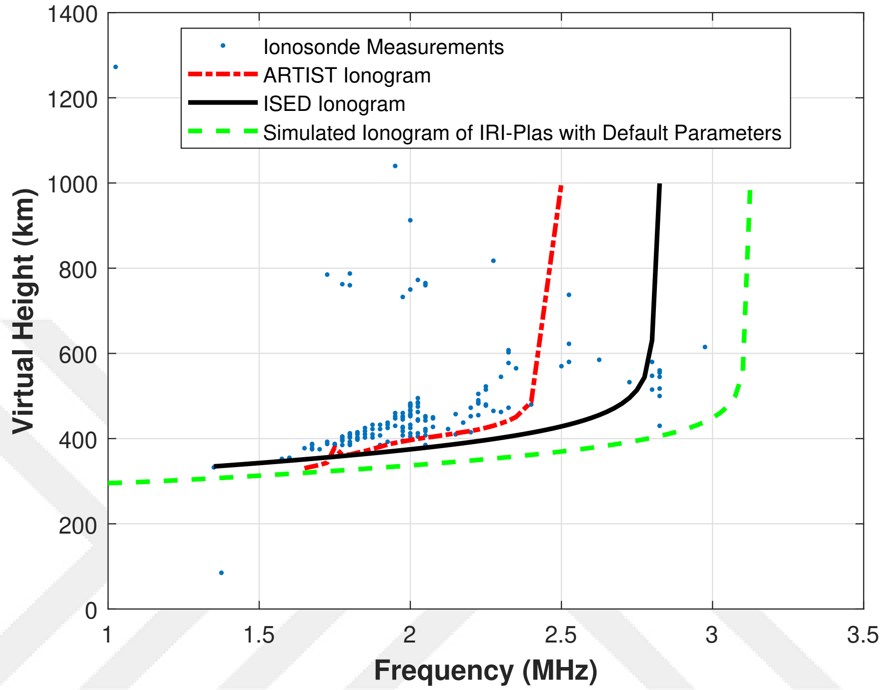

Figure 3.18: Ionosonde measurements and comparison of ionogram traces for Pruhonice Station, 19-Mar-2015 00:15 UTC.

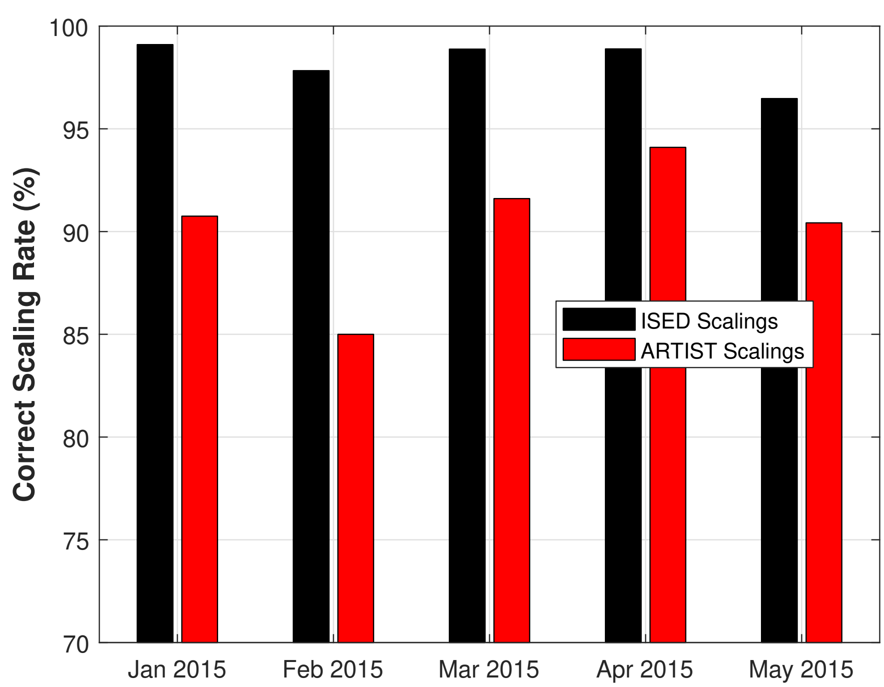

Figure 3.19: Monthly performance comparison between Jan-2015 to May-2015.

3.5 Results Obtained Under Disturbed Ionospheric Conditions

Performance of automatic scaling techniques under disturbed ionospheric conditions is an important figure of merit that shows the robustness and reliability. In this section, automatic scaling results for some important ionospheric storms that occurred in the first six months of 2015 are presented for the Pruhonice ionosonde station. The storm times are chosen using the geomagnetic three-hourly K_p index, which was introduced by J. Bartels in 1949 [56], [57]. It is designed to measure the solar particle radiation by its magnetic effects and it is considered a proxy for the energy input from the solar wind to the Earth. In Table. 3.1, selected dates depending on the K_p index for disturbed ionospheric conditions are given.

Table 3.1: Geomagnetic storms within January 2015-June 2015 [1].

Storm	Start Date (YYYY/MM/DD)	Peak Date (YYYY/MM/DD)	End Date (YYYY/MM/DD)
S1	2015/03/17	2015/03/18	2015/03/21
S2	2015/04/09	2015/04/10	2015/04/18
S3	2015/05/10	2015/05/11	2015/05/11
S4	2015/05/18	2015/05/19	2015/05/20

For the given storm dates, performance of the ARTIST and the ISED are compared for cases. For each storm, results can be summarized as:

- Fig.3.20, Fig.3.21 and Fig.3.22 are the examples for S1. In Fig.3.20 and Fig.3.22, the ARTIST fails to estimate $foF2$ parameter correctly whereas the ISED obtains acceptable results. The example provided in Fig.3.21 is a very controversial example F2 layer echoes are not clear.
- Fig.3.23 to Fig.3.26 shows examples for S2. In all of these examples, the ISED has a better performance compared to the ARTIST.
- Fig.3.27 to Fig.3.28 shows examples for S4. In these examples, the ARTIST identifies the E-Layer echoes as F2 layer and estimates the $foF2$ parameter

[1] Storm dates are obtained from '*https://www.izmiran.ru/services/iweather/storm/*' depending on their K_p indexes.

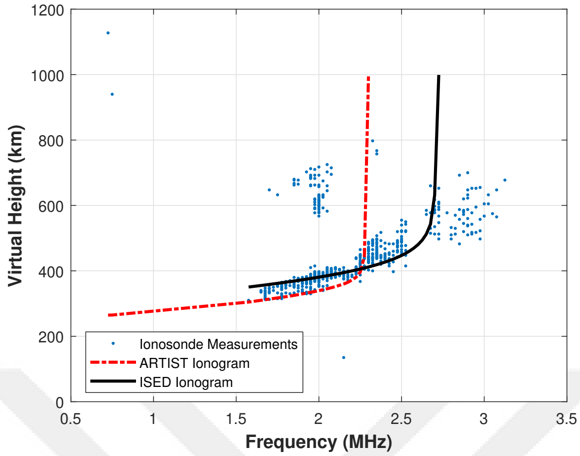

Figure 3.20: Ionosonde measurements and comparison of ionogram traces for Pruhonice Station, 18-Mar-2015 23:15 UTC. (S1)

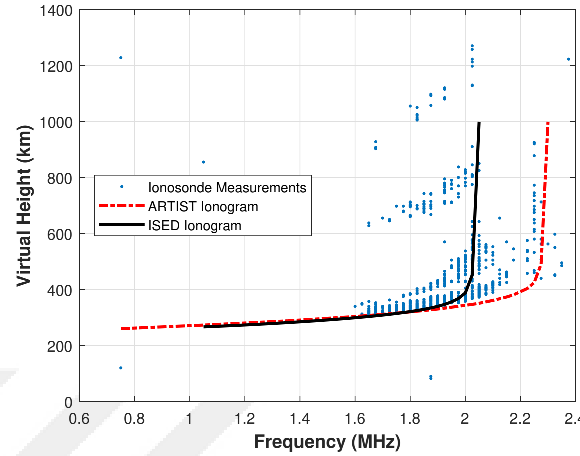

Figure 3.21: Ionosonde measurements and comparison of ionogram traces for Pruhonice Station, 19-Mar-2015 03:15 UTC. (S1)

much lower then it should be. However, the ISED correctly estimates $foF2$ parameter and successfully obtains the ionogram trace.

- Fig.3.29 shows an example for S5. Similar to the previous examples, th ARTIST's $foF2$ estimate is not correct whereas the ISED correctly scales the ionogram.

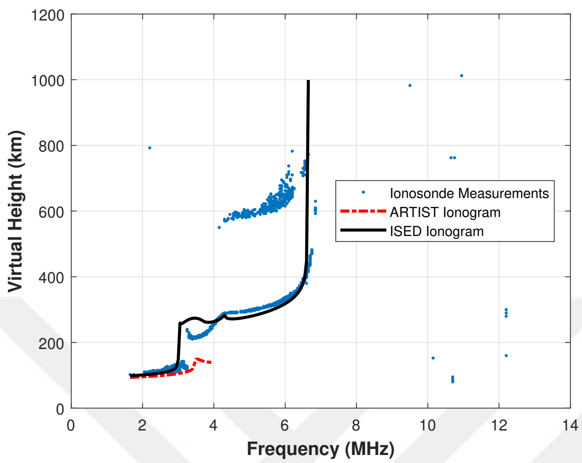

Figure 3.22: Ionosonde measurements and comparison of ionogram traces for Pruhonice Station, 19-Mar-2015 13:15 UTC. (S1)

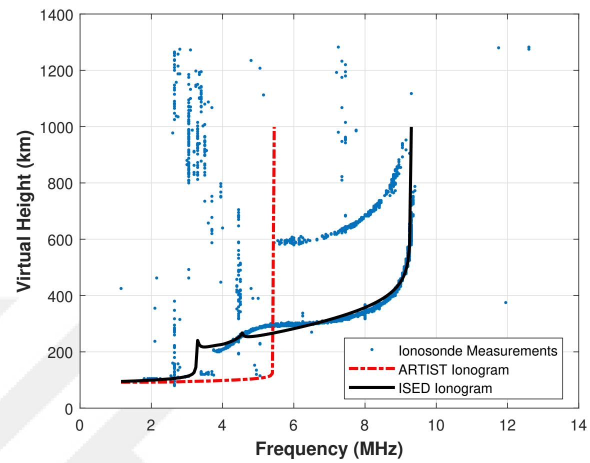

Figure 3.23: Ionosonde measurements and comparison of ionogram traces for Pruhonice Station, 09-Apr-2015 10:45 UTC. (S2)

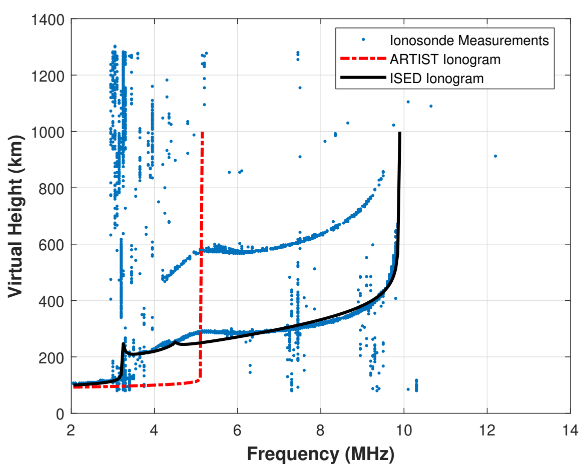

Figure 3.24: Ionosonde measurements and comparison of ionogram traces for Pruhonice Station, 09-Apr-2015 12:15 UTC. (S2)

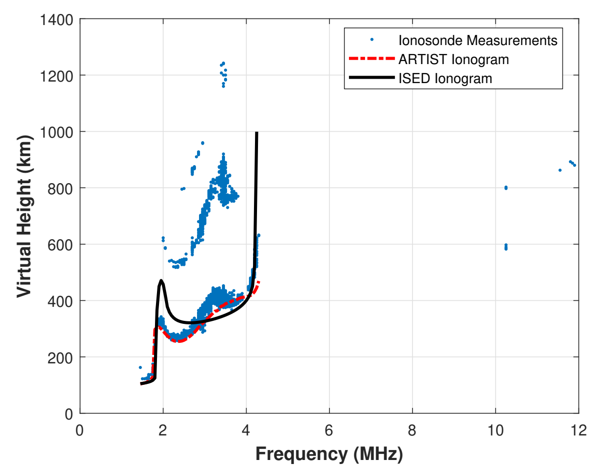

Figure 3.25: Ionosonde measurements and comparison of ionogram traces for Pruhonice Station, 10-Apr-2015 05:00 UTC. (S2)

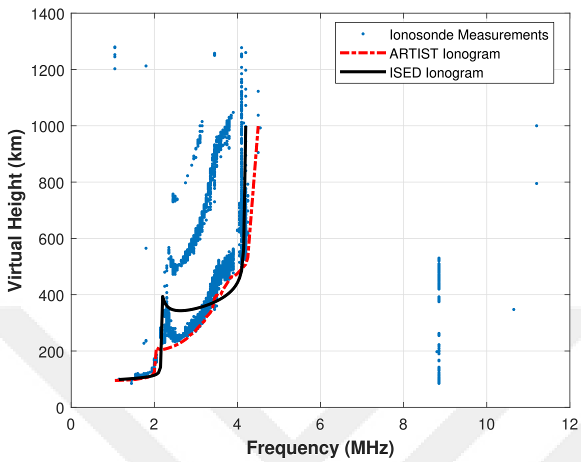

Figure 3.26: Ionosonde measurements and comparison of ionogram traces for Pruhonice Station, 10-Apr-2015 05:30 UTC. (S2)

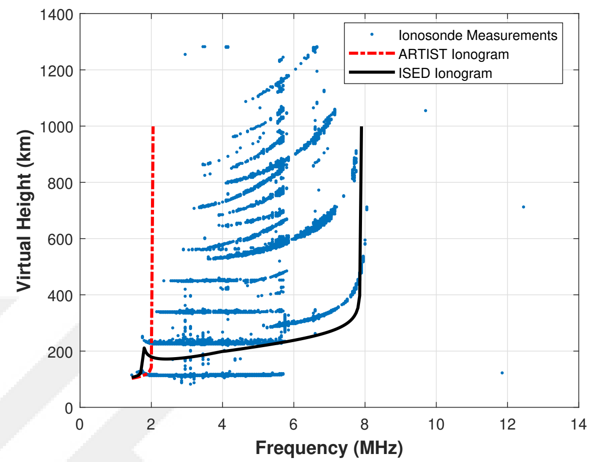

Figure 3.27: Ionosonde measurements and comparison of ionogram traces for Pruhonice Station, 14-May-2015 18:00 UTC. (S3)

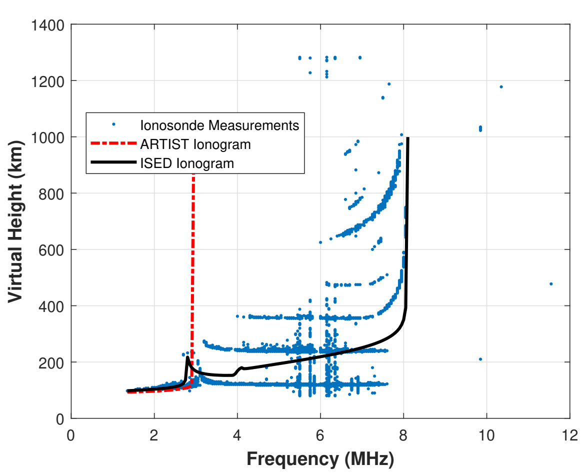

Figure 3.28: Ionosonde measurements and comparison of ionogram traces for Pruhonice Station, 16-May-2015 15:45 UTC. (S3)

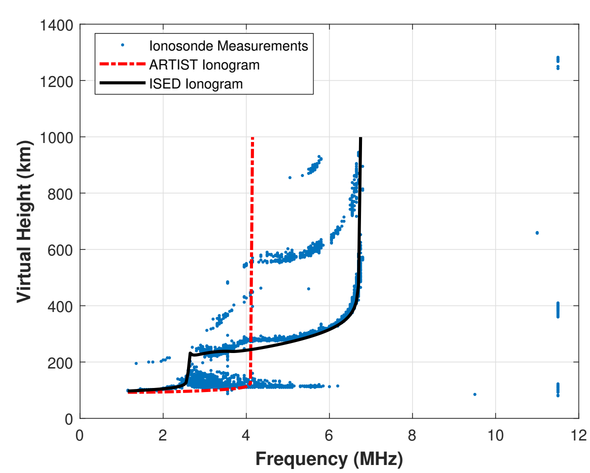

Figure 3.29: Ionosonde measurements and comparison of ionogram traces for Pruhonice Station, 31-May-2015 16:30 UTC. (S4)

3.6 Conclusions for Chapter 3

In this thesis, a novel algorithm, ISED, is proposed for ionogram scaling and electron density reconstruction. The ISED reconstructions are obtained in two stages. First, by using an HMM, the actual echoes in the ionosonde measurements are identified even if there are significant gaps in the data. Then, the electron density distribution profile is reconstructed by solving a model based optimization problem where the IRI-Plas trace with a set of estimated parameters at the data acquisition time and the geographical location of the ionosonde is used as the model. The performance of the ISED is evaluated by using 13,812 ionograms recorded at the midlatitude ionosonde station located in Pruhonice, Czech Republic. In 98.2 % of the available ionograms, it is observed that the ISED provides accurate electron density reconstructions, which is an improvement about 9 % over the ARTIST, which is the state of the art ionogram scaling technique.

Chapter 4

Electronic Intelligence and Specific Emitter Identification

Military operations are executed in an environment where the electromagnetic (EM) spectrum is becoming increasingly more complex. A wide variety of systems operating in the EM spectrum are being used in stand alone or in cooperative networks. Electronic Warfare (EW) includes all actions involving the use of EM to intercept, analyze, manipulate, or, suppress the adversarial use of the spectrum [58]. Vulnerability in EW could result with a loss in a battle without even making physical contact with hostile units.

The most critical part of EW is the radar electronic surveillance systems. These systems are traditionally grouped into three different categories as shown in Fig.4.1 [59]. First category, ELectronic INTelligence (ELINT), includes the process of observing and analyzing the signals transmitted by radar systems to obtain information about their capabilities. In other words, ELINT is the remote sensing of remote sensors [58, 60]. ELINT makes it possible to obtain valuable information while remaining remote from the radar and it is most valuable in hostile situations. It provides timely information about threatening systems such as radars guiding aircraft or missiles to targets or enemy defense systems, which might help penetrating those defenses. The second category is the Electronic

Support Measure (ESM) systems, which are mainly used for tactical purposes. In other words, the operator of ESM system relies on algorithms running on the system to produce an initial picture of the RF environment [59] and try to improve situational awareness by applying expert interpretation. The third category is the Radar Warning Receiver (RWR) systems specifically designed for instant response to protect naval and airborne platforms from radar threats.

Classification of radar threats is one of the most important functionality of radar electronic surveillance systems. Traditionally, radar remote sensing systems provides measurements on the following parameters for emitter recognition [61]:

1. Radio Frequency (RF),
2. Amplitude (Power),
3. Direction of Arrival (DOA) - also called Angle of Arrival (AOA),
4. Time of Arrival (TOA),
5. Pulse Repetition Interval (PRI),
6. PRI Type,
7. Pulse Width (PW),
8. Antenna Scan Type/Period (AST/ASP),
9. Lobe Duration (beam width),
10. Intentional Modulation on Pulse (IMOP).

Some of these parameters can be measured by using a single pulse. These parameters are referred to as monopulse parameters, which include RF, PW, DOA, amplitude and TOA. Other emitter parameters such as PRI, guidance and scan characteristics can only be obtained by using multiple pulses. The importance of these parameters for emitter identification is pointed out in [61] as shown in Table. 4.1.

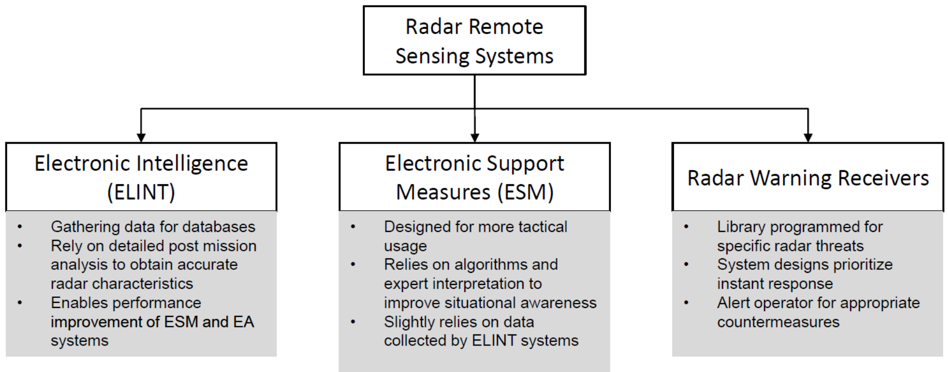

Figure 4.1: Radar remote sensing systems.

Table 4.1: The Importance of Various Emitter Parameters in the Processing of Radar Signals.

Parameter	Emitter Identification
Frequency	Very Useful
Amplitude	Not Useful
Angle of Arrival	Not Useful
TOA	Not Useful
PRI	Very Useful
PRI Type	Very Useful
PW	Some Use
AST/ASP	Very Useful
Beamwidth	Some Use
IMOP	Very Useful

However, in modern EW, emitter classification become a very challenging task as the number of emitters and their sophistication increased tremendously. Radars use different techniques to degrade detection and classification performance of EW systems. Hence, it becomes harder to classify radars by using traditional parameters. As a result, modern EW systems requires new approaches to improve detection and classification performance. Hence, detailed intra-pulse analysis of the received Intermediate Frequency (IF) signals becomes even more critical [60].

In the scope of this thesis, an ELINT problem known as Specific Emitter Identification (SEI), which aims to recognize individual emitters by using unintentional modulations on radar pulses, is investigated. SEI or Unintentional Modulation on Pulse (UMOP) is an approach which aims to recognize radar emitters by using precisely measured unintentional modulations on radar signals due to unintentional differences during the manufacturing of the transmitter hardware, including the power amplifiers and radar casing. In other words, UMOP is like a fingerprint of an emitter and can be used to even distinguish individual transmitters from the same manufacturing line.

Deployment of the SEI techniques has started in mid-1960s. Tracking and identifying unique transmitters was a high-priority problem for U.S government in that era [62]. Although most initial work was on feasibility of these systems, it resulted with successfully deployed SEI systems for different applications including all radio frequency bands, acoustic, magnetic strips and credit cards. Since then, SEI techniques have been used by the U.S government to identify specific emitters of interest for intelligence gathering or countermeasure activities. Specifically, in one program, the U.S government successfully tracked a specific emitter for more than 15 years using only the SEI techniques [62].

In the rest of this chapter, following topics will be investigated. In Sec.4.1, typical architecture of radar SEI systems, including receiver hardware design and signal processing steps are discussed. In Sec.4.2, existing work in the SEI literature is given.

4.1 Typical Radar SEI System Design

A typical system generally consists of few different subsystems as illustrated in Fig. 4.2 [62]. Radar signals are first captured by receiving antennas and pass through the RF subsystem prior to the analog to digital conversion. Then, typically a signal processing stage is used to prepare the signal for the SEI feature estimation. Finally, obtained feature set is used for the classification and the database is updated if necessary. In order to obtain a high SEI classification performance, all of these steps has different requirements and properties which are detailed in next subsections.

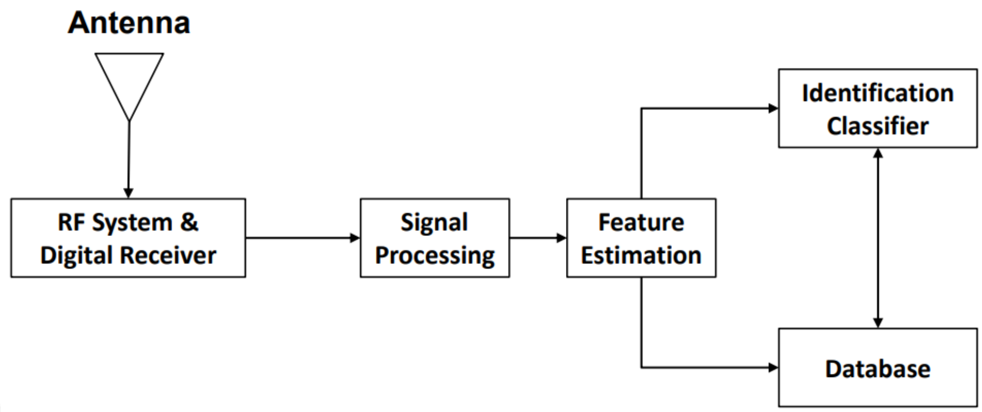

Figure 4.2: Typical system architecture for SEI.

4.1.1 RF System and Digital Receiver

Although there are different receiver architectures for radar EW systems, super heterodyne receivers are probably the best choice as the SEI relies on detailed waveform analysis [62]. The block diagram of a superhet receiver is shown in Fig.4.3. The RF subsystem usually compromises a set of RF downconverters to translate the incoming signal in frequency so that the signal can be digitized with an analog to digital converter (ADC) and captured by a digital receiver.

As SEI looks for subtle differences on the emitted signal, RF subsystem has stringent requirements in terms of signal distortion. In other words, samples of the emitters must be collected with little or no coloration by the collection system. To avoid coloring the data with receiver system, special care has to be taken to the signal path. The properties of a good SEI receiver is summarized in [62] as:

- Local oscillator phase noise must be as low as possible.
- All oscillators in the collection must be phased-locked to a common reference signal.
- The phase response of any bandpass filters must be as linear phase as possible.
- The number of bits in the ADC must be maximized to ensure sufficient

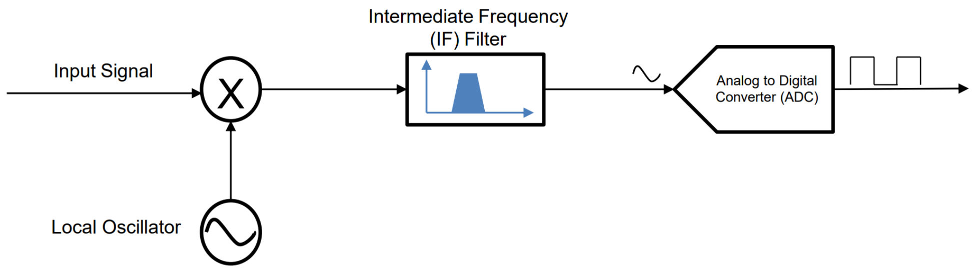

Figure 4.3: Super heterodyne receiver architecture for SEI.

dynamic range to extract SEI features.

- Signal-to-Noise Ratio (SNR) of the signals should be maximized for reliable identification.

The requirements given in [62] provides guidelines for the SEI system design but does not introduce strict numerical constraints which is the general case in the SEI literature. Most resources that can be found in the literature only demonstrate results with a limited data set and omits the effects of different receiving components such as local oscillator phase noise on the classification performance due to confidentiality. In the scope of this thesis, we try to address some of these questions which are valuable inputs for the SEI system architecture and the SEI receiver hardware.

4.1.2 Signal Processing Stage

In this stage, necessary signal processing steps are implemented to obtain robust and stable features. Depending on the application, received signals are filtered and demodulation is done before feature measurements. Similar to RF stage, if filters are to be used, coloration of the received signal should be minimal by using linear phase, finite impulse response (FIR) filters. Also, the filters should have little or no amplitude variation over the passband [63].

4.1.3 Feature Estimation

In this stage, defined signal features are calculated. This stage is probably the most important stage of a SEI system and requires special algorithms for different applications that enables the system to discriminate the subtle differences between the emitters. Hence, estimated features plays a crucial role in the performance of SEI systems.

During the feature development, it is important to know the correct identification of the emitters being evaluated, called *ground truth*. This is especially important when number of similar emitters is high in the data set. Another important aspect is that feature estimation algorithm should mitigate the multipath and noise effects that contaminate the signal for robust classification under different conditions [62].

Easiest way to evaluate the possibility of a feature set to be used in a system is to investigate the scatter plot of features for different emitters. Designed feature set should form natural clusters in feature space so that high classification performance can be reached [62]. Such an example is shown in Fig.4.4 where features occupy separate regions of the feature space and simple linear classifier can be used to discriminate the emitter set.

4.2 Literature Review

In the literature, there are several proposed techniques for SEI. In [64] and [65], the spectra of intercepted radar signals are used to generate features for the fingerprint analysis. In [66], non linear effects of power amplifiers are modelled and analyzed for the SEI. In [67], a complete SEI architecture is proposed where features are generated using higher order cumulants of radar signals and then k-Nearest Neighbor (kNN) classifier is then used to assign emitters to specific classes. In [68], basic SEI features related to characteristics of a square wave including the rise time, fall time and overshoot are discussed and, results for

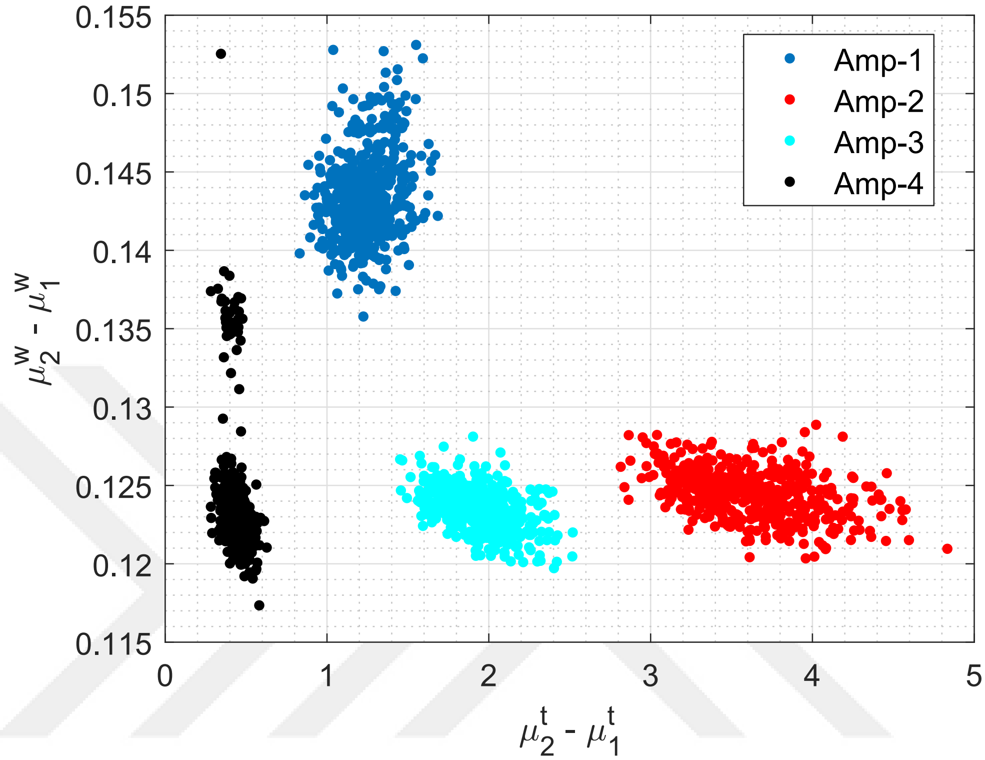

Figure 4.4: Set of example features which would provide good classification performance for 4 different classes.

a dataset consisting of two real radar signals are given. However, the details of feature extraction are not presented. Another approach employing Empirical Model Decomposition (EMD) [69] is introduced in [70]. Although the mod signals shown for two different emitters indicate variations, no further processing leading to automatic classification is presented. A common issue in the literature on radar SEI is the very limited use of real field data if not at all. Moreover, due to concerns of confidentiality, some critical steps of the proposed techniques are left out.

As stated in [62], SEI is not limited to identification of radar emitters. For example, in [71], effects related to oscillator phase noise of wireless devices are analyzed and used for classification. In [72–76], unintentional modulations related to the power amplifiers of communication systems are modelled using methods such as the Taylor series expansion, and results of the proposed algorithms are demonstrated in different communication scenarios and channels by using synthetically generated data. A new approach where the Hilbert spectrum of the received signal is fed into a deep residual network is introduced in [77] and results on single-hop and relaying communication scenarios are presented. Another machine learning based approach where the compressed bispectrum of the measured data is fed into a convolutional neural network is proposed in [78]. Yet again, these studies also lack results with real field data or do not provide any proof about the validity of the data generation models.

Chapter 5

A Method for Specific Emitter Identification

5.1 Introduction

In the scope of this thesis, we propose a novel and complete scheme for radar SEI. The proposed method consists of two main stages as shown in Fig. 5.1. In the first stage, preprocessing of the acquired radar pulses is performed to reveal the underlying unintentional modulations, which are very subtle for state of the art radar emitters of the same kind. For these emitters, pulse shapes of transmitters are usually very similar and differences could only be observed in a high Signal-to-Noise Ratio (SNR) regime that is not common in most practical EW scenarios. As a result, we propose a preprocessing scheme to integrate the pulses emitted by the same radar with the same carrier or radio frequency (RF). For successful integration, it is crucial to align collected pulses accurately in time and compensate for their phase offsets. In the proposed method, the collected samples of the acquired pulses are modelled as the discrete samples of a piece-wise continuous function [79]. Then, by choosing a reference pulse (typically the one with the highest SNR), the relative time delays between the reference pulse and all the remaining ones, which are far below the sampling interval of

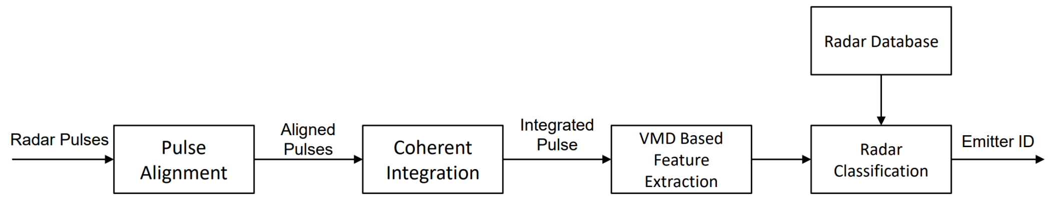

Figure 5.1: Flowchart of proposed SEI technique.

the receiver, are estimated by solving an optimization problem. Note that, since the pulses are modelled as a continuous function, the estimated time alignment delays are on a continuum rather than a fixed discrete grid, i.e., the estimation resolution is beyond the limit set by the sampling frequency of the Electronic Support Measures (ESM) receiver. The time aligned pulses are then coherently integrated to obtain a single pulse with improved SNR. In the second stage, SEI features are obtained by using Variational Mode Decomposition (VMD) [80]. The proposed feature extraction technique decomposes the envelope and instantaneous frequency of the radar pulses into components that have compact support in the frequency domain. A set of features characterizing these compact signals is then obtained and used for identification.

Outline of this chapter is as follows. In Sec.5.2, a method for time alignment of radar pulses is proposed. In Sec.5.3, experimental results for proposed pulse alignment technique is given. In Sec.5.4, proposed radar fingerprint extraction technique is introduced. Then, in Sec.5.5, overall computational complexity of proposed SEI technique is discussed. After that, in Sec.5.6, performance of the proposed technique is investigated on a dataset consisting of real radar measurements. Another performance analysis which explores the effect of phase noise of SEI receivers on the proposed technique is investigated in Sec.5.7. Finally, conclusions for this chapter are given in Sec.5.8.

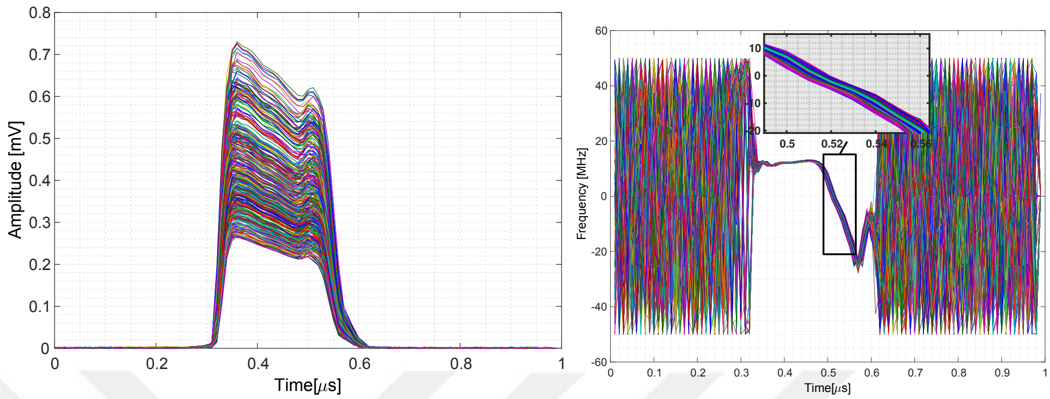

Figure 5.2: Envelopes (left) and instantaneous frequencies (right) of 383 real radar pulses.

5.2 Time Alignment of Pulses

Let $g_p(t), 1 \leq p \leq P$, represent P pulse signals emitted by the same radar with the same carrier frequency. The complex Inphase-Quadrature (IQ) samples of the p^{th} pulse measured by a digital ESM receiver with sampling rate F_s can be written as:

$$g_p(t_n) = a_p(t_n)e^{j\phi_p(t_n)} + z_p(n) \ , 1 \leq n \leq N_p, \tag{5.1}$$

where t_n is the sampling instance of the n^{th} sample, N_p is the number of collected samples, $z_p(n)$ is a sample of circularly symmetric complex white Gaussian noise with standard deviation σ_z. Here, $\phi_p(t_n)$ and $a_p(t_n)$ represent the instantaneous phase and the envelope of the pulse, respectively. For illustration, the envelopes and the instantaneous frequencies of $P = 383$ real radar pulses are shown in Fig. 5.2. Note that the instantaneous frequency can be approximated as:

$$f_p(t_n) = (\phi_p(t_n) - \phi_p(t_{n-1}))F_s/(2\pi). \tag{5.2}$$

As observed in Fig. 5.2 although these pulses are roughly aligned by the digital receiver according to their times of arrival (TOA), their instantaneous frequency curves appear to spread along the frequency axis at each t_n, which indicates imprecision in their alignment.

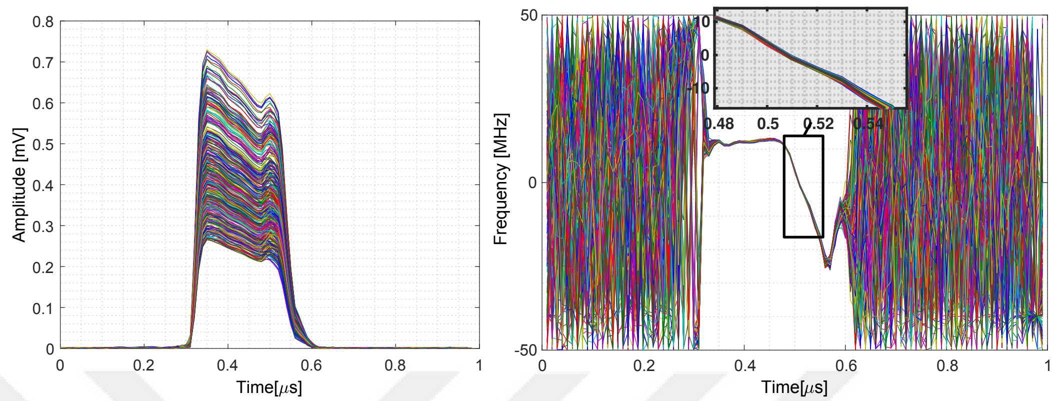

Figure 5.3: Envelopes (left) and instantaneous frequencies (right) of the aligned pulses, whose original versions are shown in Fig. 5.2.

Consider the following model for each pulse:

$$g_p(t_n) = c_p g_r(t_n - \tau_p) + z_p(n). \tag{5.3}$$

Here $g_r(t_n)$ is the reference pulse for the time alignment and amplitude/phase-offset correction procedures that will be implemented on the remaining pulses; τ_p is the time delay, and c_p is the complex coefficient controlling the amplitude/phase-offset. After estimating the c_p and τ_p parameters for each pulse, the integrated pulse with higher SNR can be formed as:

$$\hat{g}(t_n) = \frac{1}{P}\sum_{p=1}^{P} g_p(t_n + \hat{\tau}_p)e^{-j\angle\hat{c}_p}, \tag{5.4}$$

where $\angle(.)$ is the operator which returns the phase of its argument in radians. If all the c_p and τ_p parameters are estimated correctly, the standard deviation of the noise in the integrated pulse will be $\sigma_z/\sqrt{P}$. As a result, we can bound the effective SNR after the integration operation as:

$$\mathrm{SNR}_{\mathrm{min}} + 10\log_{10}(P) \leq \mathrm{SNR}_{\mathrm{eff}} \leq \mathrm{SNR}_{\mathrm{max}} + 10\log_{10}(P), \tag{5.5}$$

where $\mathrm{SNR}_{\mathrm{min}}$ and $\mathrm{SNR}_{\mathrm{max}}$ denote the SNR of the pulses with the highest and lowest SNR respectively. Hence, assuming that the amplitudes of all the pulses are about the same, the SNR increase would be $10\log_{10}(P)$ dB.

Assuming that r, $1 \leq r \leq P$, is the index of the reference pulse, and that the first K samples are used in alignment, define:

$$\mathbf{y}_{k,K} = [g_r(t_k), g_r(t_{k+1}), .., g_r(t_{k+K-1})]^T, \tag{5.6}$$

$$\mathbf{x}_{k,K} = [g_p(t_k), g_p(t_{k+1}), .., g_p(t_{k+K-1})]^T, \tag{5.7}$$

where $\mathbf{y}_{k,K}$ and $\mathbf{x}_{k,K}$ denote the vector of K complex samples of the reference pulse $g_r(t_n)$ and the p^{th} pulse $g_p(t_n)$, respectively. The relative time delay and complex scaling factor that compensates for the phase and amplitude difference between these two pulses can be obtained as:

$$[\tau^*, c^*] = \arg\min_{[\tau,c]} \|\mathbf{y}_{k,K} - c\mathbf{x}_{k,K}(\tau)\|_{l_2}^2, \tag{5.8}$$

where $\mathbf{x}_{k,K}(\tau) = [g_p(t_k + \tau), g_p(t_{k+1} + \tau), .., g_p(t_{k+K-1} + \tau)]^T$, and $\|.\|_{l_2}$ denotes the l_2 norm operator. For a given τ, the optimal value of c can be found as:

$$c(\tau) = \mathbf{x}_{k,K}(\tau)^H \mathbf{y}_{k,K} / \|\mathbf{x}_{k,K}(\tau)\|_{l_2}^2. \tag{5.9}$$

Hence, the required two-dimensional optimization in (5.8) reduces to a 1-dimensional optimization problem:

$$t^* = \arg\min_{\tau} \|\mathbf{y}_{k,K} - c(\tau)\mathbf{x}_{k,K}(\tau)\|_{l_2}^2 \ . \tag{5.10}$$

Since the cost function in (5.10) is non-convex, its cost surface might have multiple local minima. In terms of the sampling interval, $T_s = 1/F_s$, where F_s is the sampling frequency, τ can be written as:

$$\tau = \zeta T_s + \gamma T_s, \tag{5.11}$$

where $0 < \gamma < 1$ and $\zeta = \lfloor \tau / T_s \rfloor$, where $\lfloor . \rfloor$ denotes the flooring operator. In this expression, ζT_s is a coarse estimate of τ whose resolution is limited by the sampling interval of the receiver, and γT_s is a fine resolution correction.

For the estimation of these two parameters, we propose a two-stage algorithm that avoids getting trapped in a local minimum of the cost function given in (5.10). In the first stage, a coarse search is utilized for estimating ζ. In the second stage a fine search is utilized for estimating γ. In the subsections below, we detail these two stages.

5.2.1 Coarse Search: Estimation of ζ

Assuming that the fine resolution correction term is $\gamma = 0$ in (5.11), the cost function given in (5.10) can be written in terms of the coarse estimate ζ as:

$$f_\zeta(\zeta) \equiv -2\mathrm{Re}\{c(\zeta)\mathbf{y}_{k,K}^H \mathbf{x}_{k,K}(\zeta)\} + |c(\zeta)|^2 \|\mathbf{x}_{k,K}(\zeta)\|^2 \tag{5.12}$$

where $c(\zeta)$ is as in (5.9). Since $\zeta \in \mathcal{Z}$, $\mathbf{x}_{k,K}(\zeta)$ becomes:

$$\begin{aligned}\mathbf{x}_{k,K}(\zeta) &= \mathbf{x}_{k+\zeta,K}\\ &= [g_p(t_{k+\zeta}), g_p(t_{k+1+\zeta}), .., g_p(t_{k+K-1+\zeta})]^T.\end{aligned} \tag{5.13}$$

Since all the pulses are coarsely aligned according to their TOA values by the receiver, the cost function in (5.12) can be calculated over a limited interval $-\kappa \leq \zeta \leq \kappa$, and the minimum of the cost function $\bar{\zeta}$ can be found. Note that the coarse alignment term ζ given in (5.11) is smaller than the actual delay value τ, and that the fine resolution correction term γ is always positive. As a result, the coarse estimate value is computed as:

$$\hat{\zeta} = \lambda(\bar{\zeta}) = \begin{cases} \bar{\zeta} - 1 & \text{if } f_\zeta(\bar{\zeta} - 1) \leq f_\zeta(\bar{\zeta} + 1), \\ \bar{\zeta} & \text{if } f_\zeta(\bar{\zeta} - 1) > f_\zeta(\bar{\zeta} + 1). \end{cases} \tag{5.14}$$

5.2.2 Fine Search: Estimation of γ

In the coarse estimation stage of ζ, the time offset whose resolution is limited by the sampling interval is estimated. In the fine search stage, the coarsely-estimated time delay is updated in order to precisely align pulses beyond the sampling frequency, by minimizing the following simplified cost function:

$$f_\gamma(\gamma) = -2\mathrm{Re}\{c(\gamma)\mathbf{y}_{k,K}^H \mathbf{x}_{\hat{k},K}(\gamma)\} + |c(\gamma)|^2 \|\mathbf{x}_{\hat{k},K}(\gamma)\|^2 \, . \tag{5.15}$$

Here $c(\gamma)$ is as in (5.9), $\hat{k} = k + \hat{\zeta}$ and $\mathbf{x}_{\hat{k},K}(\gamma)$ is defined as:

$$\mathbf{x}_{\hat{k},K}(\gamma) = [g_p(t_{\hat{k}} + \gamma), g_p(t_{\hat{k}+1} + \gamma), .., g_p(t_{\hat{k}+K-1} + \gamma)]^T. \tag{5.16}$$

Algorithm 3 Proposed Two Stage Method

//Input: $\{g_r(t_n), g_p(t_n); n = 1, 2, .., N_s\}, k, K$
//Output: $\hat{\tau}, \hat{\zeta}, \hat{\gamma}$
//Constants: $\kappa = 5, \delta_\epsilon = 10^{-6}, i_{max} = 10$
//Initializations: $i = 0, \bar{\zeta} = 0, \hat{\gamma} = 0.5, \delta = 1$
//Coarse Search
for $\zeta = -\kappa : \kappa$ **do**
    if $f_\zeta(\zeta) < f_\zeta(\zeta)$ **then**
        $\bar{\zeta} = \zeta$
    end if
end for
$\hat{\zeta} = \lambda(\bar{\zeta})$
//Fine Search
while $i \leq i_{max}$ and $|\delta| > \delta_\epsilon$ **do**
    $\delta = -f'_\gamma(\hat{\gamma})/f''_\gamma(\hat{\gamma})$
    if $|\delta| > 0.5$ **then**
        $\delta = 0.5\text{sign}(\delta)/|\delta|$
    end if
    $\hat{\gamma} = \hat{\gamma} + \delta^i$
    $i = i + 1$
end while
$\hat{\tau} = \hat{\zeta} + \hat{\gamma}$

To obtain $\mathbf{x}_{\hat{k},K}(\gamma)$, a cubic spline interpolator on the available samples can be used [81]. To simplify the notation, let us define $\hat{\mathbf{x}} \triangleq [g_p(t_{\hat{k}}), g_p(t_{\hat{k}+1}), .., g_p(t_{\hat{k}+K})]^T$, whose entries are modeled as the discrete samples of the following continuous function:

$$s_{\hat{\mathbf{x}},n}(\gamma) = a_n + b_n\gamma + c_n\gamma^2 + d_n\gamma^3, \ 1 \leq n \leq K, \tag{5.17}$$

where $\gamma \in [0, 1]$. The spline parameters a_n, b_n, c_n, d_n are found by solving for $\mathbf{h}$ in the following linear system [81]:

$$\mathbf{A}\mathbf{h} = \mathbf{v}, \tag{5.18}$$

where $\mathbf{A} \in \mathcal{R}^{(K+1)\times(K+1)}$ and $\mathbf{v} \in \mathcal{C}^{K+1}$ are defined as:

$$\mathbf{A} = \begin{bmatrix} 2 & 1 & 0 & 0 & .. & 0 \\ 1 & 4 & 1 & 0 & .. & 0 \\ 0 & 1 & 4 & 1 & .. & 0 \\ . & . & . & . & . & \\ 0 & .. & 0 & 1 & 4 & 1 \\ 0 & .. & 0 & 0 & 2 & 1 \end{bmatrix}, \mathbf{v} = \begin{bmatrix} 3(\hat{\mathbf{x}}_2 - \hat{\mathbf{x}}_1) \\ 3(\hat{\mathbf{x}}_3 - \hat{\mathbf{x}}_1) \\ 3(\hat{\mathbf{x}}_4 - \hat{\mathbf{x}}_2) \\ \vdots \\ 3(\hat{\mathbf{x}}_{K+1} - \hat{\mathbf{x}}_{K-1}) \\ 3(\hat{\mathbf{x}}_{K+1} - \hat{\mathbf{x}}_K) \end{bmatrix}. \tag{5.19}$$

Here $\hat{\mathbf{x}}_i$ represents the i^{th} entry of $\hat{\mathbf{x}}$. Since the coefficient matrix $\mathbf{A}$ is tridiagonal, the linear system in (5.18) can be solved for $\mathbf{h}$ efficiently in $\mathcal{O}(K+1)$ complexity by using the Thomas Algorithm [82]. Then the spline parameters for $1 \leq n \leq K$ are obtained as [81]:

$$\begin{aligned} a_n &= \hat{\mathbf{x}}_n, \\ b_n &= \mathbf{h}_n, \\ c_n &= 3(\hat{\mathbf{x}}_{n+1} - \hat{\mathbf{x}}_n) - 2\mathbf{h}_n - \mathbf{h}_{n+1}, \\ d_n &= 2(\hat{\mathbf{x}}_n - \hat{\mathbf{x}}_{n+1}) + \mathbf{h}_n + \mathbf{h}_{n+1}. \end{aligned} \tag{5.20}$$

Then, by using the following $\mathbf{B}_{\hat{k},K} \in \mathcal{C}^{K\times 4}$ matrix

$$\mathbf{B}_{\hat{k},K} = \begin{bmatrix} a_1 & b_1 & c_1 & d_1 \\ a_2 & b_2 & c_2 & d_2 \\ . & & & \\ a_K & b_K & c_K & d_K \end{bmatrix}, \tag{5.21}$$

the vector $\mathbf{x}_{\hat{k},K}(\gamma)$ can be expressed as a third order piece-wise continuous polynomial:

$$\mathbf{x}_{\hat{k},K}(\gamma) = \mathbf{B}_{\hat{k},K}\boldsymbol{\gamma}, \tag{5.22}$$

where $\boldsymbol{\gamma} = [1, \gamma, \gamma^2, \gamma^3]^T$. By substituting (5.22) into (5.15), the following cost function is obtained:

$$f_\gamma(\gamma) = -2\mathrm{Re}\{c(\gamma)\mathbf{y}_{k,K}^H \mathbf{B}_{\hat{k},K}\boldsymbol{\gamma}\} + |c(\gamma)|^2 \|\mathbf{B}_{\hat{k},K}\boldsymbol{\gamma}\|^2. \tag{5.23}$$

To find the local minimum of $f_\gamma(\gamma)$, the Newton-Raphson algorithm can be used [82]. In the required iterations, the first and second order derivatives of $f_\gamma(\gamma)$ are required. To compute these derivatives, let us rewrite $f_\gamma(\gamma)$ as

$$f_\gamma(\gamma) = -2\mathrm{Re}\left\{c(\gamma)p(\gamma)\right\} + g(\gamma)q(\gamma), \tag{5.24}$$

where $p(\gamma) = \mathbf{y}_{k,K}^H \mathbf{B}_{\hat{k},K}\boldsymbol{\gamma}$, $q(\gamma) = \boldsymbol{\gamma}^T \mathbf{B}_{\hat{k},K}^H \mathbf{B}_{\hat{k},K}\boldsymbol{\gamma}$ and $g(\gamma) = |c(\gamma)|^2$. Using these definitions, $f'_\gamma(\gamma)$ and $f''_\gamma(\gamma)$ are computed as:

$$\begin{aligned} f'_\gamma(\gamma) =& -2\mathrm{Re}\left\{c'(\gamma)p(\gamma) + c(\gamma)p'(\gamma)\right\} + g'(\gamma)q(\gamma) + g(\gamma)q'(\gamma), && (5.25)\\ f''_\gamma(\gamma) =& -2\mathrm{Re}\left\{c''(\gamma)p(\gamma) + 2c'(\gamma)p'(\gamma) + c(\gamma)p''(\gamma)\right\} \\ &+ g''(\gamma)q(\gamma) + 2g'(\gamma)q'(\gamma) + g(\gamma)q''(\gamma), && (5.26)\end{aligned}$$

where the following closed form expressions for the derivatives are used in the iterations:

$$\begin{aligned} p'(\gamma) &= \mathbf{y}_{k,K}^H \mathbf{B}_{\hat{k},K}\mathbf{D}\boldsymbol{\gamma}, && (5.27)\\ p''(\gamma) &= \mathbf{y}_{k,K}^H \mathbf{B}_{\hat{k},K}\mathbf{D}^2\boldsymbol{\gamma}, && (5.28)\\ q'(\gamma) &= \boldsymbol{\gamma}^T\left(\mathbf{D}^T\mathbf{B}_{\hat{k},K}^H\mathbf{B}_{\hat{k},K} + \mathbf{B}_{\hat{k},K}^H\mathbf{B}_{\hat{k},K}\mathbf{D}\right)\boldsymbol{\gamma}, && (5.29)\\ q''(\gamma) &= \boldsymbol{\gamma}^T\Big(\left(\mathbf{D}^T\right)^2\mathbf{B}_{\hat{k},K}^H\mathbf{B}_{\hat{k},K} + 2\mathbf{D}^T\mathbf{B}_{\hat{k},K}^H\mathbf{B}_{\hat{k},K}\mathbf{D} + \mathbf{B}_{\hat{k},K}^H\mathbf{B}_{\hat{k},K}\mathbf{D}^2\Big)\boldsymbol{\gamma}, && (5.30)\end{aligned}$$

where $\mathbf{D}$ is the matrix that obtains the derivative of vector $\boldsymbol{\gamma} = [1, \gamma, \gamma^2, \gamma^3]^T$. Using $p(\gamma)$ and $q(\gamma)$, $c(\gamma)$ can be written as $c(\gamma) = p^*(\gamma)/q(\gamma)$. Then, the first and second order derivatives of $c(\gamma)$ are obtained as:

$$c'(\gamma) = \frac{p'^*(\gamma)}{q(\gamma)} - \frac{q'(\gamma)p^*(\gamma)}{q(\gamma)^2}\ , \tag{5.31}$$

$$c''(\gamma) = \frac{p''^*(\gamma)}{q(\gamma)} - \frac{q'(\gamma)p'^*(\gamma)}{q(\gamma)^2} - \frac{q''(\gamma)p^*(\gamma) + p'^*(\gamma)q'(\gamma)}{q(\gamma)^2} + 2\frac{(q'(\gamma))^2p^*(\gamma)}{q(\gamma)^3}. \tag{5.32}$$

Finally, the derivatives of $g(\gamma)$ can be written in terms of $c(\gamma)$ and $c'(\gamma)$ as:

$$\begin{aligned} g'(\gamma) &= 2\mathrm{Re}\{c'(\gamma)c^*(\gamma)\} && (5.33)\\ g''(\gamma) &= 2\mathrm{Re}\{c''(\gamma)c^*(\gamma)\} + |c'(\gamma)|^2. && (5.34)\end{aligned}$$

The above expressions for the derivatives lead to accurate convergence in about 20 iterations.

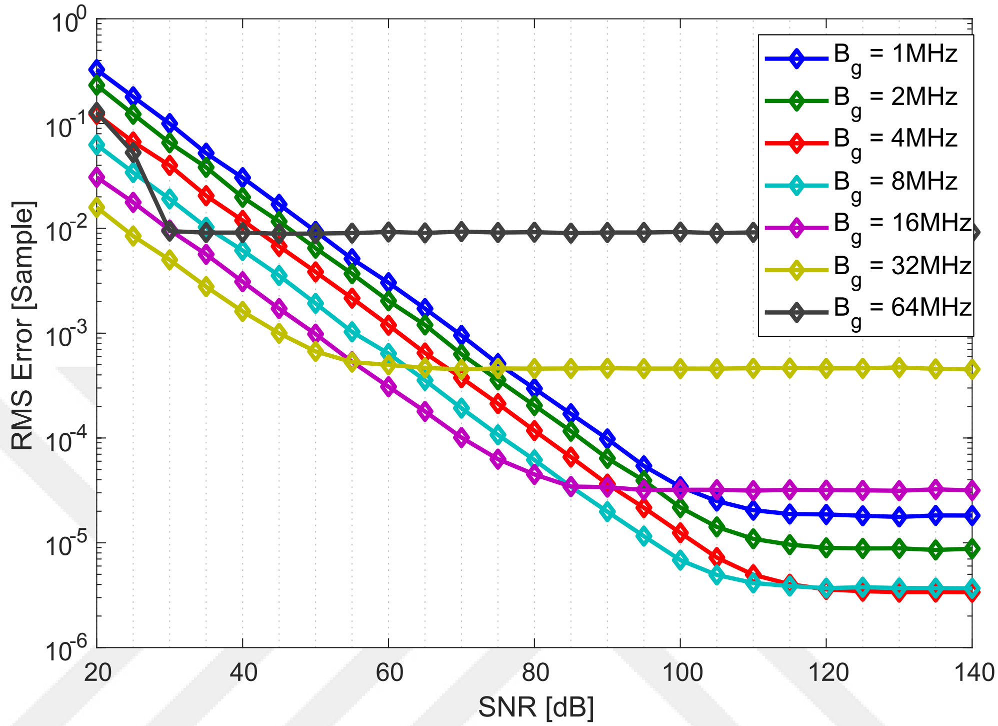

Figure 5.4: Standard deviation of the delay estimation error as a function of SNR, for different values of B_g.

Once $\hat{\gamma}$ and $\hat{\zeta}$ are obtained, τ is estimated as:

$$\hat{\tau} = (\hat{\gamma} + \hat{\zeta})/F_s, \tag{5.35}$$

where $\hat{\zeta}$ and $\hat{\gamma}$ are the minimizers of (5.12) and (5.23), respectively. The overall algorithm is summarized in Alg-1. Once the relative delays of all pulses with respect to the reference pulse are estimated, all the pulses are coherently integrated using (5.4). In the integration process, estimated delay values, which are at a higher resolution than the sampling interval, can be handled either by using the continuous function model given in (5.17) or by using fractional-delay filters [81]. In the next section, we present results obtained on both synthetic and real data sets.

5.3 Experimental Results on Pulse Alignment

To investigate the performance of the proposed delay estimation method, we performed experiments on the following synthetically generated radar pulses:

$$g(t) = Aa(t)e^{j\phi(t)}, \tag{5.36}$$

where A is the amplitude, $\phi(t)$ is the instantaneous phase, and $a(t)$ is the envelope of the pulse defined as:

$$a(t) = \begin{cases} e^{-t^2/\sigma_{TR}^2} & \text{if } t \leq 0, \\ 1 & \text{if } 0 < t \leq T_{PW}, \\ e^{(-t-T_{PW})^2/\sigma_{TF}^2} & \text{if } t > T_{PW}, \end{cases} \tag{5.37}$$

where the pulse width T_{PW} is chosen as 1 μs and both the pulse rise time σ_{TR} and pulse fall time σ_{TF} are chosen as 0.01 μs. Each pulse is modulated by using the following frequency modulation:

$$f_g(t) = 0.5B_g \cos(2\pi t/T_g), \tag{5.38}$$

where $B_g \in \{1, 2, 4, 8, 16, 32\}$ MHz and $T_g = 1$ μs are the FM deviation (bandwidth) and the FM rate of the modulation. The corresponding instantaneous phase of the pulse is:

$$\phi(t) = \int_{-\infty}^{t} f_g(\hat{t})d\hat{t} + \phi_0, \tag{5.39}$$

where ϕ_0 denotes the frequency offset of the pulse. The sampling frequency of the waveform is set to $F_s = 100$ MHz. Finally, circularly symmetric white Gaussian noise with appropriately chosen standard deviation σ_z is added to set the SNR to any desired value, given by SNR $= 20 \log 10(A/\sigma_z)$ dB. At each SNR and modulation bandwidth B_g, 10000 Monte-Carlo runs were performed. In each run, a delayed pulse $g(t - \tau/Fs)$ is generated where τ is chosen from a uniform random distribution in the interval $[-5, 5]$. Its phase offset ϕ_0 is chosen from a uniform random distribution in the interval $[-\pi, \pi)$. The standard deviation of the estimation error as a function of SNR and B_g is shown in Fig. 5.4. As

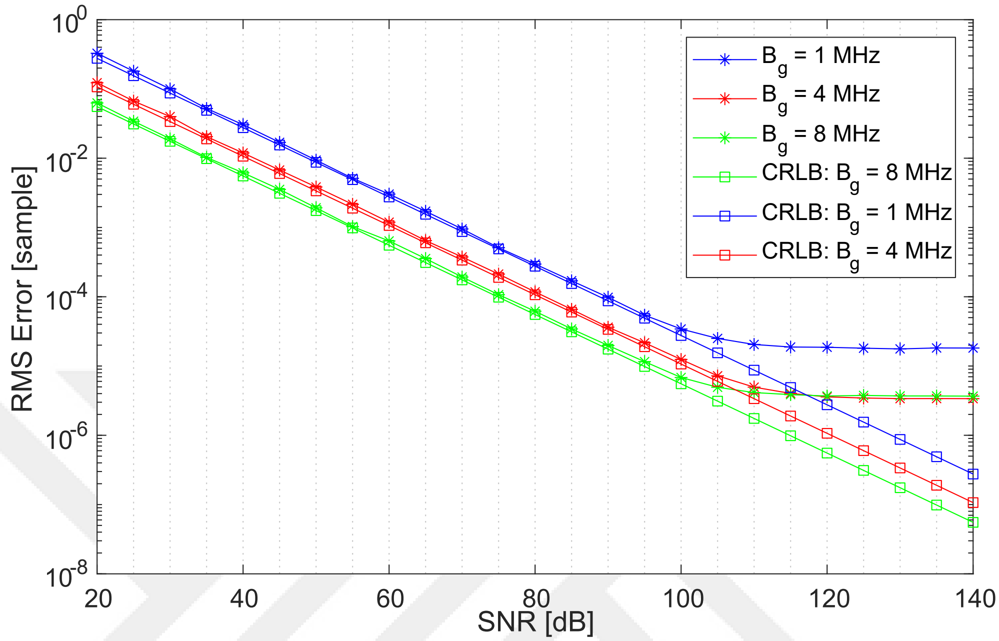

Figure 5.5: Standard deviation of the delay estimation error and CRLB as a function of SNR and bandwidth B_g.

observed, the proposed method performs better with increasing SNR and achieves a minimum estimation error of $10^{-5.4}$ samples at 105 dB. Beyond this point, there is no performance improvement, since the modeling error in representing the discrete measurements by cubic splines becomes dominant. Moreover, beyond a value of 16 MHz, performance of the proposed technique drops significantly. This observation can be explained as follows. As the BW increases, the non-regularity in the pulse increases, hence the algorithm performs better. However, at very high BW, the instantaneous frequency of the pulse gets closer to the Nyquist limit ($F_s/2$), and the cubic splines become insufficient in representing the available samples.

The performance of proposed pulse alignment technique can also be compared with the Cramer-Rao lower bound (CRLB) for the delay estimation. Time delay estimation between replicas of arbitrary waveform is a well known application of correlation processing [83] and CRLB can be calculated as [84]:

$$\sigma_\tau = \frac{1}{\beta}\frac{1}{\sqrt{BT\gamma}} \tag{5.40}$$

where B is the noise bandwidth at receiver input assumed to be the same for both replicas, T is the integration time, β is the rms radian frequency for the received signal power density spectrum $W_s(f)$ which can be calculated as:

$$\beta = 2\pi \left[\frac{\int_{-\infty}^{\infty} f^2 W_s(f) df}{\int_{-\infty}^{\infty} W_s(f) df} \right] \tag{5.41}$$

and γ is the effective input signal noise ratio for two pulses which can be given as:

$$\frac{1}{\gamma} = \frac{1}{2} \left[\frac{1}{\gamma_1} + \frac{1}{\gamma_2} + \frac{1}{\gamma_1 \gamma_2} \right] \tag{5.42}$$

where γ_1 and γ_2 denotes SNR's in the respective pulses.

Performance comparison between proposed pulse alignment technique and the CRLB for estimating the time delay between two measurements is shown in Fig. 5.5. This comparison shows that proposed pulse alignment technique reaches the performance bound determined by the CRLB. Also, another important observation is that increasing the BW of the pulse for a fixed FM rate improves the estimation performance, which is in agreement with the CRLB.

We also performed experiments on a real data set. The pulses shown in Fig. 5.2 are aligned by using the proposed technique and the results are shown in Fig. 5.3. As compared to Fig. 5.2, the instantaneous frequency curves of the aligned pulses are significantly closer to each other for every time instant. This effect is more evident when there exist some frequency modulations in the pulse.

To demonstrate the importance of pulse integration for precise SEI analysis, a third experiment is conducted, where the response of an amplifier, which is the basic transmitting element radars. We applied a 1 μs pulse at the input of the amplifier and collected 500 pulses from its output. The envelopes and instantaneous frequencies of the pulses are shown in Fig. 5.6. In each plot, the close-up inserts are also provided. First, available pulses are aligned by using the proposed method and then integrated using (5.4). The resulting integrated pulse is shown in Fig. 5.7. In the close-up insert region of the instantaneous frequency graph, there appears to be some unintentional frequency modulation with a bandwidth of a few kHz. Note that this modulation is not visible prior to pulse integration.

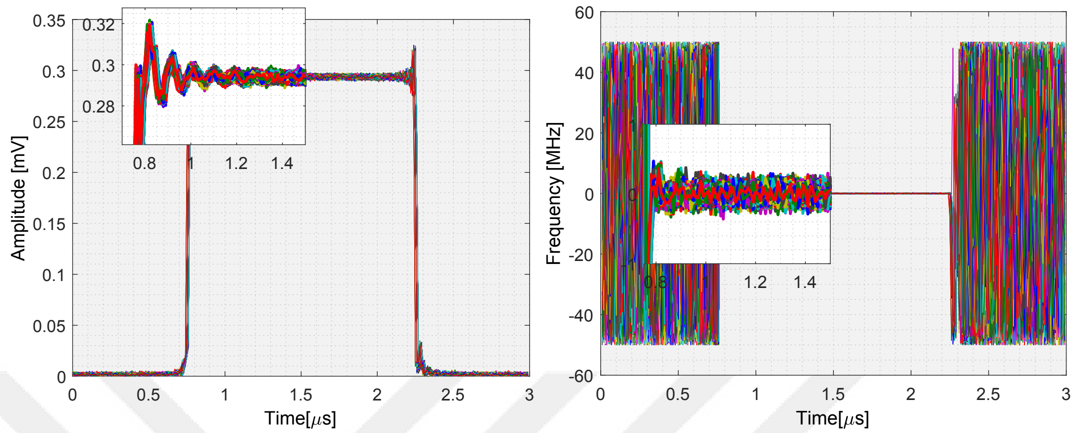

Figure 5.6: Envelopes (left) and instantaneous frequencies (right) of the pulses emitted by a T-module.

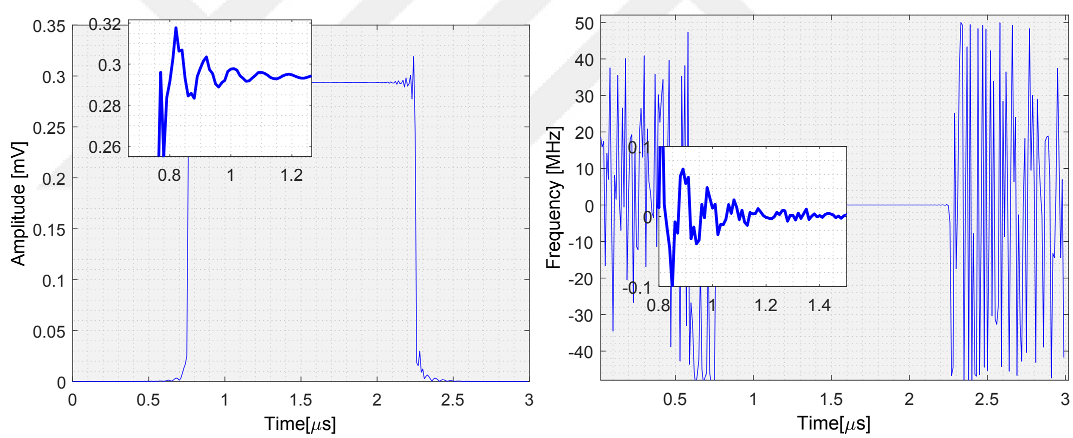

Figure 5.7: Envelope (left) and instantaneous frequency (right) of the pulse obtained by integrating all the pulses shown in Fig. 5.6.

5.4 Radar Fingerprint Extraction

In this section we will provide details for radar fingerprint extraction. To illustrate the result of each stage we will use real measurements of four solid state radar power amplifiers that are manufactured on the same production line. During the experiments, 500 pulses are obtained from each power amplifier, and input signals driving the amplifiers are set so that the outputs of the amplifiers are saturated. In Fig. 5.8, measurements obtained for two different amplifiers that will be referred to as Amp-1 and Amp-2 are shown. Comparing the experimental data we have obtained, unintentional modulations on real data can be observed

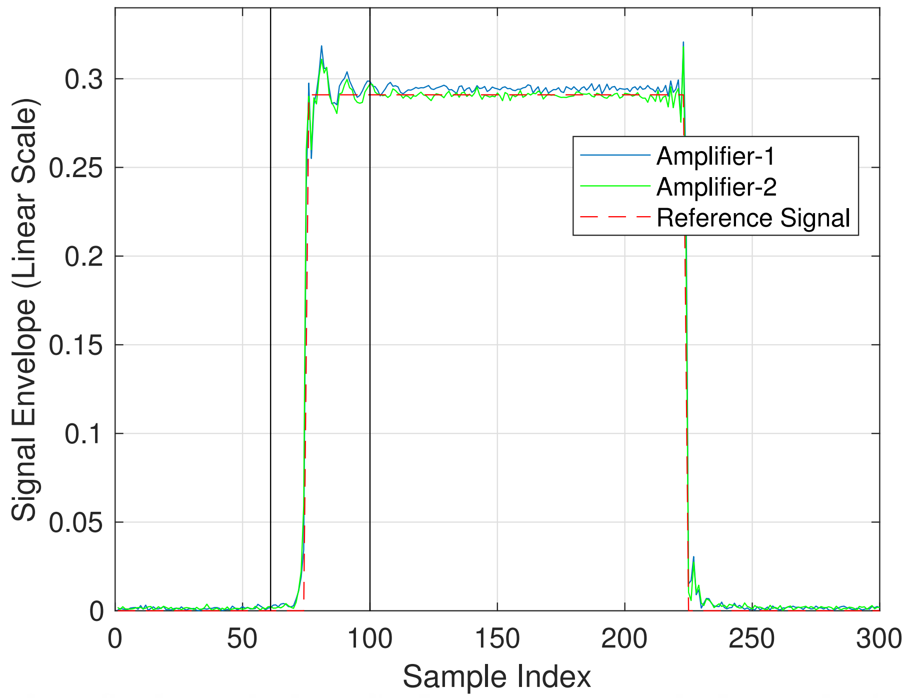

Figure 5.8: Blue: Amplifier-1 amplitude; Green: Amplifier-2 amplitude; Red: Reference ideal square wave signal that will be subtracted from the original signals; Black: Time window for UMOP.

at the on-set of each pulse. As a result, we used the time window with duration of 1 μs around the point where the pulse detection first occurs. Considering this fact, we take a closer look at the time window shown in Fig.5.8 after subtracting an ideal square wave that fits the measurement data. Residual signals are shown in Fig. 5.9 and Fig. 5.10, respectively.

In order to observe localized frequency characteristics of the residual signal $r[n]$, the Short Time Fourier Transform (STFT) can be used [85]:

$$R(m,w) = \sum_{n=-\infty}^{\infty} r[n]w[m-n]e^{-jwn} \tag{5.43}$$

where $R(m,w)$ is the STFT of $r[n]$ at time m and $w[n]$ is the window function. By using the Fast Fourier Transform (FFT), the discrete STFT can be computed at $w = \frac{2\pi}{N}k, 0 \leq k \leq N-1$.

In Fig. 5.9 and Fig. 5.10, the discrete STFTs of the residual signals are shown

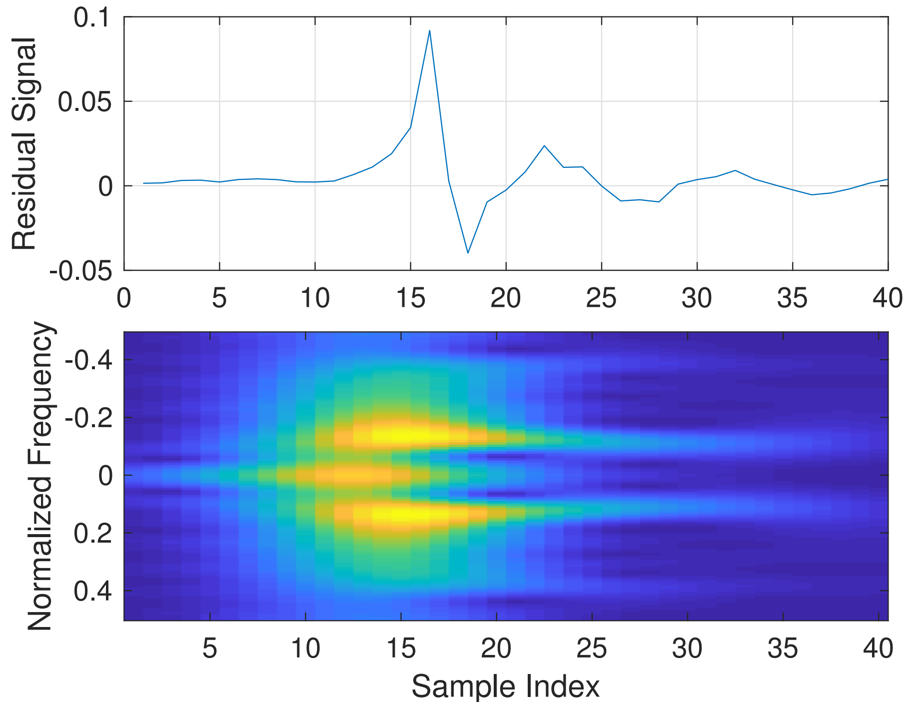

Figure 5.9: Residual Amp-1 signal after subtracting the square wave (top) and its STFT (bottom).

for a Gaussian window function with standard deviation of $\sigma = 5$. Although these two signals are very similar in the time domain, more prominent differences can be observed in their STFTs. Both signals have two significant components with different time-frequency supports. For example, in Fig. 5.9, the frequency support of each component is more compact compared to the frequency support of the corresponding components in Fig. 5.10. Also, the time differences between these components are not the same for Amp-1 and Amp-2. Therefore, features generated using these components with compact frequency and time support have the potential to serve as the fingerprint. This requires robust estimation of these components from the original signal.

For this purpose, the Variational Mode Decomposition (VMD) which as introduced in [80] can be used. In VMD, all modes are estimated concurrently by using the Alternating Direction Method of Multipliers (ADMM) optimization technique [86–88]. In the remainder of this section, we provide a brief review of

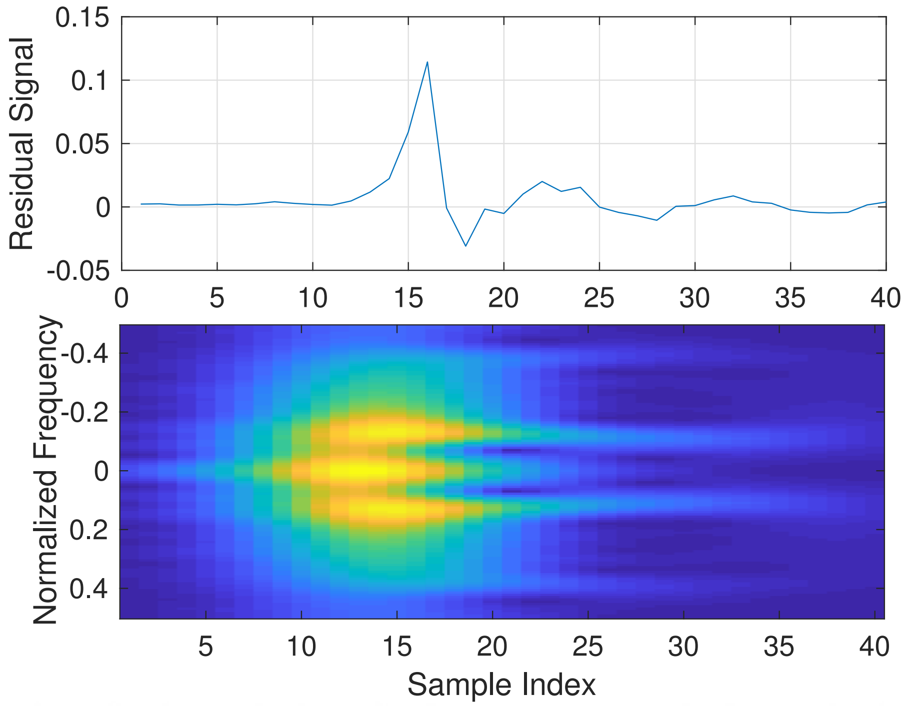

Figure 5.10: Residual Amp-2 signal after subtracting the square wave (top) and its STFT (bottom).

the VMD based on [80], and detail its use in fingerprint extraction.

The goal of VMD is to decompose a real valued input signal $x(t)$ into a number of modes, $u_k(t)$, that have a compact support around a center frequency w_k:

$$u_k(t) = A_k(t)\cos(\phi_k(t)), \tag{5.47}$$

where the modes $u_k(t)$ are identified as the solution to the following optimization problem:

$$\begin{aligned} &\min_{\{u_k(t)\},\{w_k\}} \left(\sum_k \left\| \partial_t \left[\left(\delta(t) + \frac{j}{\pi t} \right) * u_k(t) \right] e^{-jw_k t} \right\|_2^2 \right) \\ &\text{s.t.} \quad \sum_k u_k(t) = x(t) \ . \end{aligned} \tag{5.48}$$

Here, $\{u_k(t)\} := \{u_1(t), u_2(t), \ldots, u_k(t)\}$ and $\{w_k\} := \{w_1, w_2, \ldots, w_k\}$ denotes the center frequency of each mode.

In order to address the constraint of the optimization problem given in (5.48),

Algorithm 4 ADMM Optimization for VMD

Initialization: $\{\hat{u}_k^1\}, \{\hat{w}_k^1\}, \hat{\lambda}^1, n \leftarrow 0$

repeat

  $n \leftarrow n+1$

  for $k = 1 : K$ **do**

    Update mod signals:

$$\hat{u}_k^{n+1}(w) \leftarrow \frac{\hat{x}(w) - \sum_{i<k} \hat{u}_i^{n+1}(w) - \sum_{i>k} \hat{u}_i^n(w) + \frac{\hat{\lambda}}{2}}{1 + 2a(w - w_k)^2} \tag{5.44}$$

    Update mod frequencies:

$$w_k^{n+1} \leftarrow \frac{\int_0^\infty w |\hat{u}_k^{n+1}(w)|^2 dw}{\int_0^\infty |\hat{u}_k^{n+1}(w)|^2 dw} \tag{5.45}$$

  end for

  Dual Ascent for all $w \geq 0$:

$$\hat{\lambda}^{n+1}(w) \leftarrow \hat{\lambda}^n(w) + \tau \left(\hat{f}(w) - \sum_k \hat{u}_k^{n+1}(w) \right) \tag{5.46}$$

until convergence $\sum_k \|\hat{u}_k^{n+1} - \hat{u}_k^n\|_2^2 / \|\hat{u}_k^n\|_2^2 < \epsilon$

both the quadratic penalty term and the Lagrange multipliers are used by the VMD. The quadratic penalty term is used to boost the fidelity of the decomposition in the presence of noise while the Lagrange multipliers forces the constraint to be met. The augmented Lagrangian can be written as:

$$\mathcal{L}\left(\{u_k\}, \{w_k\}, \lambda\right) := \alpha \sum_k \left\| \partial_t \left[\left(\delta(t) + \frac{j}{\pi t} \right) * u_k(t) \right] e^{-jw_k t} \right\|_2^2 + \left\| f(t) - \sum_k u_k(t) \right\|_2^2 + \left\langle \lambda(t),\ f(t) - \sum_k u_k(t) \right\rangle . \tag{5.49}$$

The solution of the optimization problem given in (5.49) can be found as a saddle point of the augmented Lagrangian $\mathcal{L}$ in a sequence of iterative sub-optimizations by using the ADMM technique [80][1]. Steps of the algorithm is given in Algorithm 4.

[1]Detailed derivations are included in Appendix C.

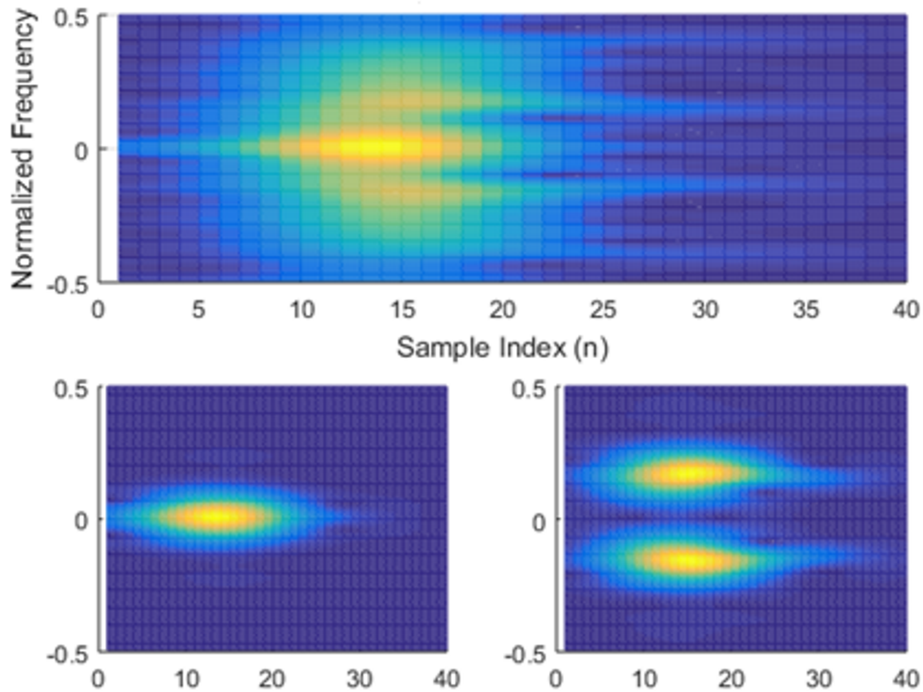

Figure 5.11: Amp-2 signal after decomposing into mods using VMD.

There are two important points that should be emphasized for VMD. In (5.44), similar to the expectation maximization approach, the k^{th} mod signal is updated by Wiener filtering the residual signal that is obtained after removing the latest updated versions of the remaining mod signals. This filtering operation denoise the signal, and help us improve the SNR. Secondly, in (5.45), w_k is chosen as the center of gravity of the power spectrum of the k^{th} mode.

The VMD technique can be used for the decomposition of UMOP signals into mods with compact frequency supports prior to feature extraction. An example of decomposed signals following the VMD is shown in Fig. 5.11. In order to characterize these mod signals, distribution of their energy in both time and frequency domains can be used. For example, the center of gravity of the mod signal in the time domain can be used to characterize the position of the mod signal, whereas in the frequency domain, the same approach would yield the estimate of its center frequency. This idea can be extended to generate the

Table 5.1: Features calculated for each mod signal.

Feature	**Time Domain Features**	**Frequency Domain Features**
Mean	$\mu_k^t = \frac{\int_{-\infty}^{\infty} t\|u_k(t)\|^2 dt}{\int_{-\infty}^{\infty} \|u_k(t)\|^2 dt}$	$\mu_k^w = \frac{\int_0^{\infty} w\|\hat{u}_k(w)\|^2 dw}{\int_0^{\infty} \|\hat{u}_k(w)\|^2 dw}$
Standard Deviation	$\sigma_k^t = \left(\frac{\int_{-\infty}^{\infty} (t-\mu_k^t)^2\|u_k(t)\|^2 dt}{\int_{-\infty}^{\infty} \|u_k(t)\|^2 dt}\right)^{\frac{1}{2}}$	$\sigma_k^w = \left(\frac{\int_0^{\infty} (w-\mu_k^w)^2\|\hat{u}_k(w)\|^2 dw}{\int_0^{\infty} \|\hat{u}_k(w)\|^2 dw}\right)^{\frac{1}{2}}$
Differential Entropy	$h_k^t = \frac{\int_{-\infty}^{\infty} \|u_k(t)\|^2 \log(1/\|u_k(t)\|^2) dt}{\int_{-\infty}^{\infty} \|u_k(t)\|^2 dw}$	$h_k^w = \frac{\int_{-\infty}^{\infty} \|\hat{u}_k(w)\|^2 \log(1/\|\hat{u}_k(w)\|^2) dw}{\int_{-\infty}^{\infty} \|\hat{u}_k(w)\|^2 dw}$
Kurtosis	$\kappa_k^t = \frac{\int_{-\infty}^{\infty} (t-\mu_k^t)^4/(\sigma_k^t)^4 \|u_k(t)^2\| dt}{\int_{-\infty}^{\infty} \|u_k(t)\|^2 dt}$	$\kappa_k^w = \frac{\int_{-\infty}^{\infty} (w-\mu_k^w)^4/(\sigma_k^w)^4 \|\hat{u}_k(w)^2\| dw}{\int_{-\infty}^{\infty} \|\hat{u}_k(w)\|^2 dw}$
Skewness	$s_k^t = \frac{\int_{-\infty}^{\infty} (t-\mu_k^t)^3/(\sigma_k^t)^3 \|u_k(t)^2\| dt}{\int_{-\infty}^{\infty} \|u_k(t)\|^2 dt}$	$s_k^w = \frac{\int_{-\infty}^{\infty} (w-\mu_k^w)^3/(\sigma_k^w)^3 \|\hat{u}_k(w)^2\| dw}{\int_{-\infty}^{\infty} \|\hat{u}_k(w)\|^2 dw}$

features given in Table. 5.1, which are obtained by normalizing the energy of the mod signals and considering them as probability density functions (PDF).

Note that, all features except the time center of the mods are time invariant, i.e., extracted features are not affected by the time shift of the signal in the acquisition window. This is actually a desired property that improves the robustness of the feature extraction method, as the position of the pulse rise time in the data acquisition window might change slightly between different measurements. By using the mean time of the first mod signal as a reference, this feature can also be transformed to a time invariant feature as:

$$\mu_k^{t_{ref}} = \mu_k^t - \mu_0^t \ , \tag{5.50}$$

where μ_0^t is the mean time of the first mod signal.

5.5 Computational Complexity Analysis

In this section, the computational complexity of the proposed method will be analysed. It will be assumed that N pulses each having K samples are available. In the coarse alignment step, $\mathcal{O}(K)$ operations are performed for evaluating (5.12), hence $\kappa \times \mathcal{O}(K)$ operations are required for finding the coarse delay estimate ζ. In the fine alignment step, the main complexity arises from solving the linear system of equations given in (5.18) and the derivatives defined from (5.27) to (5.30). Since $\mathbf{A}$ in (5.18) is tri-diagonal, it can be solved in $\mathcal{O}(K+1)$ operations using the Thomas Algorithm [82]. The consecutive derivatives of $p(\gamma)$ and $q(\gamma)$ can also be evaluated with $\mathcal{O}(K)$ operations. Hence, for N pulses, the total complexity of the alignment procedure requires $\mathcal{O}(K \times N)$ operations.

In the VMD stage, $\mathcal{O}(K)$ operations are required in (5.44) and (5.45) in Algorithm 4. If M mods are extracted (in our case $M = 2$) and T iterations are utilized (T is typically around 50 in our experiments), the total number operations required in the VMD stage is $\mathcal{O}(K \times M \times T)$. Note that, since this stage is utilized for the integrated pulse, the complexity of this stage is independent of the number of pulses. In the feature extraction step, all the features are computed at $\mathcal{O}(K)$ operations.

Overall, the main computational burden of the proposed method arises from the pulse alignment procedure, which is linear in the number of samples K and the number of pulses N.

5.6 Results on Real Field Data

To demonstrate the performance of the proposed SEI technique, three different data sets that consist of real measurements are used. During the experiments, the signals are decomposed into two components by VMD. The first set of measurements were obtained from the same solid state amplifiers whose data were analyzed in the previous section. The amplifiers were in the saturation regime

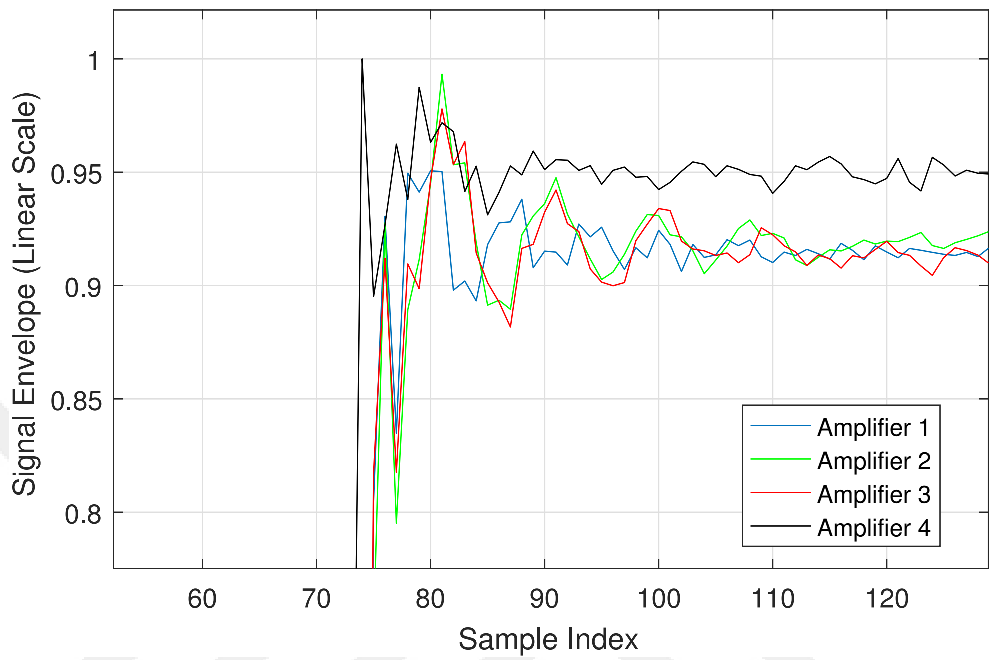

Figure 5.12: Signal envelopes for 4 different amplifiers.

and the data is obtained in a high SNR (SNR $\geq$ 50 dB) regime. For illustrative purposes, a set of measurements is shown in Fig. 5.12. The part of the signal where UMOP occurs is extracted by using the same time window shown in Fig. 5.8. Then, extracted signal is fed into the VMD feature extraction stage where the features given in Table.5.1 are obtained. Features obtained from the envelope of the radar signals are shown in Fig. 5.13, Fig. 5.14, and Fig. 5.15. As stated in [62], features should form natural clusters in the feature space for reliable classification. From the results we conclude that different emitters occupy separate regions of the feature space, and the amplifiers can be classified accurately by using a basic linear classifier.

In the second dataset, measurements obtained from an ELINT system operating in the field were used. The data set consist of 47 emitters. Some of these emitters were productions of the same radar. For each radar, we randomly generated 10 measurement sets of recorded pulses, where each set contains 200 pulses to be aligned and integrated. As a result, $47 \times 10 = 470$ different measurement sets are obtained. The Normalized Euclidean Distance of the extracted features between each measurement is plotted in Fig. 5.16 on a logarithmic scale. In this

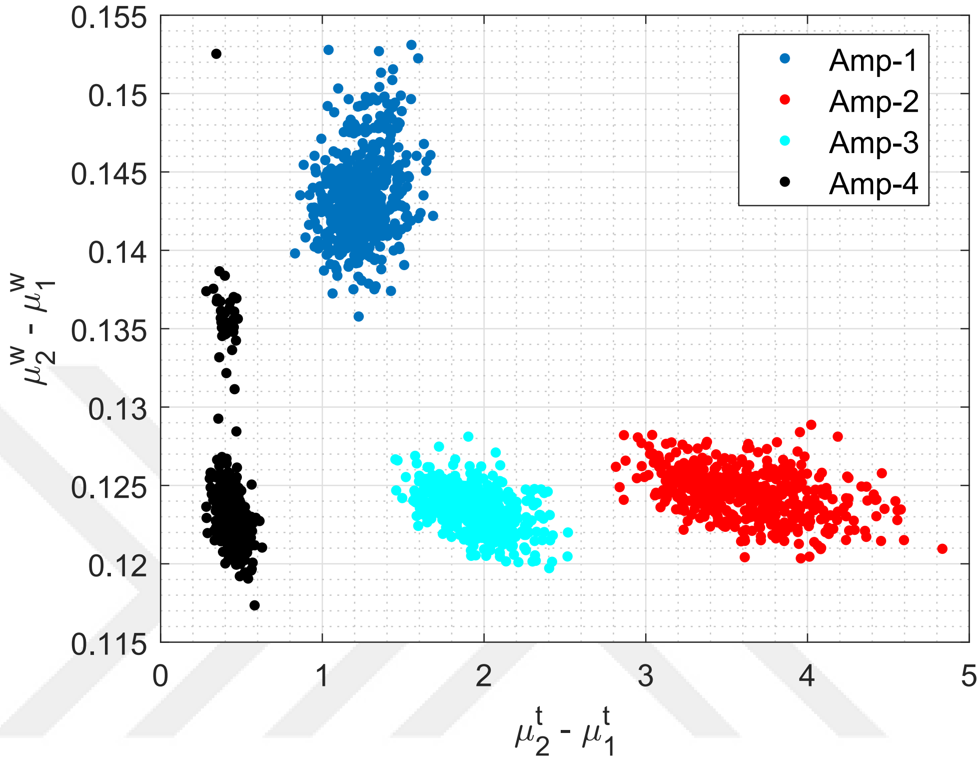

Figure 5.13: Time and frequency center features.

figure, every 10 by 10 sub-matrix around the diagonal belongs to the same class. It can be observed that in class distances are below -50 dB whereas distance between classes are above -20 dB.

The classification performance of the proposed features is evaluated using a simple majority voting classifier [89], since we are mainly interested in the quality of the generated features. During the classification process, the class index whose corresponding feature has the closest distance is found from the database for each computed feature. Once this operation is utilized for all extracted features, the most frequently appearing class index is selected as the classification result. The second and third possible candidate classes are obtained similarly. Although prior information of radars that can be obtained from classical parameters such as PW, PRI and RF can be used by practical SEI systems, these parameters are not used by the classifier during this experiment. During the experiments, it is only assumed that the test data of the classifier belongs to one of the emitters in the database, i.e. it is not a new emitter.

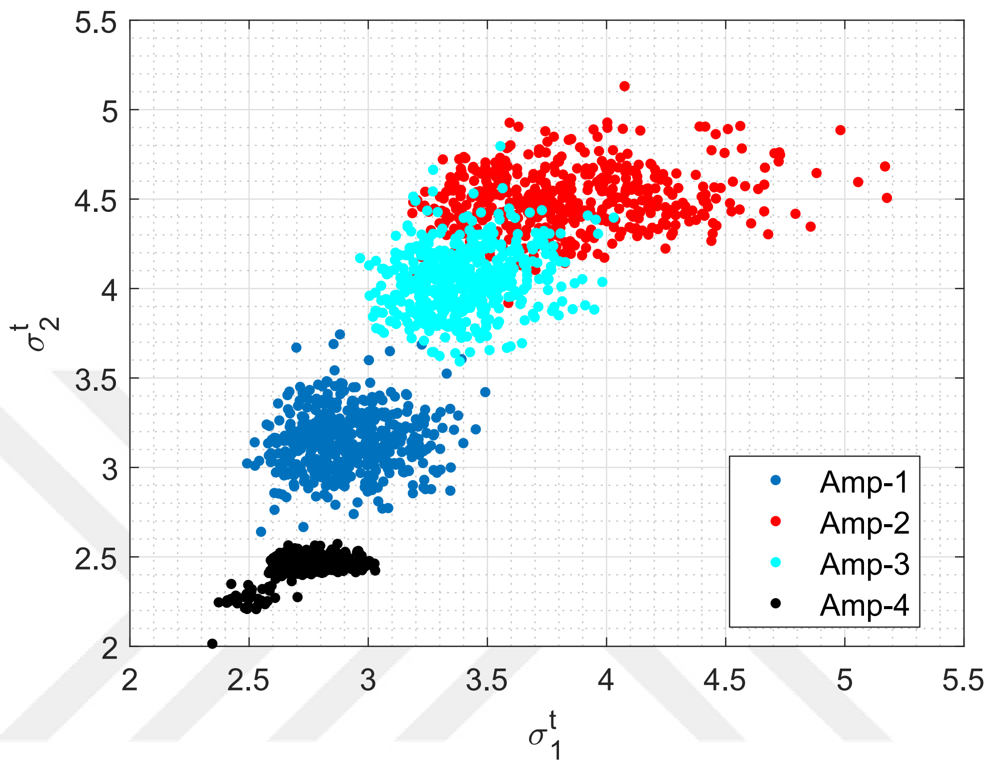

Figure 5.14: Time standard deviation feature.

During the classification experiments, we randomly generate 4 batches where each batch contains 400 pulses from 47 radars. As this dataset includes measurements of the same emitter that are obtained at different times over several years, we make sure that each batch consists of measurements that are taken at the same time. For each batch, we coherently integrate the pulses to obtain a high SNR measurement. One of these four signals for each radar is placed in a database as prior information and 3 other pulses are used for testing purposes. We therefore performed $47 \times 3 = 141$ classification tests. Obtained classification results are shown in Fig. 5.17. Our results show that the proposed technique can obtain 100% accuracy in this dataset.

Finally, we evaluate the performance of the SEI algorithm for different SNR levels and compare it with the EM^2 technique given in [72]. This analysis has a few very important aspects. First of all, it provides an opportunity to fairly compare our technique with the available methods in the literature using our real radar dataset. Another important points is that it enables us to determine the

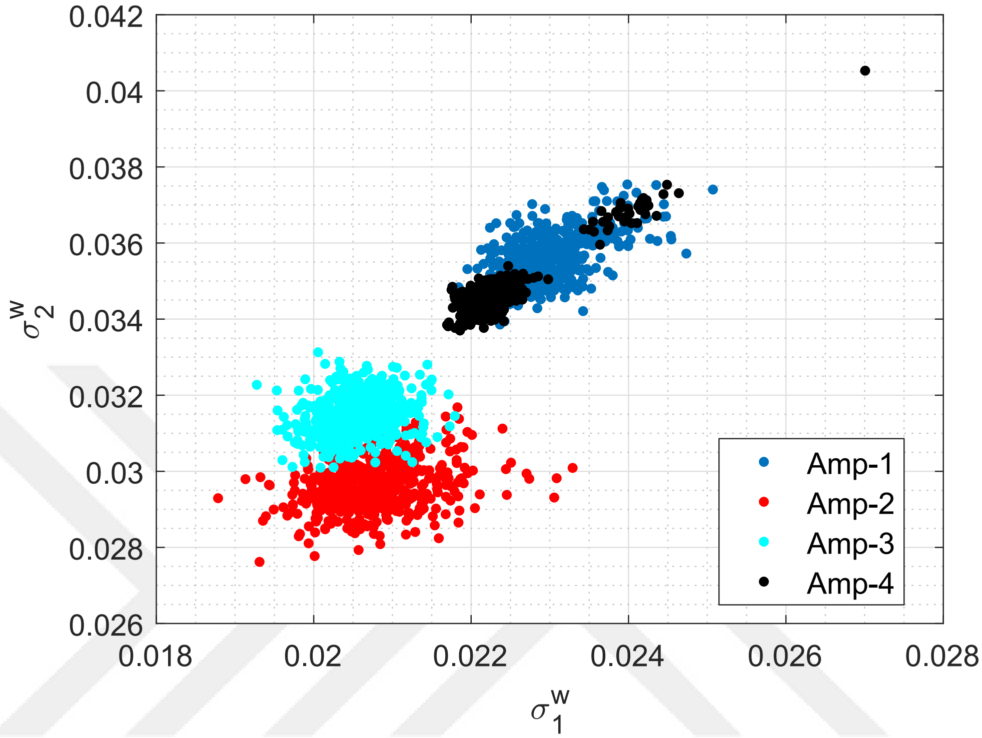

Figure 5.15: Frequency standard deviation feature.

number of pulses to be integrated that is required for successful SEI classification. Moreover, important system level requirements, such as antenna gain, can be derived so that the designed SEI system can capture the data at a sufficiently high SNR for SEI purposes. Unfortunately, obtaining the classification performance at different SNR levels using real radar data is not straight forward, due to the fact that data acquisition over multiple radars is a long term process, during which we have no direct control over the SNR of the received signal. But using our pulse alignment technique, we can generate measurements at a very high SNR (ideally at infinite SNR), and we can then obtain the SNR performance of our SEI technique by adding AWGN synthetically to test the performance at a desired SNR. To accomplish this task, we filtered the data so that each individual pulse had at least 30 dB SNR. During the SNR calculation, the pulse amplitude is calculated at the center of the pulse, so that the rise and fall times of the pulses which include some transient effects can be avoided. Assuming that we can perfectly align and integrate pulses, the effective SNR for N pulses can be calculated in dB as:

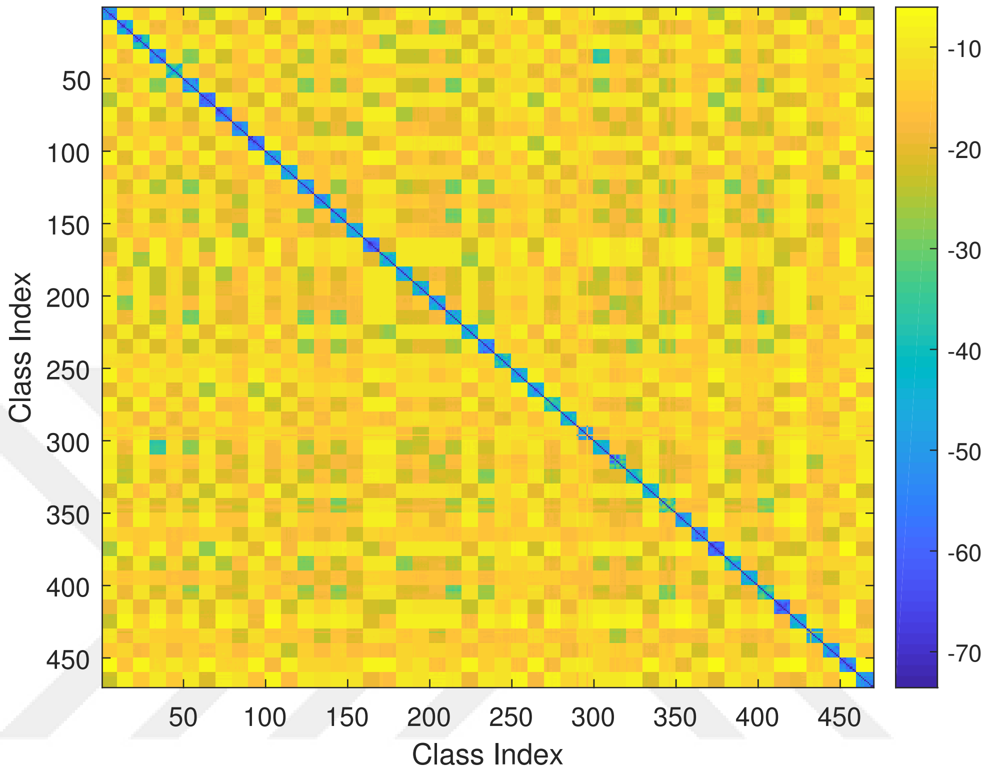

Figure 5.16: Normalized Euclidean Distance of features.

$$\mathrm{SNR}_{\mathrm{min}} = 30 + 10 \log_{10} N. \tag{5.51}$$

In Fig. 5.18, the number of pulses for each radar and the corresponding effective SNR bounds are shown. Note that this bound shows the minimum SNR level, assuming that the SNR of each pulse is at least 30 dB. As there are pulses with higher SNR, effective SNR for each radar is actually greater than the given bound. Also note that, the SNR calculation is conducted at the center of the pulse where no transient effects are present. As a result, the proposed SEI technique is actually working with samples that have much lower SNR which is different for each radar depending on their individual waveforms.

In Fig. 5.19, the overall classification performance that is obtained by using Monte Carlo simulations for SNR values between 30 to 60 dB is shown. Our results demonstrate that the effective SNR value should be around 47 dB to obtain a correct classification probability larger then 0.9. The performance of the

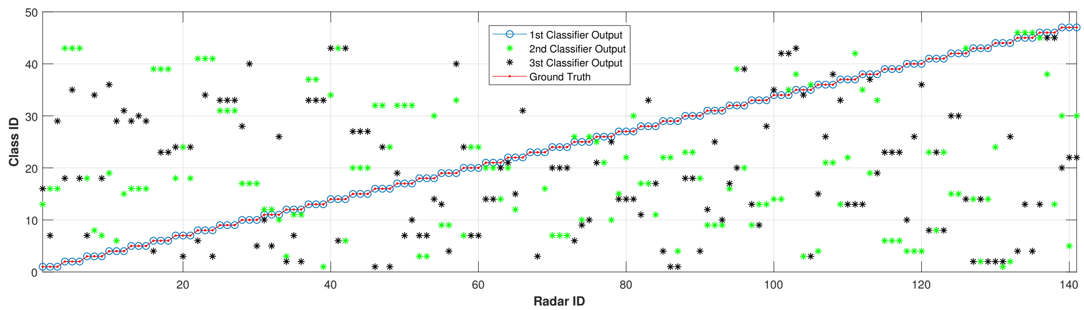

Figure 5.17: Classification performance for 47 different radar emitters.

proposed technique is also compared with the EM^2 method given in [72]. It can be observed that proposed technique outperforms EM^2 and has an SNR advantage of 4 dB for a 0.9 probability of correct classification. Furthermore, considering that EW systems typically observe their targets at a SNR of around 30 dB, we can conclude that we should integrate at least 100 pulses to achieve this level of performance. In Fig. 5.20, the SNR performance of each radar in the dataset is shown. It can be observed that classification performance is highly dependent on the radar type. For example, radar index 22 is easily distinguished from other emitters, whereas radar index 49 has a slightly lower classification performance compared to other radars. In Fig. 5.21, and Fig. 5.22, the envelopes of radar number 22 and 49 are given respectively. We can see that UMOP on radar 22 is very distinct, whereas the envelope of radar 49 is almost identical to an ideal square wave which is the main reason for the performance difference between these two emitters.

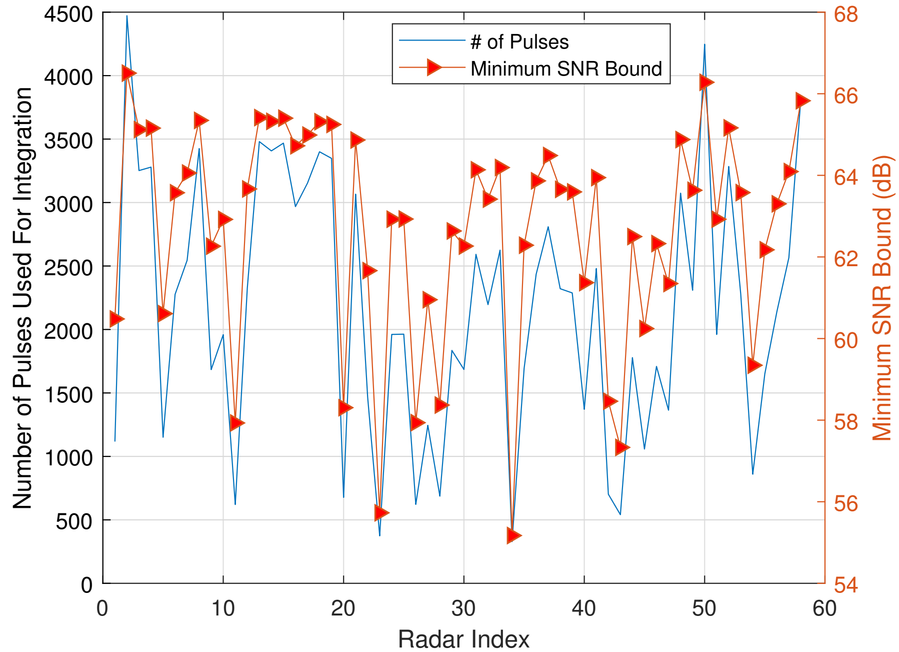

Figure 5.18: Number of pulses used during data integration for each radar, and the corresponding SNR lower bound.

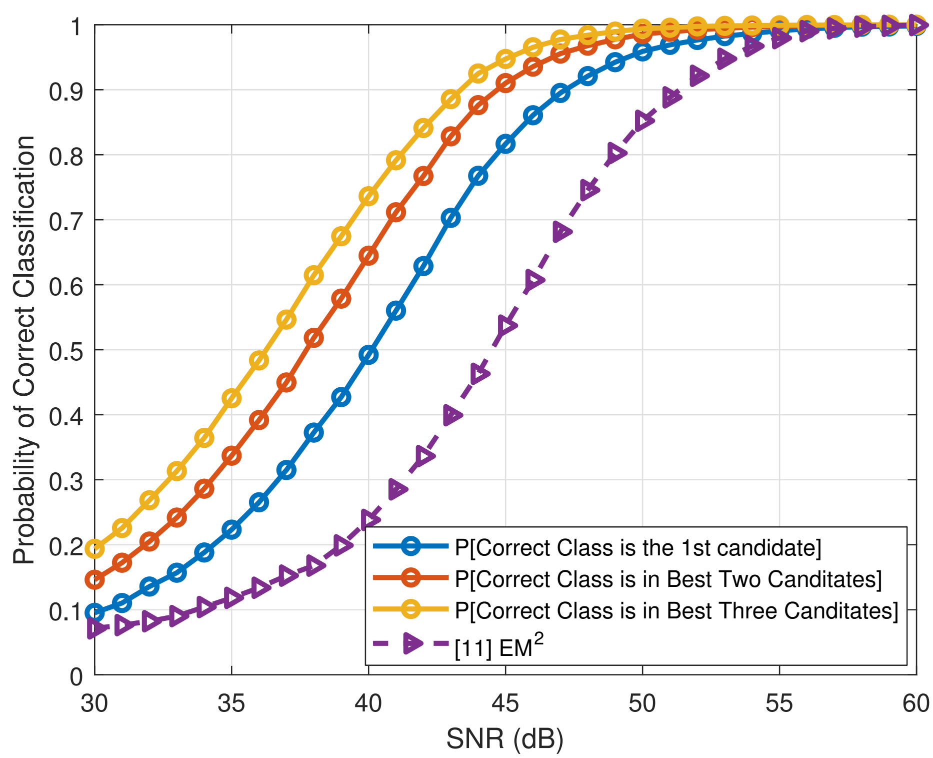

Figure 5.19: Classification performance with respect to SNR.

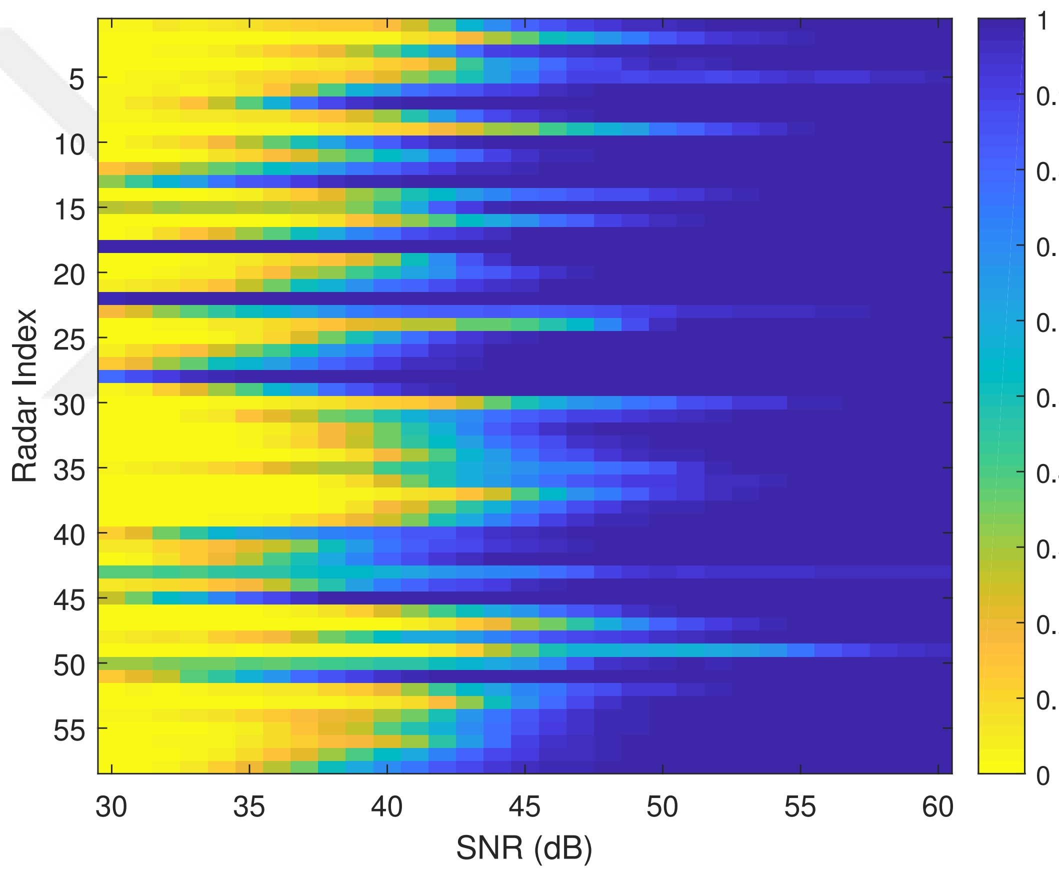

Figure 5.20: Probability of correct classification of the proposed technique for each radar with respect to SNR.

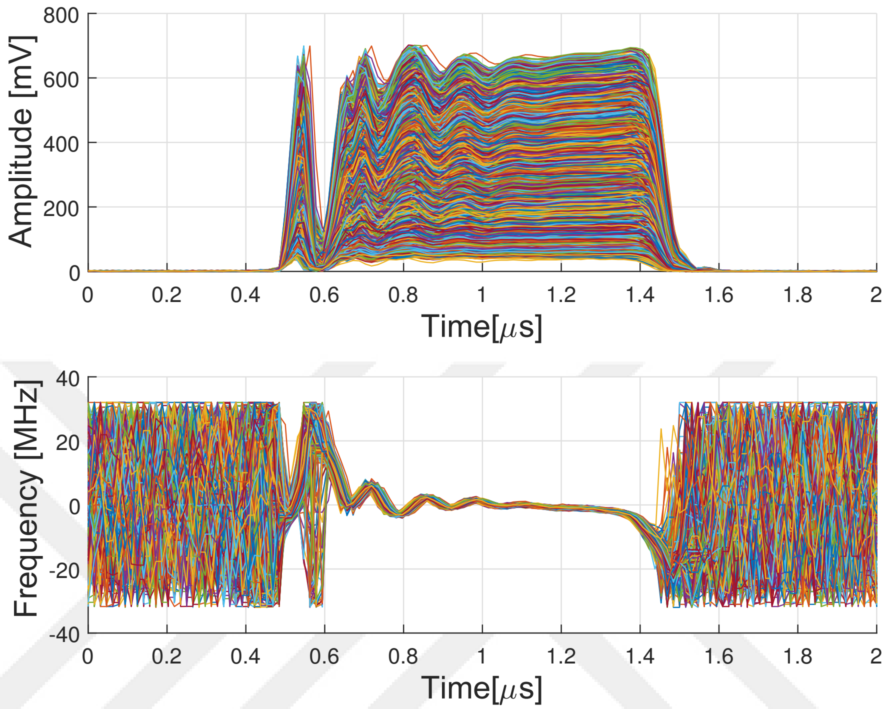

Figure 5.21: Complex samples of radar index 22. (Amplitude on the top, instantaneous frequency on the bottom.)

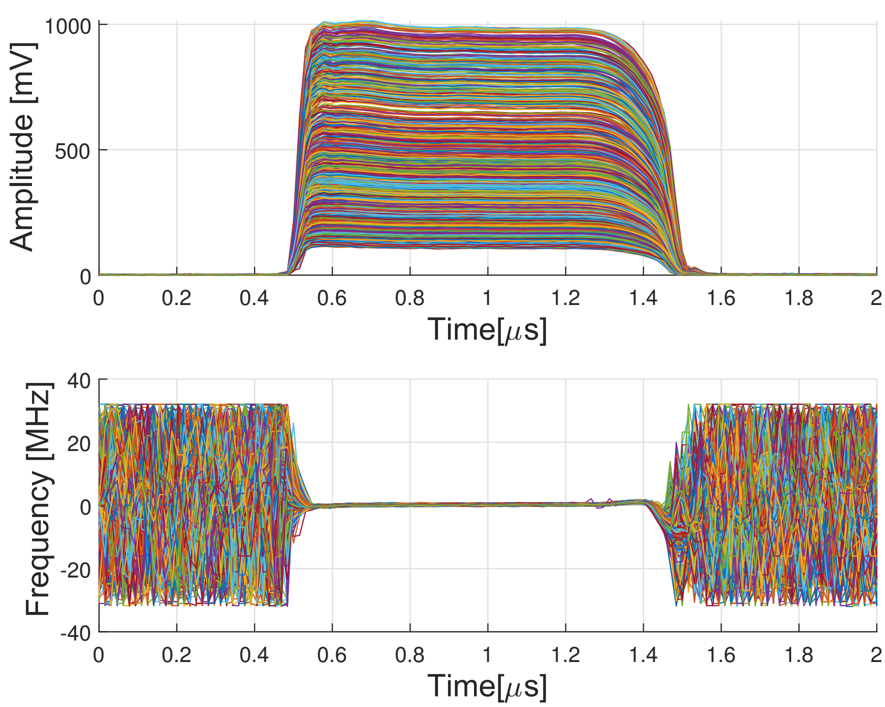

Figure 5.22: Complex samples of radar index 49. (Amplitude on the top, instantaneous frequency on the bottom.)

5.7 Effects of Local Oscillator Phase Noise on SEI Performance

As discussed in Sec.4.1.1, super hetorodyne receivers uses a local oscillator (LO) signal for translating the received signal to a IF frequency that is adequate for the ADC sampling. Hence, the local oscillator that is used for conversion should have low phase noise for minimal distortion on the received signal.

Although, the oscillator phase noise is extensively studied for satellite repeaters, sensitive communication receivers and mobile phone base stations, SEI literature does not include any analysis about the effect of phase noise on the performance of SEI systems. Typically, different sources state that phase noise of the local oscillators should be as low as possible for minimal coloring on the received signal [62] so that receiver characteristics does not change the results of the SEI algorithms. However, no numerical results for phase noise specifications are given for SEI receivers. Hence, in this section of the thesis we investigate the effects of phase noise on the SEI performance for the proposed technique.

Outline of this section is as follows. In Sec.5.7.1, definitions related to the phase noise are given. In Sec.5.7.2, a model for introducing phase noise to a baseband signal is introduced. In Sec.5.7.3, simulation results related to the effect of phase noise is discussed.

5.7.1 Definition of Phase Noise

Phase noise is defined as the noise arising from the short term phase fluctuations occur on a signal. Let $f_{LO}(t)$ denote oscillator signal which can be given as:

$$f_{LO}(t) = \cos(w_0 t + \phi(t)) \tag{5.52}$$

where w_0 is the frequency of the oscillator and $\phi(t)$ is the phase noise. In ideal conditions, $\phi(t) = 0\ \forall t$ should be satisfied and the spectrum of oscillator signals should have impulse at the locked frequency w_0. However, in practice, the phase

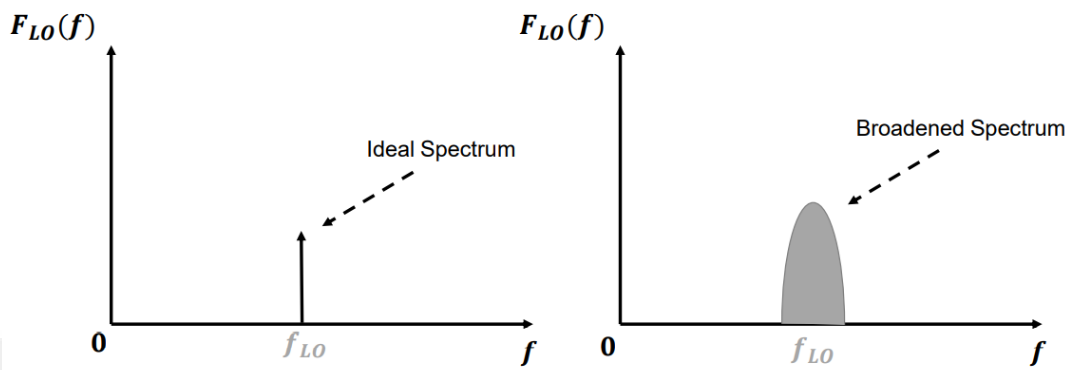

Figure 5.23: Effect of phase noise on the spectrum on the LO signal. (Ideal LO spectrum on the left, LO spectrum with phase noise on the right.)

of the oscillator signal has small fluctuations and these fluctuations appear as side-bands in the spectrum of the LO signal. This causes broadening of the signal spectrum as illustrated in Fig.5.23. This broadening effect causes defocusing on the received signal while translating it to the IF frequency.

Traditionally, the phase noise processes are illustrated in power spectral density (PSD) plots in the frequency domain [90]. Hence, while specifying phase noise of a LO, three elements need to be defined as shown in Fig.5.24. These three elements can be summarized as:

- **Phase Noise Amplitude:** It is expressed in dB relative to the carrier. This is normally denoted in **dBc**, e.g. -75 dBc means -75 decibels down in level from the carrier.
- **The offset from the carrier:** Showing the frequency difference between the carrier frequency and the frequency where the phase noise is measured, e.g 1 kHz.
- **Measurement Bandwidth:** Noise power is proportional to the band-width. Hence, measurement bandwidth should be specified along with the phase noise amplitude. Typically, 1 Hz is taken.

Using these three parameters, oscillator manufacturers specify the phase noise

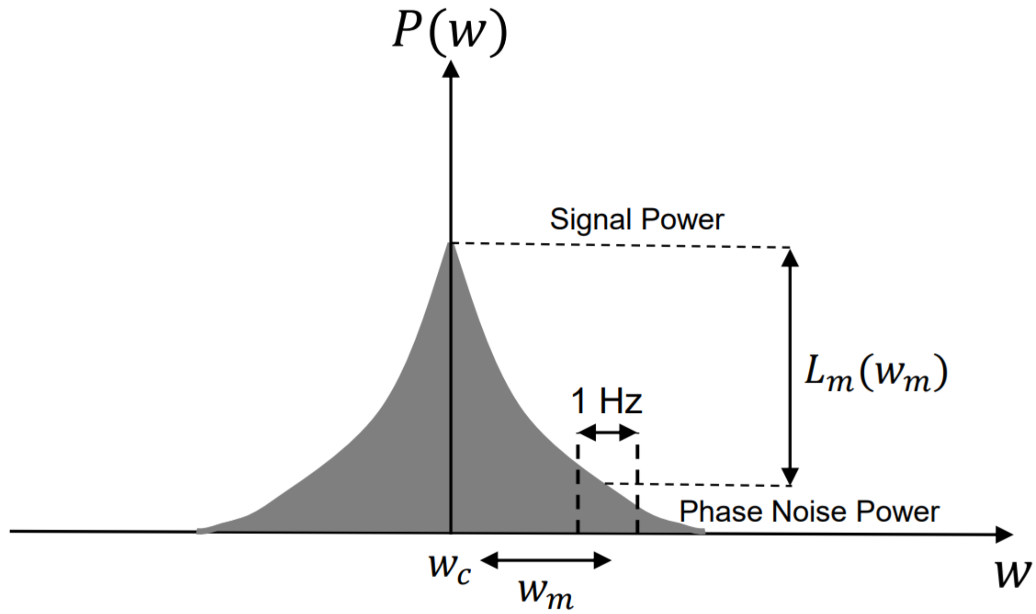

Figure 5.24: Phase noise specification using the power spectral density at the output of the LO.

of the oscillators using the unit of $[dBc/Hz]$ which is defined as:

$$L_m(w_m) = 10 \log \left(\frac{P_{noise}(w_m)}{P_{sig}} \right), \quad [dBc/Hz] \tag{5.53}$$

5.7.2 Introducing Phase Noise to a Baseband Signal

Noisy oscillator can be described in the time domain as:

$$f_{LO}(t) = (1 + \epsilon(t)) \cos(w_0 t + \phi(t)) \tag{5.54}$$

where $\epsilon(t)$ and $\phi(t)$ are real random processes modeling amplitude fluctuations and phase noise of the oscillator. To isolate the effect of phase noise on the oscillator PSD, it is assumed that amplitude fluctuations expressed through $\epsilon(t)$ have a negligible effect [91]. This assumption is also supported by the results of [92] where it is shown that there exists a frequency range close to the oscillator frequency w_0, effect of amplitude fluctuations on PSD is negligible compared to the phase noise.

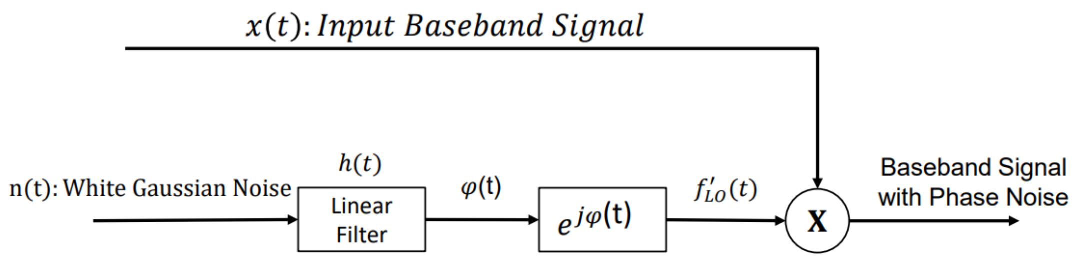

Figure 5.25: Adding phase noise to a baseband signal.

To simplify the analysis, consider the complex valued oscillation:

$$f'_{LO}(t) = e^{(jw_0 t + \phi(t))} \tag{5.55}$$

where $f'_{LO}(t)$ is the analytical LO signal. PSD of $f'_{LO}(t)$ has two main components. First components is due to the ideal LO signal $e^{jw_0 t}$ and its power spectrum includes a delta function at frequency w_0. Second component is due to $\phi(t)$ which is the phase noise component and it widens the PSD of the LO signal around frequency w_o. As the total PSD of the LO signal can be derived by frequency translation of $e^{j\phi(t)}$ with w_0, we will be only interested in the PSD of the $w(t)$ given as:

$$w(t) = e^{j\phi(t)} \quad . \tag{5.56}$$

It is common in the literature to assume that ϕ_t is a zero-mean wide sense stationary (WSS) process and more importantly ϕ_t is small enough to make the small-angle approximation so that $w(t)$ can written as [93]:

$$w(t) = e^{j\phi(t)} \approx 1 + j\phi(t) \tag{5.57}$$

With this approximation, autocorrelation of $w(t)$ can be calculated as:

$$\begin{aligned} R_{ww}(\tau) &= E\left[w(t)w(t-\tau)^*\right] \\ &\approx E\left[(1 - j\phi(t))(1 + j\phi(t-\tau))\right] \\ &= 1 + R_{\phi\phi}(\tau) \end{aligned} \tag{5.58}$$

where $E[.]$ is the expected value operator, '$*$' denotes the complex conjugate and $R_{\phi\phi} = E\left[\phi(t)\phi(t-\tau)\right]$. As as result, PSD of phase noise can be obtained as:

$$S_w(w) = \mathcal{F}\left\{R_{ww}(\tau)\right\} = 2\pi\delta(w) + S_\phi(w) \ , \tag{5.59}$$

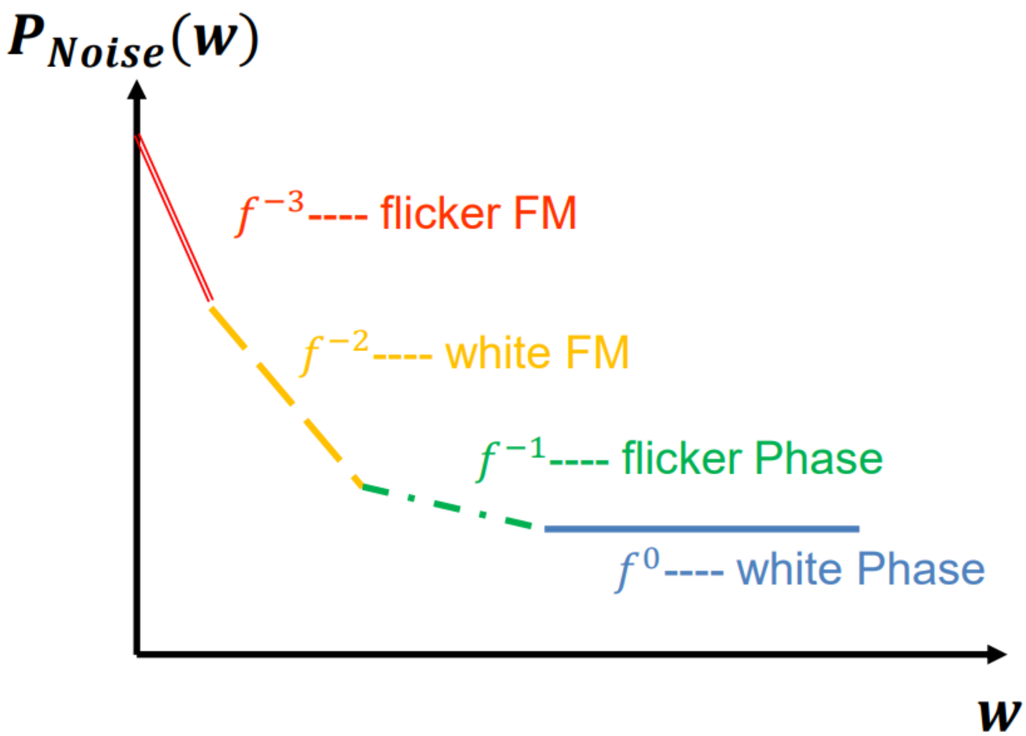

Figure 5.26: Power spectral density model for phase noise as a function of frequency.

where $S_{\phi}(w) = \mathcal{F}\{R_{\phi\phi}(\tau)\}$ denotes the PSD of the random process $\phi(t)$. In (5.59), it can be observed that the PSD of oscillator $S_{\phi}(w)$ coincides with the phase noise PSD, $S_w(w)$, when small-angle approximation is applicable [93]. As a result, desired phase noise PSD $S_w(w)$ can be obtained by appropriately filtering a white gaussian noise $n(t)$ using filter with impulse response $h(t)$ as shown in Fig.5.25. Note that, in Fig.5.25, the oscillator frequency is omitted during the generation of phase noise. This is due to the fact that input signal $x(t)$ is already a baseband signal which is already translated to the IF frequency. Hence, frequency translation using w_0 is not necessary and it can be assumed that $w_0 = 0$.

As we have now a method for generating a desired PSD for phase noise, we need a PSD model for typical local oscillators. Typical microwave processing devices have a PSD with two or three dominant noise processes [90, 94] which all follow power-law decay of the spectrum as function of frequency as illustrated in Fig.5.26. Here, the phase noise is generated by filtering a white gaussian noise

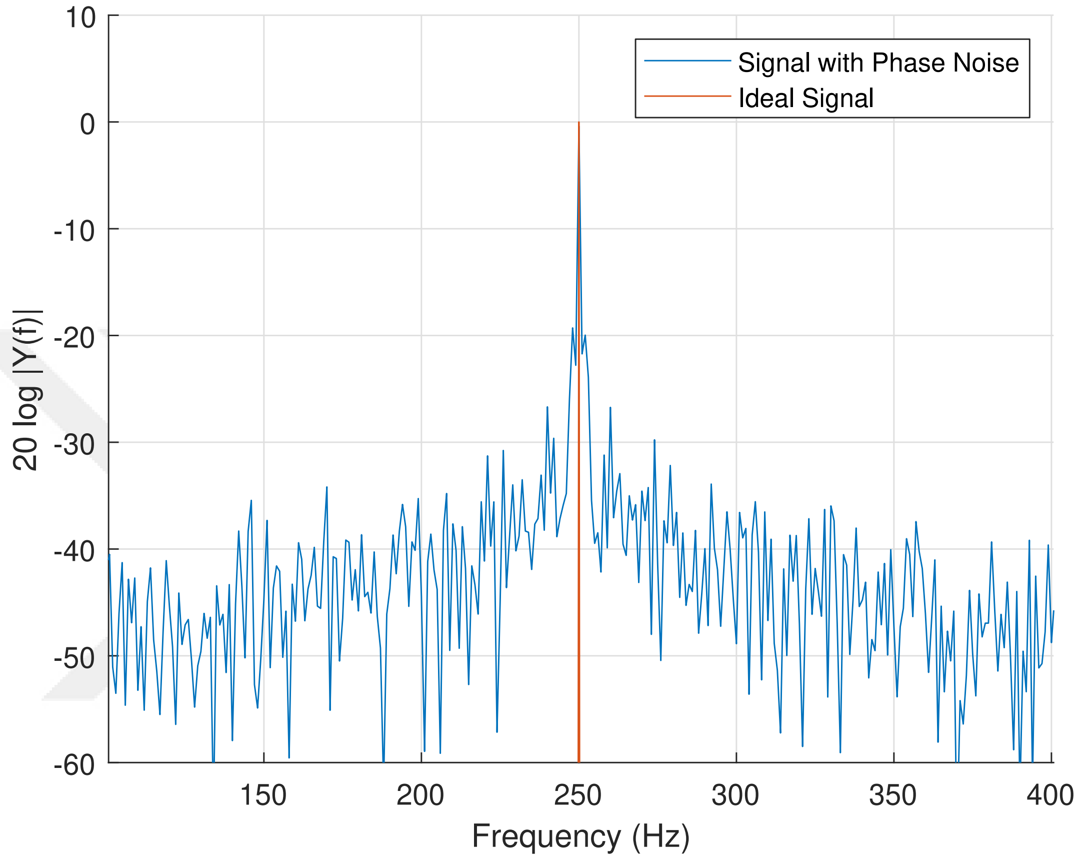

Figure 5.27: Power spectrum of the signal with input signal $x(t) = e^{j2\pi 250t}$ and phase noise with -40 dBc/Hz at 50 Hz.

process with a filter $h(t)$ which is a low-pass filter with $1/f$ decay characteristic. To do that, infite impulse response (IIR) filter design method is used which is specified in [95]. This specific filter design tool calculates the coefficients of the filter based on the desired attenuation at a specific frequency and the decay of the frequency response has $1/f$ characteristic.

To demonstrate the phase noise on a example, phase noise with -40 dBc/Hz at 50 Hz is applied to a complex exponential signal with center frequency 250 Hz and the PSD of the signal is estimated using the Discrete Fourier Transform (DFT). During the experiment, sampling frequency is taken as $f_s = 1MHz$ and number of samples that is obtained from the signal is selected in a way that DFT resolution coincides with 1 Hz. Power spectrum of a single experiment is shown in Fig.5.27. Here, it can be observed that ratio given (5.53) is around -40 dBc/Hz for the frequency offset of 50 Hz which is inline with the expected result of the experiment.

5.7.3 Simulation Results

Proposed SEI technique consist of two main stages. In terms of phase noise, the first stage, pulse alignment of radar pulses, is the weakest link of the proposed technique. In this step, baseband signal of received pulses are time aligned which is directly effected by the phase deviations that occur during the pulse. As a result, performance of the pulse alignment method under the phase noise is investigated. During the simulations, phase noise frequency offset parameter w_m is selected as 1 kHz, as it is the typical value that is specified by the commercial local oscillator manufacturers. In order to investigate the performance of time alignment, a similar approach that is used in Sec.5.3 is taken. Synthetic pulses are generated using (5.37) where modulation bandwidth given in (5.38) is selected as $B_g \in \{1, 2, 4, 8\}$. At each phase noise level between $[-100 - 40]$ dBc/Hz at 1 kHz, 1000 Monte-Carlo runs were performed. The standard deviation of the estimation error as a function of phase noise and B_g is shown in Fig.5.28. The result given in Fig.5.28 shows an expected result where accuracy of pulse alignment improves for lower phase noise levels. However, based solely on the result given in Fig.5.28, it is not possible to specify a phase noise requirement for the SEI receiver.

In order to define a specification for the SEI receiver, pulse alignment accuracy is investigated under the effect of both thermal noise and phase noise. For typical EW receivers, 20 dB SNR is a typical value that can be reached in typical EW scenarios. Hence, standard deviation of pulse alignment is obtained for phase noise levels between $[-40, -100]$ dBc/Hz at 1 kHz where SNR due to thermal noise is set to 20 dB. Results that are obtained by 1000 Monte-Carlo simulations for each phase noise level is shown in Fig.5.29. It can be observed that, almost for each modulation bandwidth, pulse alignment accuracy for phase noise levels better than -80 dBc/Hz at 1 kHz does not improve. When phase noise level is

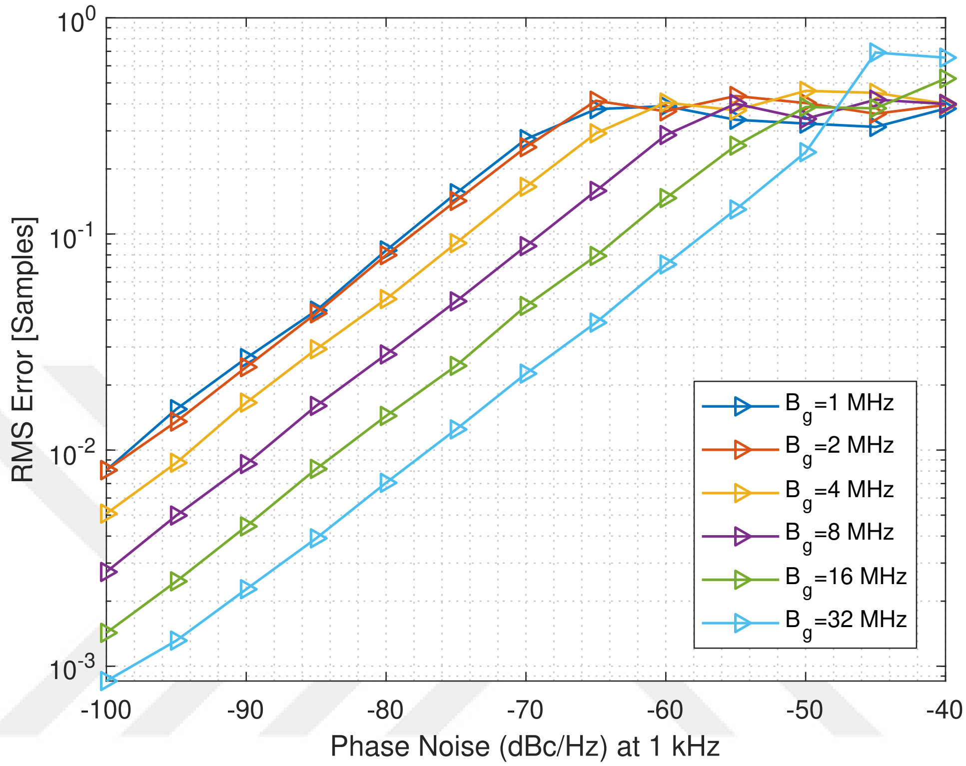

Figure 5.28: Standard deviation of the delay estimation error as a function of phase noise at 1 kHz and bandwidth B_g.

better than -80 dBc/Hz, effect of thermal noise on radar pulses becomes dominant and time alignment performance does not get better. As a result, it can be concluded that the phase noise at 1 kHz should be better than -80 dBc/Hz so that phase noise of local oscillator does not effect the performance of the proposed SEI technique.

5.8 Conclusions for Chapter 5

In this chapter, a novel SEI technique for radar transmitters is proposed. The proposed technique accurately perform time alignment and coherent integration of the collected radar pulses to boost the SNR so that UMOP on the signals can be reliably identified. Then, features related to UMOP are extracted using a VMD-based technique. The proposed technique is demonstrated successfully on real

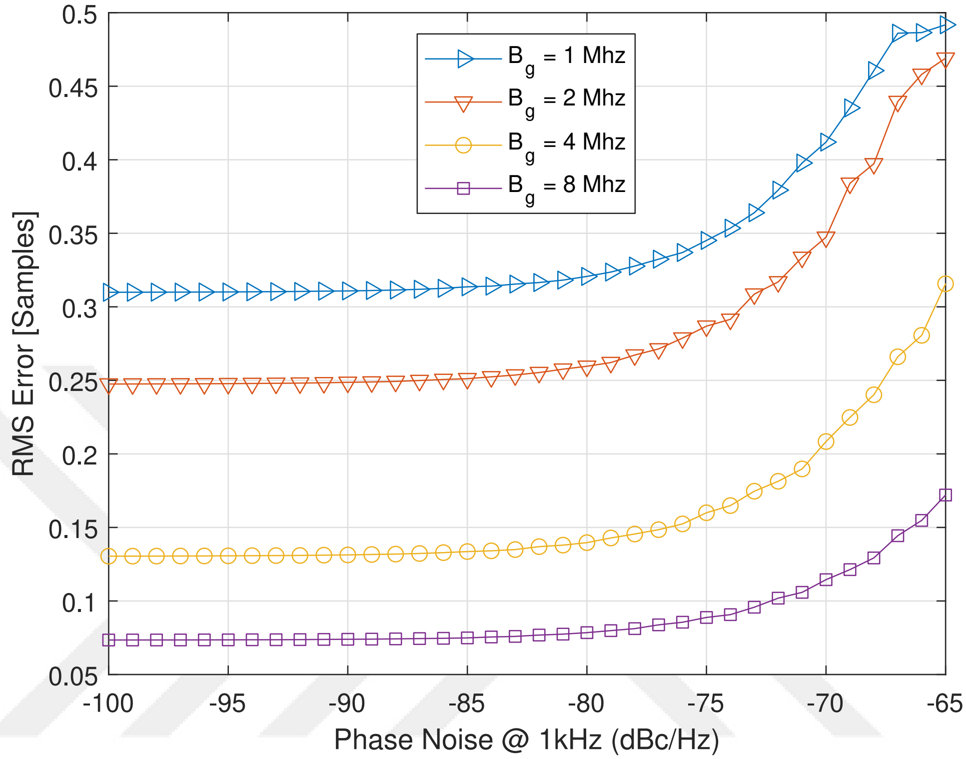

Figure 5.29: Standard deviation of the delay estimation error as a function of phase noise at 1 kHz and bandwidth B_g.

radar data sets that are significantly larger and more challenging than previously reported SEI results in the literature. Simulation results show the that proposed technique outperforms the state of the art EM^2 method. Also, few important SEI system parameters are investigated including the required SNR level for reliable classification and effect of SEI receiver phase noise on classification performance. Simulation results show that 50 dB SNR is required for reliable classification. However, in typical scenarios, 50 dB SNR is not achievable target for a single radar pulse. Considering that EW systems typically observe their targets at a SNR of around 30 dB, it can be concluded that at least 100 pulses should be integrated to obtain reliable classification performance. Another important SEI receiver design parameter is the phase noise that is mainly caused by LO. Analysis show that phase noise of the SEI receiver should be better then -80 dBc/Hz at 1 kHz.

Chapter 6

Conclusions and Future Work

In this thesis, novel signal processing techniques for two different remote sensing problems are proposed. In the first part, a new technique, ISED, which automatically obtains the underlying electron density profile in the ionosphere using the ionosonde measurements is introduced. Conducted experiments show that ISED is able to provide reliable scalings under different conditions and it outperforms the ARTIST technique which is considered as the most accomplished algorithm. ISED has two key elements behind its success. Firstly, the HMM echo extraction successfully handles spurious measurements and frequency gaps in the data. Secondly, electron density profile is reconstructed by using the IRI-Plas model which is steadily updated to model the changes in the ionosphere. As a future work, ionogram from different ionosonde stations will be investigated. Monitoring the state of the ionosphere has to be done in global scale and the ISED should be able to scale the ionograms that are measured at different ionosonde stations over the world.

In the second part of the thesis, a novel SEI technique for radar transmitters is proposed. Performance of the proposed technique is demonstrated successfully on real radar data sets which includes emitters belonging to same manufacturing line. Also, some of the most important design parameters of SEI systems are investigated. Conducted experiments show that reliable classification performance requires a level of SNR which could not be obtained using a single pulse in typical EW scenarios. However, using the results of the conducted experiments, SEI system can decide the number of pulses to be collected depending on the SNR of individual pulses in a real time manner. Another important SEI system design parameter is the phase noise of SEI receiving hardware. Simulation results show that the phase noise of the SEI receivers should be better than -80 dBc/Hz at 1 kHz.

As a future work, different SEI system design parameters such as phase linearity of band-pass filters will be investigated to provide specifications to SEI hardware. Another important research topic is the Specific Emitter Verification (SEV) [62] problem. SEV confirms the identity of a transmitter where the identity is known a priori. An important application of SEV is the verification of Identification, Friend or Foe (IFF) signals. IFF is an aircraft identification system that is designed for military and civilian air traffic control. IFF transponders located on the aircraft broadcast the identity of the aircraft. To prevent spoofing of IFF signals, SEV techniques are employed and unintentional modulations on IFF signals are used link the IFF transmitting hardware and aircrafts identity to prevent IFF spoofing. Proposed SEI feature set for radar transmitters in the scope of this thesis will be applied to the SEV problem for IFF transmitters.

Bibliography

[1] "Lowell digisonde international." https://www.digisonde.com/index.html.

[2] R. E. Collin, *Antennas and radiowave propagation.* McGraw-Hill, 1985.

[3] W. R. Piggott and K. Rawer, "URSI handbook of ionogram interpretation and reduction," 1972.

[4] N. Wakai, H. Ohyama, and T. Koizumi, "Manual of ionogram scaling," *Radio Research Laboratory, Ministry of Posts and Telecommunications, Japan*, 1987.

[5] J. D. Gilbert and R. W. Smith, "A comparison between the automatic ionogram scaling system artist and the standard manual method," *Radio Science*, vol. 23, no. 06, pp. 968–974, 1988.

[6] G. Gok, Y. K. Alp, O. Arikan, and F. Arikan, "A method for automatic scaling of ionograms and electron density reconstruction," *IEEE Transactions on Geoscience and Remote Sensing*, In review.

[7] C. Scotto, M. Pezzopane, and B. Zolesi, "Estimating the vertical electron density profile from an ionogram: On the passage from true to virtual heights via the target function method," *Radio Science*, vol. 47, no. 1, 2012.

[8] G. Gok, Y. K. Alp, and O. Arikan, "A new method for specific emitter identification with results on real radar measurements," *IEEE Transactions on Information Forensics and Security*, vol. 15, pp. 3335–3346, 2020.

[9] T. Murphy and T. Imrich, “Implementation and operational use of ground-based augmentation systems (gbass)—a component of the future air traffic management system,” *Proceedings of the IEEE*, vol. 96, no. 12, pp. 1936–1957, 2008.

[10] S. Raghunath and D. V. Ratnam, “Ionospheric gradient detection methods for ground based augmentation system,” in *2015 2nd International Conference on Electronics and Communication Systems (ICECS)*, pp. 894–898, 2015.

[11] K. Davies, *Ionospheric Radio*. No. 31, IET, 1990.

[12] K. Rawer, *Wave propagation in the ionosphere*, vol. 5. Springer Science & Business Media, 2013.

[13] K. Davies, *Ionospheric radio propagation*, vol. 80. US Department of Commerce, National Bureau of Standards, 1965.

[14] K. C. Yeh, Y. KC, and L. CH, “Theory of ionospheric waves,” 1972.

[15] J. M. Kelso and H. Hagger, “Radio ray propagation in the ionosphere,” *PhT*, vol. 18, no. 4, p. 68, 1965.

[16] J. A. Ratcliffe *et al.*, *An introduction to ionosphere and magnetosphere*. CUP Archive, 1972.

[17] “Ionosphere and magnetosphere.” Ionosphere and magnetosphere https://www.britannica.com/science/ionosphere-and-magnetosphere.

[18] K. G. Budden, *The propagation of radio waves: The theory of radio waves of low power in the ionosphere and magnetosphere*. Cambridge University Press, 1988.

[19] E. Erdem and F. Arikan, “Ray tracing on stratified plane ionosphere model,” in *2014 22nd Signal Processing and Communications Applications Conference (SIU)*, pp. 1391–1394, IEEE, 2014.

[20] G. Breit and M. A. Tuve, “A test of the existence of the conducting layer,” *Physical Review*, vol. 28, no. 3, p. 554, 1926.

[21] B. W. Reinisch, I. A. Galkin, G. Khmyrov, A. Kozlov, K. Bibl, I. Lisysyan, G. Cheney, X. Huang, D. Kitrosser, V. Paznukhov, *et al.*, "New digisonde for research and monitoring applications," *Radio Science*, vol. 44, no. 01, pp. 1–15, 2009.

[22] J. Titheridge, "Ionogram analysis with the generalised program polan," 1985.

[23] B. W. Reinisch, R. R. Gamache, J. S. Tang, and D. F. Kitrosser, "Automatic real time ionogram scaler with true height analysis-artist," tech. rep., DTIC Document, 1983.

[24] X. Huang and B. Reinisch, "Vertical electron density profiles from the digisonde network," *Advances in Space Research*, vol. 18, no. 6, pp. 121–129, 1996.

[25] C. Scotto, "Electron density profile calculation technique for autoscala ionogram analysis," *Advances in Space Research*, vol. 44, no. 6, pp. 756–766, 2009.

[26] C. Scotto and M. Pezzopane, "A software for automatic scaling of fof2 and muf (3000) f2 from ionograms," *URSI XXVIIth General Assembly*, 2002.

[27] C. Scotto and M. Pezzopane, "A method for automatic scaling of sporadic e layers from ionograms," *Radio Science*, vol. 42, no. 2, 2007.

[28] M. Fagre, J. A. Prados, J. Scandaliaris, B. S. Zossi, M. A. Cabrera, R. G. Ezquer, and A. G. Elias, "Algorithm for automatic scaling of the f-layer using image processing of ionograms," *IEEE Transactions on Geoscience and Remote Sensing*, 2020.

[29] C. Steger, "An unbiased detector of curvilinear structures," *IEEE Transactions on pattern analysis and machine intelligence*, vol. 20, no. 2, pp. 113–125, 1998.

[30] F. Arikan, S. Salous, and O. Arikan, "Algorithm for high quality ionograms," *Electronics Letters*, vol. 36, no. 11, pp. 985–987, 2000.

[31] F. Arikan, O. Arikan, and S. Salous, "A new algorithm for high-quality ionogram generation and analysis," *Radio science*, vol. 37, no. 1, pp. 1–11, 2002.

[32] L. F. McNamara, "Quality figures and error bars for autoscaled digisonde vertical incidence ionograms," *Radio science*, vol. 41, no. 04, pp. 1–16, 2006.

[33] L. Rejfek, Z. Mošna, D. Kouba, J. Boška, and D. Burešová, "Application of digital filters to check quality of the automatically scaled ionograms," *Journal of Electrical Engineering*, vol. 66, no. 3, pp. 164–168, 2015.

[34] J. Kennedy, "Particle swarm optimization," in *Encyclopedia of Machine Learning*, pp. 760–766, Springer, 2010.

[35] L. R. Rabiner, "A tutorial on hidden markov models and selected applications in speech recognition," *Proceedings of the IEEE*, vol. 77, no. 2, pp. 257–286, 1989.

[36] L. Rabiner and B. Juang, "An introduction to hidden markov models," *ieee assp magazine*, vol. 3, no. 1, pp. 4–16, 1986.

[37] D. P. Bertsekas, *Nonlinear programming.* Athena scientific Belmont, 1999.

[38] D. Calvetti, G. Golub, W. Gragg, and L. Reichel, "Computation of gauss-kronrod quadrature rules," *Mathematics of computation*, vol. 69, no. 231, pp. 1035–1052, 2000.

[39] L. F. Shampine, "Vectorized adaptive quadrature in matlab," *Journal of Computational and Applied Mathematics*, vol. 211, no. 2, pp. 131–140, 2008.

[40] X. Huang and B. W. Reinisch, "Vertical electron content from ionograms in real time," *Radio Science*, vol. 36, no. 2, pp. 335–342, 2001.

[41] K. Rawer, S. Ramakrishnan, and D. Bilitza, "International reference ionosphere, international union of radio science, ursi special report," 1978.

[42] D. Bilitza, "International reference ionosphere, nssdc 90-22," *World Data Center A, Rockets and Satellites, Greenbelt, USA*, 1990.

[43] D. Bilitza and B. W. Reinisch, "International reference ionosphere 2007: improvements and new parameters," *Advances in space research*, vol. 42, no. 4, pp. 599–609, 2008.

[44] D. Bilitza, D. Altadill, Y. Zhang, C. Mertens, V. Truhlik, P. Richards, L.-A. McKinnell, and B. Reinisch, "The international reference ionosphere 2012–a model of international collaboration," *Journal of Space Weather and Space Climate*, vol. 4, p. A07, 2014.

[45] U. Sezen, T. Gulyaeva, and F. Arikan, "Online computation of international reference ionosphere extended to plasmasphere (iri-plas) model for space weather," *Geodesy and Geodynamics*, vol. 9, no. 5, pp. 347–357, 2018.

[46] T. L. Gulyaeva, X. Huang, and B. W. Reinisch, "Plasmaspheric extension of topside electron density profiles," *Advances in Space Research*, vol. 29, no. 6, pp. 825–831, 2002.

[47] T. Gulyaeva and D. Bilitza, "Towards iso standard earth ionosphere and plasmasphere model," in *New developments in the standard model*, pp. 1–40, 2012.

[48] U. Sezen, T. L. Gulyaeva, and F. Arikan, "Performance of solar proxy options of iri-plas model for equinox seasons," *Journal of Geophysical Research: Space Physics*, vol. 123, no. 2, pp. 1441–1456, 2018.

[49] B.-H. Juang, S. E. Levinson, L. R. Rabiner, and M. M. Sondhi, "Hidden markov model speech recognition arrangement," Nov. 8 1988. US Patent 4,783,804.

[50] Y. K. Alp, U. Yavuz, and A. Bayri, "Hmm based track-before-detect strategy for fmcw/cw emitter detection," in *Signal Processing and Communications Applications Conference (SIU), 2013 21st*, pp. 1–4, IEEE, 2013.

[51] P. B. C. Leite, R. Q. Feitosa, A. R. Formaggio, G. A. O. P. da Costa, K. Pakzad, and I. D. Sanches, "Hidden markov models for crop recognition in remote sensing image sequences," *Pattern Recognition Letters*, vol. 32, no. 1, pp. 19–26, 2011.

[52] F. Li, X. Jia, D. Fraser, and A. Lambert, "Super resolution for remote sensing images based on a universal hidden markov tree model," *IEEE Transactions on Geoscience and Remote Sensing*, vol. 48, no. 3, pp. 1270–1278, 2009.

[53] N. Viovy and G. Saint, "Hidden markov models applied to vegetation dynamics analysis using satellite remote sensing," *IEEE Transactions on Geoscience and Remote Sensing*, vol. 32, no. 4, pp. 906–917, 1994.

[54] A. Viterbi, "Error bounds for convolutional codes and an asymptotically optimum decoding algorithm," *IEEE transactions on Information Theory*, vol. 13, no. 2, pp. 260–269, 1967.

[55] G. D. Forney, "The Viterbi algorithm," *Proceedings of the IEEE*, vol. 61, no. 3, pp. 268–278, 1973.

[56] J. Matzka, O. Bronkalla, K. Tornow, K. Elger, and C. Stolle, "Geomagnetic kp index," 2021.

[57] J. Bartels, "The standardized index, ks, and the planetary index, kp," *IATME Bull*, vol. 97, no. 12b, p. 0001, 1949.

[58] D. E. Gordon, "Chapter i - introduction," in *Electronic Warfare* (D. E. Gordon, ed.), pp. 1–13, Pergamon, 1981.

[59] S. Robertson, *Practical ESM Analysis*. Artech House, 2019.

[60] R. G. Wiley, *ELINT: The interception and analysis of radar signals*. Artech House, 2006.

[61] N. A. W. Center, "Electronic warfare and radar systems engineering handbook," *Electronic Warfare Division, Pont Mugu, CA*, 1997.

[62] K. I. Talbot, P. R. Duley, and M. H. Hyatt, "Specific emitter identification and verification," *Technology Review*, vol. 113, 2003.

[63] R. Crochiere and L. Rabiner, "Optimum fir digital filter implementations for decimation, interpolation, and narrow-band filtering," *IEEE Transactions*

on Acoustics, Speech, and Signal Processing, vol. 23, no. 5, pp. 444–456, 1975.

[64] T.-w. Chen, W.-d. Jin, and J. Li, “Feature extraction using surrounding-line integral bispectrum for radar emitter signal,” in *Neural Networks, 2008. IJCNN 2008.(IEEE World Congress on Computational Intelligence). IEEE International Joint Conference on*, pp. 294–298, IEEE, 2008.

[65] B. Pei, Z. Bao, and M. Xing, “Logarithm bispectrum-based approach to radar range profile for automatic target recognition,” *Pattern recognition*, vol. 35, no. 11, pp. 2643–2651, 2002.

[66] M.-W. Liu and J. F. Doherty, “Specific emitter identification using nonlinear device estimation,” in *Sarnoff Symposium, 2008 IEEE*, pp. 1–5, IEEE, 2008.

[67] A. Aubry, A. Bazzoni, V. Carotenuto, A. De Maio, and P. Failla, “Cumulants-based radar specific emitter identification,” in *Information Forensics and Security (WIFS), 2011 IEEE International Workshop on*, pp. 1–6, IEEE, 2011.

[68] S. D’Agostino, G. Foglia, and D. Pistoia, “Specific emitter identification: analysis on real radar signal data,” in *2009 European Radar Conference (EuRAD)*, pp. 242–245, IEEE, 2009.

[69] N. E. Huang, Z. Shen, S. R. Long, M. C. Wu, H. H. Shih, Q. Zheng, N.-C. Yen, C. C. Tung, and H. H. Liu, “The empirical mode decomposition and the hilbert spectrum for nonlinear and non-stationary time series analysis,” in *Proceedings of the Royal Society of London A: mathematical, physical and engineering sciences*, vol. 454, pp. 903–995, The Royal Society, 1998.

[70] C. Song, J. Xu, and Y. Zhan, “A method for specific emitter identification based on empirical mode decomposition,” in *2010 IEEE International Conference on Wireless Communications, Networking and Information Security*, pp. 54–57, IEEE, 2010.

[71] A. C. Polak and D. L. Goeckel, "Wireless device identification based on rf oscillator imperfections," *IEEE Transactions on Information Forensics and Security*, vol. 10, no. 12, pp. 2492–2501, 2015.

[72] J. Zhang, F. Wang, O. A. Dobre, and Z. Zhong, "Specific emitter identification via hilbert–huang transform in single-hop and relaying scenarios," *IEEE Transactions on Information Forensics and Security*, vol. 11, no. 6, pp. 1192–1205, 2016.

[73] G. Huang, Y. Yuan, X. Wang, and Z. Huang, "Specific emitter identification based on nonlinear dynamical characteristics," *Canadian Journal of Electrical and Computer Engineering*, vol. 39, no. 1, pp. 34–41, 2016.

[74] J. Zhang, F. Wang, Z. Zhong, and O. Dobre, "Novel hilbert spectrum-based specific emitter identification for single-hop and relaying scenarios," in *2015 IEEE Global Communications Conference (GLOBECOM)*, pp. 1–6, IEEE, 2015.

[75] U. Satija, N. Trivedi, G. Biswal, and B. Ramkumar, "Specific emitter identification based on variational mode decomposition and spectral features in single hop and relaying scenarios," *IEEE Transactions on Information Forensics and Security*, vol. 14, no. 3, pp. 581–591, 2018.

[76] B. He, F. Wang, Y. Liu, and S. Wang, "Specific emitter identification via multiple distorted receivers," in *2019 IEEE International Conference on Communications Workshops (ICC Workshops)*, pp. 1–6, IEEE, 2019.

[77] Y. Pan, S. Yang, H. Peng, T. Li, and W. Wang, "Specific emitter identification based on deep residual networks," *IEEE Access*, vol. 7, pp. 54425–54434, 2019.

[78] L. Ding, S. Wang, F. Wang, and W. Zhang, "Specific emitter identification via convolutional neural networks," *IEEE Communications Letters*, vol. 22, no. 12, pp. 2591–2594, 2018.

[79] R. H. Bartels, J. C. Beatty, and B. A. Barsky, "Hermite and cubic spline interpolation," *An Introduction to Splines for Use in Computer Graphics and Geometric Modelling*, pp. 9–17, 1998.

[80] K. Dragomiretskiy and D. Zosso, "Variational mode decomposition," *IEEE transactions on signal processing*, vol. 62, no. 3, pp. 531–544, 2014.

[81] V. Valimaki and A. Haghparast, "Fractional delay filter design based on truncated lagrange interpolation," *IEEE Signal Processing Letters*, vol. 14, no. 11, pp. 816–819, 2007.

[82] L. H. Thomas, "Elliptic problems in linear difference equations over a network," *Watson Sci. Comput. Lab. Rept., Columbia University, New York*, vol. 1, 1949.

[83] C. Knapp and G. Carter, "The generalized correlation method for estimation of time delay," *IEEE transactions on acoustics, speech, and signal processing*, vol. 24, no. 4, pp. 320–327, 1976.

[84] S. Stein, "Algorithms for ambiguity function processing," *IEEE Transactions on Acoustics, Speech, and Signal Processing*, vol. 29, no. 3, pp. 588–599, 1981.

[85] B. Boashash, *Time-frequency signal analysis and processing: a comprehensive reference*. Academic Press, 2015.

[86] M. R. Hestenes, "Multiplier and gradient methods," *Journal of optimization theory and applications*, vol. 4, no. 5, pp. 303–320, 1969.

[87] R. T. Rockafellar, "A dual approach to solving nonlinear programming problems by unconstrained optimization," *Mathematical programming*, vol. 5, no. 1, pp. 354–373, 1973.

[88] D. P. Bertsekas, *Constrained optimization and Lagrange multiplier methods*. Academic press, 2014.

[89] L. Lam and S. Suen, "Application of majority voting to pattern recognition: an analysis of its behavior and performance," *IEEE Transactions on Systems, Man, and Cybernetics-Part A: Systems and Humans*, vol. 27, no. 5, pp. 553–568, 1997.

[90] T. H. Lee and A. Hajimiri, "Oscillator phase noise: A tutorial," *IEEE journal of solid-state circuits*, vol. 35, no. 3, pp. 326–336, 2000.

[91] S. M. Rytov, Y. A. Kravtsov, and V. I. Tatarskii, *Principles of statistical radiophysics 2. Correlation theory of random processes.* 1988.

[92] G. V. Klimovitch, "A nonlinear theory of near-carrier phase noise in free-running oscillators," in *Proceedings of the 2000 Third IEEE International Caracas Conference on Devices, Circuits and Systems (Cat. No. 00TH8474)*, pp. T80–1, IEEE, 2000.

[93] A. Chorti and M. Brookes, "A spectral model for rf oscillators with power-law phase noise," *IEEE Transactions on Circuits and Systems I: Regular Papers*, vol. 53, no. 9, pp. 1989–1999, 2006.

[94] A. Hajimiri and T. H. Lee, "A general theory of phase noise in electrical oscillators," *IEEE journal of solid-state circuits*, vol. 33, no. 2, pp. 179–194, 1998.

[95] N. J. Kasdin, "Discrete simulation of colored noise and stochastic processes and 1/f/sup/spl alpha//power law noise generation," *Proceedings of the IEEE*, vol. 83, no. 5, pp. 802–827, 1995.

[96] G. H. Golub and J. H. Welsch, "Calculation of gauss quadrature rules," *Mathematics of computation*, vol. 23, no. 106, pp. 221–230, 1969.

[97] J. Gilles, "Empirical wavelet transform," *IEEE transactions on signal processing*, vol. 61, no. 16, pp. 3999–4010, 2013.

[98] I. Daubechies, J. Lu, and H.-T. Wu, "Synchrosqueezed wavelet transforms: An empirical mode decomposition-like tool," *Applied and computational harmonic analysis*, vol. 30, no. 2, pp. 243–261, 2011.

[99] A. N. Tihonov, "Solution of incorrectly formulated problems and the regularization method," *Soviet Math.*, vol. 4, pp. 1035–1038, 1963.

[100] V. A. Morozov, "Linear and nonlinear ill-posed problems," *Itogi Nauki i Tekhniki. Seriya" Matematicheskii Analiz"*, vol. 11, pp. 129–178, 1973.

[101] D. Gabor, "Theory of communication. part 1: The analysis of information," *Journal of the Institution of Electrical Engineers-Part III: Radio and Communication Engineering*, vol. 93, no. 26, pp. 429–441, 1946.

Appendix A

Adaptive Gauss-Kronrod Quadrature Rules for Integration

A.1 Brief Overview for Adaptive Gauss-Kronrod Quadrature

Most numerical integration techniques involves approximating the integrand by a polynomial in a region or regions and then integrating the polynomial exactly. Usually, complicated integrand can be factored into a non-negative weight function and another function which can be approximated by a polynomial. An n-point Gauss quadrature rule for the integral,

$$\mathcal{L}(f) = \int_a^b g(t)dt = \int_a^b w(t)f(t)dt \tag{A.1}$$

is given by

$$\mathcal{G}_n(f) := \sum_{k=1}^{N} w_k f(t_k). \tag{A.2}$$

The pair of weights w_k and nodes t_k are the quadrature rule $\{w_k, t_k\}_{k=1}^{n}$ and they are exact for integrand functions that are $2N-1$ polynomials [96].

There are efficient algorithms such as [96] that obtains the rule for N point quadrature. Note that, quadrature rule $\{w_k, t_k\}_{k=1}^{n}$ is only needed to be calculated once or may even be used from a lookup table.

The Gauss-Kronrod quadrature rule is an extension of Gauss quadrature such that:

$$\mathcal{K}_{2n+1}(f) := \sum_{k=1}^{2n+1} f(\tilde{x}_k)\tilde{w}_k \tag{A.3}$$

where nodes of the Gauss quadrature are also included in the Gauss-Kronrod quadrature rule, i.e,

$$\{x_k\}_{k=1}^{n} \subset \{\tilde{x}_k\}_{k=1}^{2n+1}. \tag{A.4}$$

There are two main advantages of Gauss-Kronrod quadrature compared to Gauss quadrature. First, Gauss-Kronrod quadrature is exact for integration of polynomial with order less then $3N + 1$. Secondly, common approach to estimate the approximation error $|\mathcal{L}(f) - \mathcal{K}_{2n+1}(f)|$ is to consider a second rule with less number of nodes. In order to estimate the approximation error for Gauss-Kronrod quadrature, Gauss quadrature rule that uses the subset of Gauss-Kronrod quadrature can be used, i.e,

$$|\mathcal{L}(f) - \mathcal{K}_{2n+1}(f)| \approxeq |\mathcal{G}_n(f) - \mathcal{K}_{2n+1}(f)|. \tag{A.5}$$

As nodes of the Gauss quadrature are included in Gauss-Kronrod quadrature, integrand function is not needed to be evaluated again for error approximation. As a result, approximation error can be calculated efficiently which leads to efficient adaptive implementation. To improve the accuracy of the result, integral interval can be split into smaller regions and integral of sub intervals and related error approximations can be calculated. Then, for sub intervals with low accuracy can be split into more sub intervals until a given error tolerance is satisfied. The algorithm for adaptive Gauss-Kronrod is given in Algorithm 5.

In this study, Gauss-Kronrod with a set of 15 nodes is used. Weights and nodes that are used are given in Table A.1.

Algorithm 5 Adaptive Gauss-Kronrod Quadrature $(a, b, f(x))$

N: Minimum number of sub-intervals

Initialization: Split $[a, b]$ interval into N sub-intervals such that:

$$q_n = [a_n, b_n],\ n = 1 \dots N.$$

$I \leftarrow 1 \dots N$, I:Set of sub-interval indices with insufficient accuracy.

while $I \neq \{\emptyset\}$ **do**

  $\mathcal{K}_{15}(n) = \sum_{k=1}^{15} f(\tilde{x}_k)\tilde{w}_k, \forall n \in I$

  $\mathcal{G}_7(n) = \sum_{k=1}^{7} f(\tilde{x}_k)\tilde{w}_k, \forall n \in I$

  $E(n) = |\mathcal{K}_{15}(n) - \mathcal{G}_7(n)|$

  $I \leftarrow \{n | E(n) > tol\}$, I:Update the sub-interval indices with insufficient accuracy.

  $\mathcal{L}(f) = \sum_{n \notin I} \mathcal{K}_{15}(n)$, Update the total sum with results of sub-intervals that satisfy the accuracy requirement.

end while

Table A.1: Gauss-Kronrod (7,15) Weights and Nodes

Weights	**Nodes**
0.0229	-0.9915
0.0631	-0.9491
0.1048	-0.8649
0.1407	-0.7415
0.1690	-0.5861
0.1904	-0.4058
0.2044	-0.2078
0.2095	0
0.2044	0.2078
0.1904	0.4058
0.1690	0.5861
0.1407	0.7415
0.1048	0.8649
0.0631	0.9491
0.0229	0.9915

Appendix B

User Manual of Ionolab-IED

B.1 Quick Guide

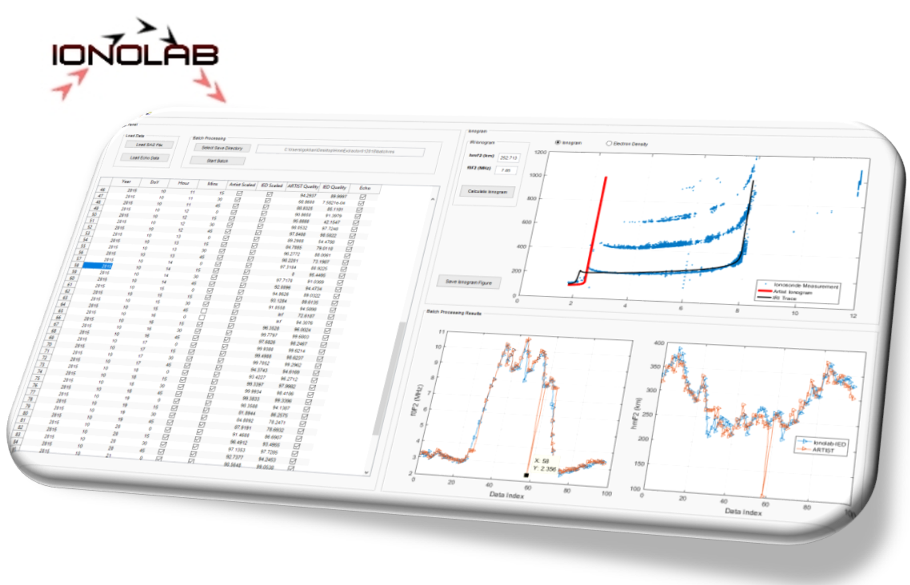

Figure B.1: IONOLAB-IED software for ionogram scaling.

IONOLAB-IED is a software for ionogram scaling which incorporates ISED algorithm. IONOLAB-IED is developed in Matlab environment. In Fig.B.2, main components of the IONOLAB-IED graphical user interface are numbered and each component is summarized below.

1. **Load Data Panel**: Through this panel, user can load SAO files and Echo Data.

2. **Batch Processing Panel**: User can execute batch processing for all loaded data through this panel.

3. **Data Table**: Information for loaded data is shown in this table. User can select a specific data by clicking the corresponding row in the table to start automatic scaling process.

4. **Scaling Result Plot**: Results obtained using ARTIST (if available) and IONOLAB-IED is shown in this plot along with the ionosonde vertical O-Ray measurements. Also, user can see the electron density distribution in this plot.

5. **Result Selection Button Group**: User can choose between ionogram and electron density to be shown on Scaling Result Plot.

6. **IRI Ionogram Panel**: After automatic scaling process, user can see optimal IRI parameters in this panel. Also, user can obtain ionograms for different parameters of IRI by entering the related parameters into text boxes and by pressing 'Calculate Ionogram' button.

7. **Save Ionogram Button**: Ionogram that is shown on Scaling Result Plot is saved using this button. When 'Save Ionogram Button' is pressed, a dialog box appears to let user select the file path for saving ionogram.

8. **Batch Processing Result-1** : f_oF2 parameters that are obtained by both ARTIST and IONOLAB-IED is shown for all processed files.

9. **Batch Processing Result-2**: h_mF2 parameters that are obtained by both ARTIST and IONOLAB-IED is shown for all processed files.

10. **Status Bar**: This text box shows the status of the software.

11. **Graphical Tools**: Toolbar provides the basic tools for all plots in the software.

Details of each component is given in the following sections of the document.

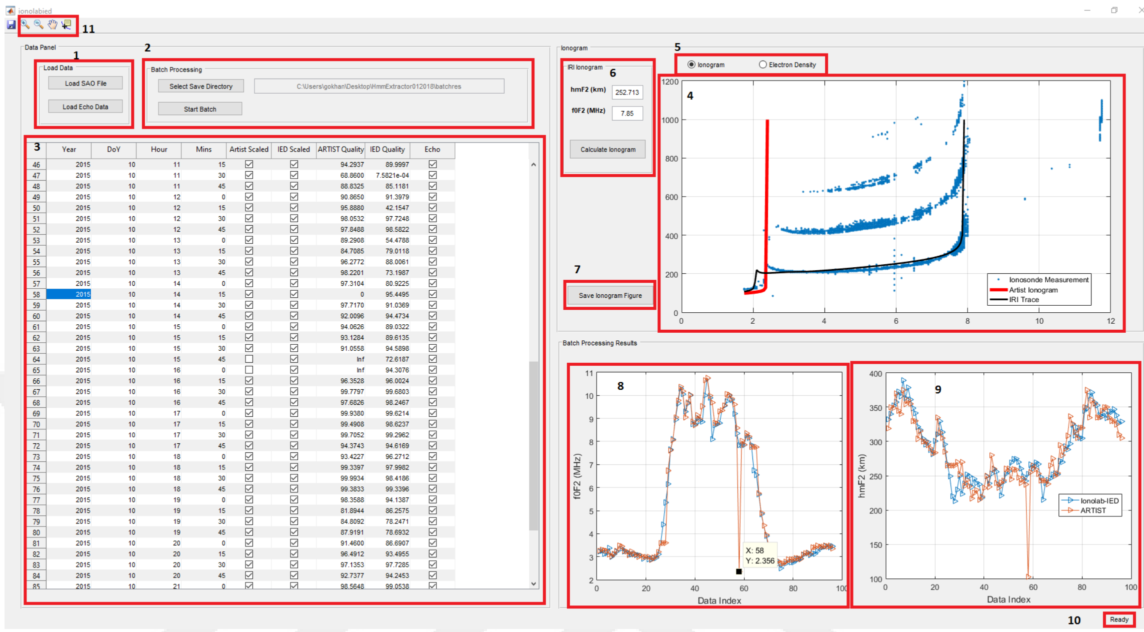

Figure B.2: User interface of IONOLAB-IED.

B.2 Importing Ionosonde Data

Importing data into the software can be done using the 'Load Data Panel' that is shown with number (1) in Fig.B.2. Importing process can be completed using two simple steps:

- **Loading SAO Files**: In order to load SAO files into the software, user should click to ''Load SAO File" button. Then a dialog box shown in Fig.B.3 will appear and user can choose which SAO files to load. In this dialog box, multiple files can be chosen to load. After loading process is completed, loaded data will appear in Data Table.
- **Load Echo Data**: After loading SAO data, echo data that is extracted from SAO explorer can be loaded using the 'Load Echo Data' button. SAO explorer can export ionosonde measurements in '.txt' format using the '. rsf' file that contains raw ionosonde measurements. In Fig.B.4, extracting echo data from SAO Explorer is shown. SAO Explorer will create a '.txt' file for selected data after this step which can be directly loaded into software.

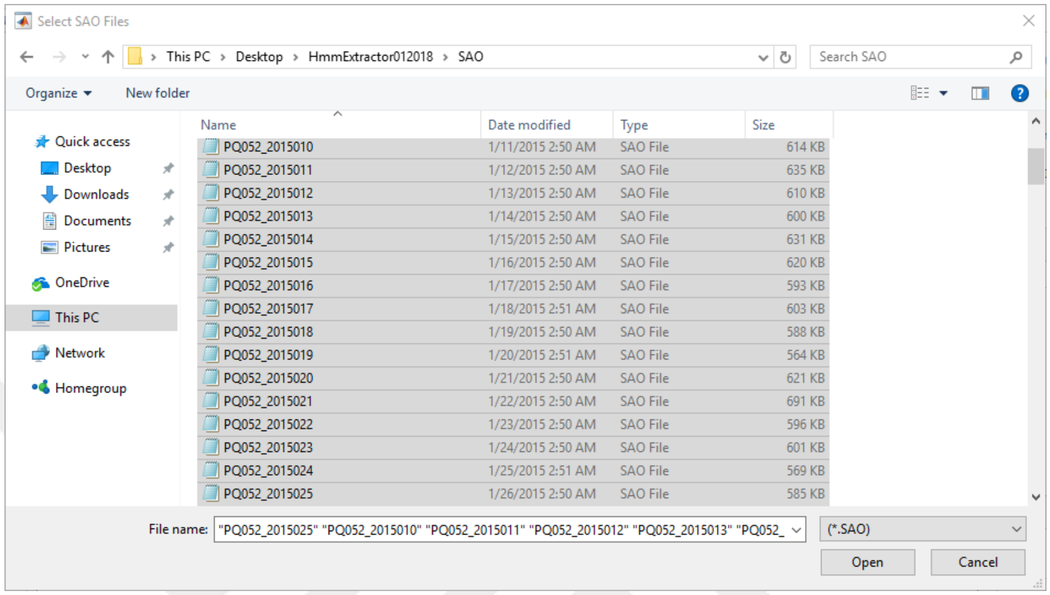

Figure B.3: Loading .SAO files to IONOLAB-IED.

B.3 Data Table

After loading data into the software, user can view the loaded data in the Data Table. Every row in data table shows a different ionosonde measurement. Detailed information of the columns are given in Table.B.1.

Table B.1: Descriptions for data table columns.

Year	Measurement year
DoY	Measurement day of year
Hour	Measurement hour
Mins	Measurement minute
IONOLAB-IED	Ticked when ISED scaling available
Artist Quality	Quality factor for ARTIST
IED Quality	Quality factor for IONOLAB-IED
Echo	Ticked when echo data is available
Artist Scaled	Ticked when ARTIST scaling available.

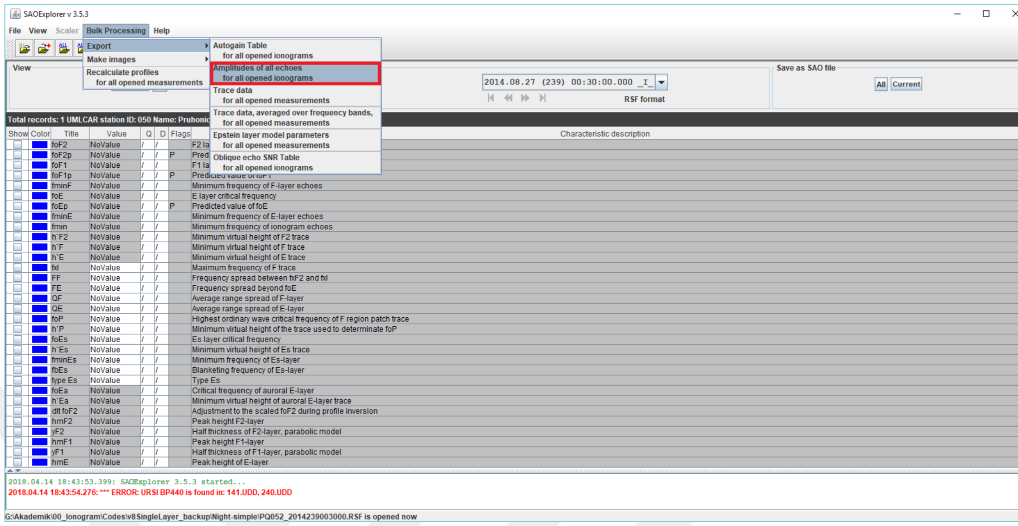

Figure B.4: Exporting raw ionogram data from SAO Explorer.

	Year	DoY	Hour	Mins	Artist Scaled	IED Scaled	ARTIST Quality	IED Quality	Echo
1	2015	10	0	0	☑	☑	98.7300	79.3522	☑
2	2015	10	0	15	☑	☑	99.8673	85.7425	☑
3	2015	10	0	30	☑	☑	99.2039	93.0227	☑
4	2015	10	0	45	☑	☑	99.9123	81.8123	☑

Figure B.5: IONOLAB-IED data table.

B.4 Batch Processing Panel

User can initiate a batch process in order to scale all loaded ionosonde data and calculate the quality factors. To do that, user must set a folder for saving batch processing results. Software automatically saves ionograms for all processed data to this folder in '.png' and '.fig' file formats. A single in example for saved data is shown in Fig.B.6.

After batch processing is completed, F2 layer parameters are plotted in 'Batch Processing Result Panel'. In this plots, x-axis shows the data index that can be matched with data index in the 'Data Table' as shown in Fig.B.7.

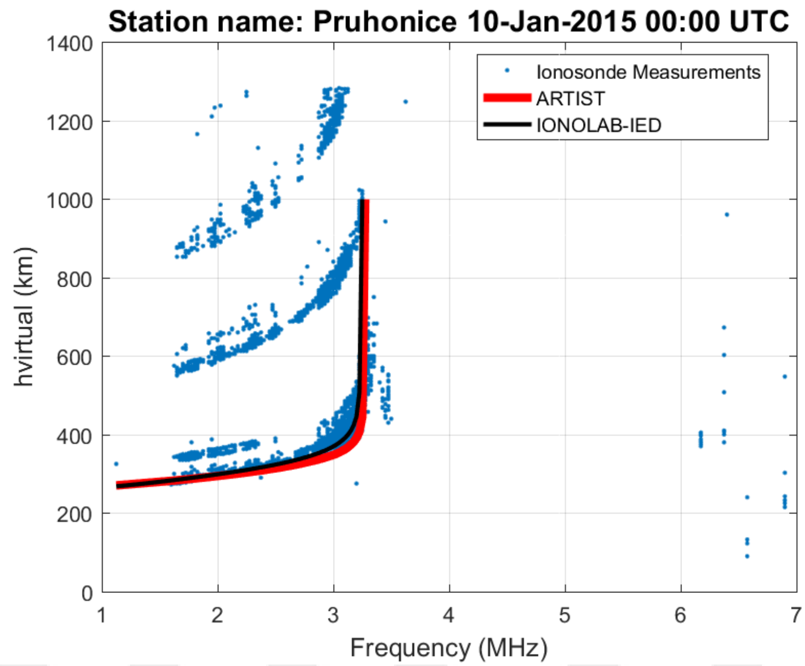

Figure B.6: Example picture file for saving IONOLAB-IED results.

B.5 Scaling Result Panel

In this panel, scaling result for selected data in ‘Data Table’ is shown. Also user can do the following operations in this panel:

- Resulting graph can be switched between Ionogram and electron density distribution using the button group above the graph.
- User can obtain ionograms for different IRI parameters by entering the parameters and press ‘Calculate Ionogram’ button as shown in Fig.B.7.
- Ionograms can be saved as an image file using the ‘Save Ionogram’ button. When pressed, this button will open a dialog box for user to select a path and extension for image file.

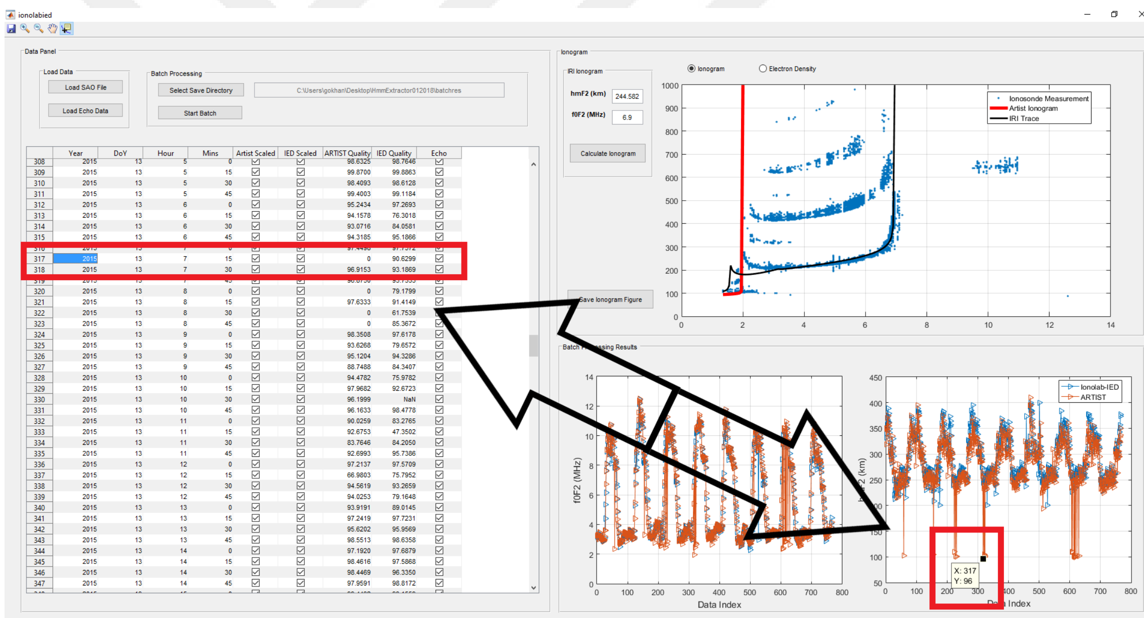

Figure B.7: Batch processing results of IONOLAB-IED.

Appendix C

Detailed Derivations for Variational Mode Decomposition

In this section, detailed derivations that are given in [80] for VMD are provided.

C.1 Definitions and Signal Processing Tools

C.1.1 Intrinsic Mode Functions

Variational mode decomposition (VMD), decomposes a given signal into so-called *Intrinsic Mode Functions* (IMF) where IMFs are defined based on a modulation criteria. Intrinsic Mode Functions are signals which have amplitude and frequency modulations, written as:

$$\mu_k(t) = A_k(t)\cos(\phi_k(t)), \tag{C.1}$$

where the phase $\phi_k(t)$ is a non-decreasing function, $\phi^{'}(t) \geq 0$, the envelope is non-negative $A_k(t) > 0$, and the instantaneous frequency $w_k(t) := \phi_k^{'}(t)$ and the envelope $A_k(t)$ vary much slower than the phase $\phi_k(t)$ [97], [98]. With these definitions, $u_k(t)$ can be considered as pure harmonic.

C.1.2 Wiener Filtering

Wiener filtering is a solution to obtain original signal f from the noisy version of the signal f_o

$$f_o = f + n \tag{C.2}$$

where n is the zero-mean Gaussian noise. Recovering the unknown signal can be obtained by solving the Tikhonov regularized cost function [99], [100]:

$$\min_{f} ||f - f_o||_2^2 + \alpha ||\partial_t f||_2^2 \tag{C.3}$$

Optimization problem given in (C.3) can be solved by writing Euler-Lagrange equations and solved in Fourier domain as :

$$\hat{f}(w) = \frac{\hat{f}_o}{1 + \alpha w^2} \tag{C.4}$$

where $f(w)$ is the Fourier transform of the signal.

C.1.3 Hilbert Transform

Hilbert transform is the linear, shift invariant operator denoted by $\mathcal{H}$. It is a all-pass filter that converts the sign of negative frequencies and characterized by the transfer function

$$\hat{h}(w) = -jsgn(w) = -\frac{jw}{|w|}, \tag{C.5}$$

where $j^2 = -1$. The most typical use of Hilbert transform is to obtain an analytical signal proposed in [101] which is discussed in the next section.

C.1.4 Analytical Signal

Let $f(t)$ be a real signal. The complex analytical signal is defined as:

$$f_A(t) = f(t) + j\mathcal{H}f(t) \tag{C.6}$$

An important property of the analytical signal given in (C.6) is that it only consist of non-negative frequencies in Fourier domain. Also note that, original signal $f(t)$ can be obtained from the analytical signal as:

$$f(t) = \mathcal{R}\left\{f_A(t)\right\}. \tag{C.7}$$

C.1.5 Frequency Mixing

Mixing is the process of combining two signals in a non-linear fashion. During the derivation of VMD, mixing of two analytical signals is used. When analytical signal $f_A(t)$ is mixed with pure exponential, the output of mixing process is given by:

$$f_A(t)e^{-jw_0 t} \overset{\mathcal{F}}{\longleftrightarrow} \hat{f}_A(w) * \delta(w + w_0) = \hat{f}_A(w + w_0) \tag{C.8}$$

where δ is the Dirac distribution and $*$ denotes the convolution operator. Thus, multiplying an analytical signal with a pure exponential results in frequency shifting in Fourier domain.

C.1.6 Variational Mode Decomposition

The aim of VMD is to decompose a real valued signal f into a discrete number of modes u_k that is sparse in spectral domain. In other words, each mode u_k is compact around a center frequency w_k which is determined along with the decomposition. To achieve this goal, bandwidth of each mode is assessed by using the $\mathcal{L}^2$ norm of the gradient of each mode signal. VMD proposes the scheme that is illustrated in Fig.C.1. The steps of VMD can be summarized as:

1. For each u_k, compute the analytic signal using Hilbert transform and obtain a spectrum that consist of non-negative frequencies.

2. For each mode, shift the signal to baseband by mixing it with the pure exponential with frequency w_k.

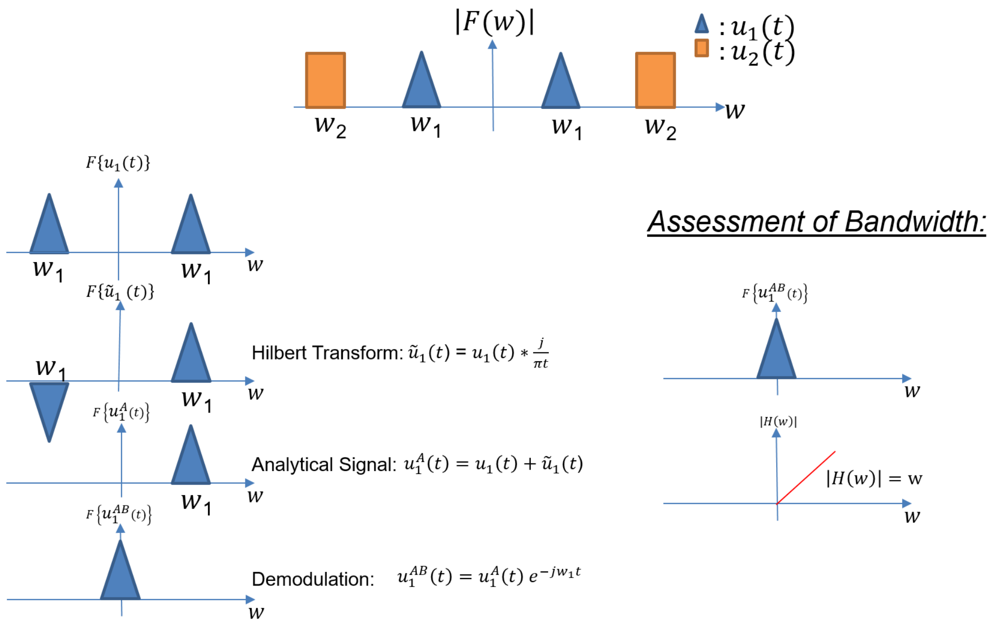

Figure C.1: Illustration of VMD processing.

3. Asses the bandwidth of each mode using $\mathcal{L}^2$ norm of the gradient of each mode signal.

To implement these steps, VMD solves the following optimization problem:

$$\min_{\{u_k\},\{w_k\}} \left\{ \sum_k \left\| \partial_t \left[\delta(t) + \frac{j}{\pi t} * u_k(t) \right] e^{-jw_k t} \right\|_2^2 \right\} \qquad \text{(C.9)}$$
$$s.t \quad \sum_k u_k = f$$

The reconstruction constraint of the optimization problem given in (C.9) is handled by making use of both Lagrangian multipliers and quadratic penalty term and augmented Lagrangian $\mathcal{L}$ can be formed as:

$$\mathcal{L}(\{u_k\}, \{w_k\}, \lambda) := a \sum_k \left\| \partial_t \left[\left(\delta(t) + \frac{j}{\pi t} \right) * u_k(t) \right] e^{-jw_k t} \right\|_2^2 \qquad \text{(C.10)}$$
$$\left\| f(t) - \sum_k u_k(t) \right\|_2^2 + \left\langle \lambda(t), f(t) - \sum_k u_k(t) \right\rangle.$$

The solution of the optimization problem in (C.9) can be found as the saddle

Algorithm 6 ADMM Optimization for VMD

1: *Initialization:* $\{\hat{u}_k^1\}, \{\hat{w}_k^1\}, \hat{\lambda}^1, n \leftarrow 0$
2: **repeat**
3: $n \leftarrow n+1$
4: **for** $k = 1 : K$ **do**
5: Update u_k:

$$\hat{u}_k^{n+1} \leftarrow \arg\min_{u_k} \mathcal{L}\left(\{u_{i<k}^{n+1}\}, \{u_{i\geq k}^{n}\}, \{w_i^n\}, \lambda^n\right) \tag{C.11}$$

6: Update w_k:

$$\hat{w}_k^{n+1} \leftarrow \arg\min_{w_k} \mathcal{L}\left(\{u_i^{n+1}\}, \{w_{i<k}^{n+1}\}, \{w_{i\geq k}^{n}\}, \lambda^n\right) \tag{C.12}$$

7: **end for**
8: Dual Ascent:

$$\lambda^{n+1} \leftarrow \lambda^n + \tau\left(f - \sum_k u_k^{n+1}\right) \tag{C.13}$$

9: **until** convergence $\sum_k \|\hat{u}_k^{n+1} - \hat{u}_k^n\|_2^2 / \|\hat{u}_k^n\|_2^2 < \epsilon$

point of the augmented Lagrangian $\mathcal{L}$ that is given in (C.10) using the iterative optimization method known as alternate direction method of multipliers (ADMM) [86–88] given in Alg.6. In (C.13), τ is the parameter that enables the Lagrangian multiplier to enforce the constraint which can be disabled by setting $\tau = 0$ when exact reconstruction is not the goal. During the iterations, two sub optimization problems given in (C.11) and (C.12) is solved which is detailed in the next two subsections.

C.1.6.1 Update Step of u_k

To update the modes, u_k, the optimization problem given in (C.11) is rewritten as:

$$u_k^{n+1} = \arg\min_{u_k} \; \alpha \left\| \partial_t \left[\left(\delta(t) + \frac{j}{\pi t} \right) * u_k(t) \right] e^{-jw_k t} \right\|_2^2 + \left\| f(t) - \sum_i u_i(t) + \frac{\lambda(t)}{2} \right\|_2^2 \tag{C.14}$$

Using the Parseval/Plancherel Fourier isometry under the L^2 norm, this problem can be written in spectral domain as:

$$\hat{u}_k^{n+1} = \underset{\hat{u_k}}{\arg\min} \;\; \alpha \left\| jw \left[(1 + \operatorname{sgn}(w + w_k))\, \hat{u}_k(w + w_k) \right] \right\|_2^2 + \left\| \hat{f}(w) - \sum_i \hat{u}_i(w) + \frac{\hat{\lambda}(w)}{2} \right\|_2^2 \tag{C.15}$$

After performing change of variables $w \leftarrow (w - w_k)$ in the first term, result becomes

$$\hat{u}_k^{n+1} = \underset{\hat{u_k}}{\arg\min} \;\; \alpha \left\| j(w - w_k) \left[(1 + \operatorname{sgn}(w))\, \hat{u}_k(w) \right] \right\|_2^2 + \left\| \hat{f}(w) - \sum_i \hat{u}_i(w) + \frac{\hat{\lambda}(w)}{2} \right\|_2^2 \tag{C.16}$$

Exploiting the Hermitian symmetry of real signals in the reconstruction fidelity terms, we can write both terms as half space integrals over the non-negative frequencies as:

$$\hat{u}_k^{n+1} = \underset{\hat{u_k}}{\arg\min} \;\; \left\{ \int_0^\infty 4\alpha(w - w_k)^2 |\hat{u}_k(w)|^2 + 2 \left| \hat{f}(w) - \sum_i \hat{u}_i(w) + \frac{\hat{\lambda}(w)}{2} \right|^2 dw \right\} \tag{C.17}$$

The solution of this quadratic optimization problem can be found by letting the first variation vanish for positive frequencies:

$$\hat{u}_k^{n+1} = \frac{\hat{f}(w) - \sum_{i \neq k} \hat{u}_i(w) + \frac{\hat{\lambda}(w)}{2}}{1 + 2\alpha(w - w_k)^2} \tag{C.18}$$

which is the Wiener filtering of the current residual, with signal frequency around w_k. The full spectrum of the mode $\hat{u}_k$ can be obtained by Hermitian symmetric completion and the mode in time domain can be obtained as the real part of the inverse Fourier transform of this filtered analytic signal.

C.1.6.2 Update Step of w_k

The center frequencies, w_k, only appear in the first term of the augmented Lagrangian given in (C.10). Hence, the optimization problem for w_k can be stated

Algorithm 7 ADMM Optimization for VMD [1]

Initialization: $\{\hat{u}_k^1\}, \{\hat{w}_k^1\}, \hat{\lambda}^1, n \leftarrow 0$
repeat
  $n \leftarrow n + 1$
  for $k = 1 : K$ **do**
    Update mod signals:

$$\hat{u}_k^{n+1}(w) \leftarrow \frac{\hat{x}(w) - \sum_{i<k} \hat{u}_i^{n+1}(w) - \sum_{i>k} \hat{u}_i^{n}(w) + \frac{\hat{\lambda}}{2}}{1 + 2a(w - w_k)^2} \tag{C.22}$$

    Update mod frequencies:

$$w_k^{n+1} \leftarrow \frac{\int_0^\infty w|\hat{u}_k^{n+1}(w)|^2 dw}{\int_0^\infty |\hat{u}_k^{n+1}(w)|^2 dw} \tag{C.23}$$

  end for
  Dual Ascent for all $w \geq 0$:

$$\hat{\lambda}^{n+1}(w) \leftarrow \hat{\lambda}^{n}(w) + \tau \left(\hat{f}(w) - \sum_k \hat{u}_k^{n+1}(w) \right) \tag{C.24}$$

until convergence $\sum_k \|\hat{u}_k^{n+1} - \hat{u}_k^{n}\|_2^2 / \|\hat{u}_k^{n}\|_2^2 < \epsilon$

as:

$$w_k^{n+1} = \underset{w_k}{\arg\min} \left\{ \left\| \partial_t \left[\left(\delta(t) + \frac{j}{\pi t} \right) * u_k(t) \right] e^{-jw_k t} \right\|_2^2 \right\} \tag{C.19}$$

As for the update step of mode signals, u_k, the optimization can be done in Fourier domain. Optimal center frequencies in each iteration can be found solving the following problem:

$$w_k^{n+1} = \underset{w_k}{\arg\min} \left\{ \int_0^\infty (w - w_k)^2 |\hat{u}_k(w)|^2 dw \right\}, \tag{C.20}$$

which is a quadratic problem and its solution is given by:

$$w_k^{n+1} = \frac{\int_0^\infty w|\hat{u}_k(w)|^2 dw}{\int_0^\infty |\hat{u}_k(w)^2| dw}. \tag{C.21}$$

The complete procedure of VMD optimization is given in Algorithm 7.

[1] All the variables with no iteration superscript denotes the latest variables that is obtained during the ADMM iterations.